Kumulative Dissertation

Models in nonlinear condensed-matter optics: From theory to experiment

zur Erlangung des Grades
eines Doktors der Naturwissenschaften

von
Kay-Michael Voit

genehmigt vom Fachbereich Physik der

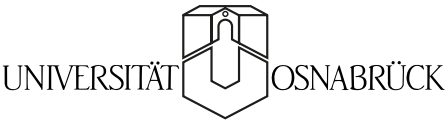

Osnabrück, im März 2013

Hauptberichterstatter:	Prof. Dr. Mirco Imlau
Berichterstatter:	apl. Prof. Dr. Heinz-Jürgen Schmidt

Tag der Einreichung:	27.02.2013
Tag der mündlichen Prüfung:	28.03.2013

"The igibûm exceeded the igûm by 7.
What are the igûm and the igibûm?"

– YBC 6967, 1. Babylonian Dynasty [1]

Contents

1. Introduction **7**

2. Holographic gratings **11**
2.1. Publications 13
2.2. Unpublished results 14
2.2.1. Derivation of real number coupled-wave equations (RN-CWT) . 14
2.2.2. Analysis of RN-CWT 15

3. Space-charge wave spectroscopy **21**
3.1. Publications 23

4. Photofunctional molecules **25**
4.1. Publication 26

5. Summary & Conclusion **27**

A. Open access publications **29**
A.1. Small-polaron based holograms in LiNbO3 in the visible spectrum . . . 31
A.2. Holographic Spectroscopy 47

B. Publications with proprietary licenses **75**

C. Contributions to conferences **123**

Bibliography **125**

Acknowledgement **131**

Eidesstattliche Erklärung **131**

1. Introduction

As indicated by the title, the central subjects of this thesis are theoretical – i. e. mathematical – models and their application to the experimental process. A mathematical model may be defined as *"an abstract, simplified, mathematical construct related to a part of reality and created for a particular purpose"* [2, 3]. Depending on the nature, complexity and purpose of the problem, one might choose different types of models on various levels, for example: descriptive or predictive, continuous or discrete, analytical or numerical, microscopic or macroscopic, stochastic or deterministic, qualitative or quantitative ones [4].

Some of the simplifications in the process of modeling are strongly linked to the abstraction: Aspects of reality that have no effects on the system under consideration are neglected. However, on close inspection, there is seldom anything that has exactly no effect on the system. This is illustrated by an extreme but prominent example from popular science, the Butterfly Effect [5]. Thus, an early and essential task is the distinction between those effects that may be *neglected* and those that are crucial: Ignoring too many aspects of reality will make the model useless, as it lacks precision. Ignoring too few, however, might increase the complexity beyond manageability, regarding solvability, required data or necessary computational power. Depending on the purpose, trade-offs may be made in generality, realism or precision. Simulation models, for example, tend to sacrifice generality in favor of realism and precision [2, 6].

Besides the negligible aspects of reality, a second class is formed by entities that effect the modeled system, but are not part of it themselves. In mathematical models, they often provide the boundary conditions, or, more generally spoken, exogenous variables. Examples are the thermodynamic heat bath, or, in some models presented later, the incident laser beam (before it interacts with the system under consideration). The third class, of course, is the system under consideration, constituted by its endogenous variables.

In a second step of simplification, the mathematical relation between exogenous variables and endogenous variables may be considered. For example, in some systems that change on a large time constant, derivatives of higher order may be neglected, greatly simplifying differential equations. Perhaps the most common method at this stage is the simplification of complicated dependences between endogenous and exogenous variables, for example via expansion into Taylor or Fourier series. Reduction to first or even zero order is customary in these cases.

Today, mathematical modelling forms the basis of many modern sciences, including physics. However, one might say that modelling predates science by ten thousands of years: In 1937 in Vestonice in Moravia, a wolfbone was found, featuring 55 notches, from which 25 where pooled in groups of five [7, 8]. It was dated to be at least 20,000

years old, and it is assumed to have served a hunter in counting prey or even slain wolves in particular. The wolfbone served as a description of reality, abstracting and simplifying it by reducing reality to the only necessary aspect. Striping the wolves down to a notch as a countable entity and omitting all other attributes – especially the hard-to-carry clawy and teethy ones – was not only a considerable increase of comfort, but may be described as one of the first evidences for human economic – and in a wider sense mathematical – modelling.

The next important step was made in the early ancient civilisations, more than 15,000 years later. Centralized bureaucratic nations with outspread trading contacts required the invention of calculation [9], which naturally widely extended the possibilities for mathematical modelling. For example, both Egyptian and Babylonic scribes reduced their buildings and granaries to numerical diameter and height to determine their capacities [9–11]. The Egyptian Papyri Rhind, Kahûn, Moscow, and Berlin feature various exercise tasks like

> "Example for the production of a magazine of 9 (and of) 10." [11]

followed by instructions to calculate the volume. The Babylonian clay board YBC 5037 is inscribed with the question

> "An excavation. Every side of the upper square is 1/2 gar. Every side of the lower square is 4 cubit. The depth is 1/2 gar. What is the volume?" [11, 12].

Especially Babylon produced a considerable amount of boards with word problems to torment their apprentice scribes. Due to the durable clay form, many Babylonian boards are preserved until today, while most Egyptian papyri are lost [11, 13]. They feature various geometrical and economical problems and discuss mathematical techniques including roots, exponentials, calculation of interest and 2^{nd} order algebraic equations [11].

In the following 3,000 years, mathematics were extensively used in astronomy and astrology. Still, the description of reality via mathematical models cannot be qualified as science in the modern sense, as – besides calendrical purposes – religion was still strongly connected to the measuring of celestial bodies [14, 15]. Nevertheless – but not until the 16^{th} century – the conjunction of mathematical models and science was performed in this very field, initiated by the Copernican Revolution [16, 17]. Soon after, Newton and Leibniz developed infinitesimal calculus and classical mechanics. Parallel to this process, Bacon, Descartes, and Kant revolutionized epistemology, providing the basis for the fundamental rules of science [17]. Since that time, the combination of sophisticated mathematical models and scientific methods in empirical observation characterises all natural sciences. Especially modern physics is born from this fusion.

Until today, experimental advances in all fields of physics demand the construction of new and the amelioration of existing models. The publications compiled in this cumulative thesis cover subtopics of nonlinear solid state optics. The models presented are derived in close collaboration with the experimental branch of our research group. This strong coupling of theory and experiment allows agile adaption of models to new

experimental circumstances and direct proof or disproof of theoretical approaches. Three important topics in modern photonics are studied. While a comprehensive introduction and motivation is included in the respective chapters, a short overview is given in the following:

In chapter 2, the coupled-wave theory first introduced by Kogelnik [18] is reviewed and extended with emphasis on out-of-phase mixed holographic gratings. This class of gratings becomes increasingly important due to novel methods of hologram recording and new classes of materials and metamaterials like holographic polymer dispersed liquid crystals. Additionally, advances in laser technology suggest a stronger spectroscopic view on holography. The model presented in this thesis accounts for both of these demands and provides a closed analytical solution.

Chapter 3 contributes to the field of space-charge waves (SCW), which provides powerful tools for material analysis, especially in semiconductor technology. Although the underlying theory is generally understood [19], recent improvements of the experimental techniques required extensions of the model and the interpretation of new effects. In this thesis, the existing formalism is adapted to a new method of excitation, which not only simplifies the experimental setup, allowing for easier adoption into industrial environments, but also provides insight into the direction of carrier motion. Furthermore, the model is extended to describe the influence of an external magnetic field, adding the possibility to examine the Hall mobility of carriers.

Eventually, chapter 4 studies the dynamics of light induced absorption in photochromic $[Ru(bpy)_2(OSO)]^+$. Compared to other photofunctional compounds, this molecule is nontoxic and exhibits exceptional photochromic reactions. These properties make it a promising candidate for important industrial and technological applications, ranging from data storage to non-electronic computation. For a profound analysis, the models used for the description of photofunctional molecules [20–22] have been completely revised to account for the pronounced absortion changes in the material. Furthermore, a setup with orthogonal pump and probe beams is modeled and experimentally tested. This novel geometry is introduced to resemble common industrial setups.

In all fields, the theoretical models are presented in conjunction with the adjoined experimental work, both explaining and predicting the experimental data. The results show remarkable agreement between theory and experiment.

2. Holographic gratings

The term "holography", which is derived from *ολος*, *complete*, and *γραφειν*, *to write*, has been coined by Dennis Gábor in 1947, who developed it as a "new principle" for microscopy [23]. As an imaging technique, it can be compared to photography – however, instead of the intensity and frequency of the light, it captures intensity and phase. Through the phase, the hologram carries directional information, allowing 3D images from a limited field of vision. Via multiplexing of multiple holograms, the field of vision can be extended and color added, covering the CIE range [24].

Hologram recording strongly depends on a coherent light source. Not surprisingly, like many other optical applications, its success story [25–28] is strongly correlated with the realisation of the laser in 1960 [29].

Summing it up, holograms may be used to control intensity, phase/direction, and frequency of light. These qualities make them important components in optical setups, ranging from filters over mirrors to microscopic image carriers [30–36]. In state-of-the-art technological applications, holograms are of great interest especially for storage and display purposes [37, 38].

The formation of holograms is widely understood [39, 40]. The classical method is to interfere a plain reference wave with a signal wave, carrying the image information, inside a photosensitive material (see figure 2.1). The recording in the material consists of an absorption or refractive index modulation – i. e. a complex permittivity modulation. It is read via the plain reference beam, leading to a reconstruction of the signal beam carrying the image.

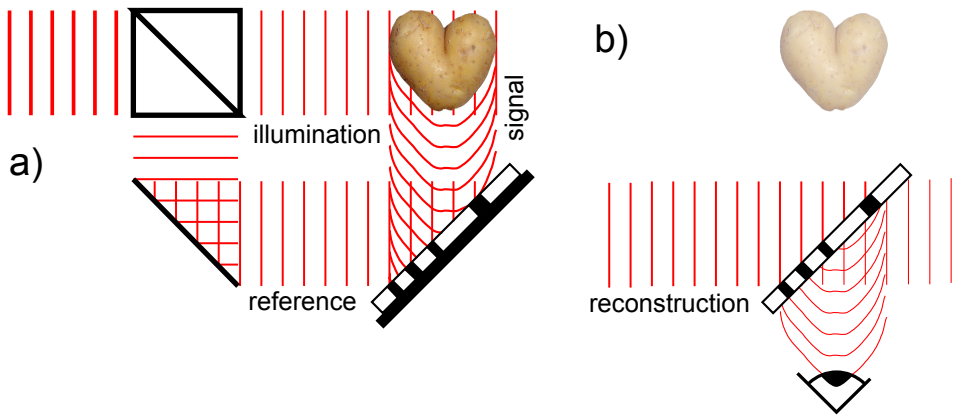

Figure 2.1.: Recording (a) and reconstruction (b) of a thick transmission hologram. *Image of potato from Wikicommons user Lumbar, public domain license.*

The simplest hologram is obviously the image of another plain wave (besides the one of no wave). It consists of the sinusoidal permittivity grating and results in a – generally partial – diffraction of the plane reconstruction wave from the direction of the reference wave – i. e. the Bragg angle of the grating – into the direction of the initial signal wave. The ratio between the intensity of the incident beam I_0 and diffracted beam I_S is described by the diffraction efficiency $\eta = I_S/I_0$. Despite the fact that a first theoretical description has been given by Kogelnik in 1969 [18] and the structure of far more complex holograms can be calculated for decades [41–46], the sinusoidal modulation is still of great theoretical interest, especially regarding the diffraction efficiency and the phase development in thick volume holograms.

Kogelnik's theory covers gratings with pure or in-phase absorption and refractive index gratings and low modulation depths. It has been used for the past 40 years – for example in material sciences for the characterisation of light-matter interaction. Nowadays, however, a review and extension of the theory has become necessary due to new materials featuring strong, photosensitive effects allowing for high modulation depths and complex out-of-phase gratings. Additionally, advances in laser technology allowing to create a wide range of frequencies have made a spectroscopic view on holography interesting.

Publication 1 presents a reviewed version of Kogelnik's coupled-wave theory for thick holographic gratings, updating and extending it to complex out-of-phase gratings and discussing new, emerging effects. Publication 2 applies these theories for studying small-polaron based holograms in thermally reduced, nominally undoped lithium niobate regarding diffraction efficiency, relaxation behavior and dependence on pump-beam intensity. In the unpublished-results section, calculations and discussions regarding the phase behavior during beam diffraction or coupling inside a thick hologram are shown.

Further fundamentals on the topic are given in the publications.

2.1. Publications

In the field of holographic gratings, the author contributed to the following articles in scientific, peer-reviewed journals:

1. Voit, K.-M. and M. Imlau. *"Holographic Spectroscopy: Wavelength-Dependent Analysis of Photosensitive Materials by Means of Holographic Techniques."*
MDPI Materials 6, no. 1 (January 23, 2013): 334–358. doi:10.3390/ma6010334.

   Abstract: Holographic spectroscopy is highlighted as a powerful tool for the analysis of photosensitive materials with pronounced alterations of the complex permittivity over a broad range in the visible spectrum, due to the advances made both in the fields of advanced holographic media and highly tunable lasers systems. To analytically discuss consequences for in- and off-Bragg reconstruction, we revised Kogelnik's coupled-wave theory strictly on the basis of complex permittivities. We extended it to comply with modern experimental parameters such as out-of-phase mixed holograms and highly modulated gratings. A spatially modulated, wavelength-dependent permittivity that superimposes a spatially homogeneous wavelength-dependent ground state spectrum is taken into account for signal wave reconstruction with bulky elementary mixed gratings as an example. The dispersion characteristics of the respective diffraction efficiency is modelled for color-center-absorption and absorption of strongly localized carriers. As an example for the theoretical possibilities of our newly derived set of equations, we present a quantitative analysis of the Borrmann effect connected to out-of-phase gratings, providing easier and more intuitive methods for the derivation of their grating parameters.

2. Brüning, H., V. Dieckmann, B. Schoke, K.-M. Voit, M. Imlau, G. Corradi, and C. Merschjann. *"Small-polaron Based Holograms in $LiNbO_3$ in the Visible Spectrum."*
Opt. Express 20, no. 12 (June 4, 2012): 13326–13336. doi:10.1364/OE.20.013326.

   Abstract: Diffraction efficiency, relaxation behavior and dependence on pump-beam intensity of small-polaron based holograms are studied in thermally reduced, nominally undoped lithium niobate in the visible spectrum ($\lambda = 488\,\mathrm{nm}$). The pronounced phase gratings with diffraction efficiency up to $\eta = (10.8 \pm 1.0)\%$ appeared upon irradiation by single ns-laser pulses ($\lambda = 532\,\mathrm{nm}$) and are comprehensively assigned to the optical formation of spatially modulated densities of small bound $NbLi^{4+}$ electron polarons, $NbLi^{4+}$:$NbNb^{4+}$ electron bipolarons, and O-hole polarons. A remarkable quadratic dependence on the pump-beam intensity is discovered for the recording configuration $K \parallel c$-axis and can be explained by the electro-optic contribution of the optically generated small bound polarons. We discuss the build-up of local space-charge fields via small-polaron based bulk photovoltaic currents.

Both articles were published open access and are included in appendix A.

2.2. Unpublished results

2.2.1. Derivation of real number coupled-wave equations (RN-CWT)

The complex-amplitude version of the coupled-wave equations

$$\frac{\mathrm{d}\bar{R}(z)}{\mathrm{d}z} = \frac{e^{i\Phi_A} k_0 \epsilon_1''(\lambda) \bar{S}(z)}{4\left(\epsilon_0'(\lambda)\right)^{1/2}\cos(\theta)} - \frac{i e^{i\Phi_B} k_0 \epsilon_1'(\lambda) \bar{S}(z)}{4\left(\epsilon_0'(\lambda)\right)^{1/2}\cos(\theta)} \tag{2.1}$$

$$\begin{aligned}\frac{\mathrm{d}\bar{S}(z)}{\mathrm{d}z} = &\frac{e^{-i\Phi_A} k_0 \epsilon_1''(\lambda) \bar{R}(z)}{4\left(\epsilon_0'(\lambda)\right)^{1/2}\cos(\theta)} - \frac{i e^{-i\Phi_B} k_0 \epsilon_1'(\lambda) \bar{R}(z)}{4\left(\epsilon_0'(\lambda)\right)^{1/2}\cos(\theta)} \\ &+ i\left(\frac{K_x^2}{2k_0\left(\epsilon_0'(\lambda)\right)^{1/2}\cos(\theta)} - K_x\tan(\theta)\right)\bar{S}(z),\end{aligned} \tag{2.2}$$

derived in *"Holographic Spectroscopy: Wavelength-Dependent Analysis of Photosensitive Materials by Means of Holographic Techniques."* (publication 1, included in appendix A, see for details on derivation and quantities), is well-suited for an analytical solution. However, it obscures some important information about two-wave coupling, namely the mechanics of the beam's phase development inside the crystal. In the following, we substitute the complex amplitudes of the electric field E with its Euler representation $\bar{R}(z) = \bar{r}(z)\exp(i\Phi_r(z))$ (and the analogue version for $\bar{S}$) to examine the phase explicitly.

Separation into real and imaginary part of the equation results in four coupled ordinary differential equations (ODE) for $\bar{r}(z)$, $\bar{s}(z)$, $\Phi_r(z)$ and $\Phi_s(z)$. The first two equations only depend on $\Phi_{\text{Diff}} \equiv \Phi_s(z) - \Phi_r(z)$. The second two equations may be subtracted from each other, resulting in an equation also only depending on $\Phi_{\text{Diff}}(z)$. Consequently, the set of equations considered in the following will be

$$\begin{aligned}\bar{r}'(z) = &\frac{\cos\left(\Phi_A - \Phi_{\text{Diff}}(z)\right) k_0 \epsilon_1''(\lambda)}{4n_0\cos(\theta)}\bar{s}(z) \\ &+ \frac{\sin\left(\Phi_B - \Phi_{\text{Diff}}(z)\right) k_0 \epsilon_1'(\lambda)}{4n_0\cos(\theta)}\bar{s}(z)\end{aligned} \tag{2.3}$$

$$\begin{aligned}\bar{s}'(z) = &\frac{\cos\left(\Phi_A - \Phi_{\text{Diff}}(z)\right) k_0 \epsilon_1''(\lambda)}{4n_0\cos(\theta)}\bar{r}(z) \\ &- \frac{\sin\left(\Phi_B - \Phi_{\text{Diff}}(z)\right) k_0 \epsilon_1'(\lambda)}{4n_0\cos(\theta)}\bar{r}(z)\end{aligned} \tag{2.4}$$

$$\begin{aligned}\bar{r}(z)\bar{s}(z)\Phi_{\text{Diff}}'(z) = &\beta(\theta)\bar{r}(z)\bar{s}(z) \\ &- \frac{\sin\left(\Phi_A - \Phi_{\text{Diff}}(z)\right) k_0 \epsilon_1''(\lambda)}{4n_0\cos(\theta)}\left(\bar{r}(z)^2 + \bar{s}(z)^2\right) \\ &- \frac{\cos\left(\Phi_B - \Phi_{\text{Diff}}(z)\right) k_0 \epsilon_1'(\lambda)}{4n_0\cos(\theta)}\left(\bar{r}(z)^2 - \bar{s}(z)^2\right)\end{aligned} \tag{2.5}$$

Note that this is no longer a set of linear differential equations and we will not bother with another full analytical solution. Instead, it is important to see that the equations for

the amplitudes only indirectly contain the off-Bragg parameter $\beta(\theta)$ through $\Phi_{\text{Diff}}(\theta)$. This means that the phase relation between the two beams – i. e. is the position of the interference pattern of the illumination in relation to the holographic grating – governs the diffraction efficiency. It is subject to a "dephasing" due to the off-Bragg parameter.

We will examine the development of the phase along the propagation through the grating in the following, using numerical methods.

2.2.2. Analysis of RN-CWT

Numerical examination

Given the appropriate boundary conditions, the set of eqs. (2.3)-(2.5) can be easily solved numerically. The focus of the calculations presented here lies on the development of the phase difference between the reference and the signal beam. The reference beam intensity is normalized to an initial intensity $I_{R,0} = 1\,\text{W/m}^2$. In contrast to the diffraction analysis that publication 1 is focussed on, we will start with an additional "signal beam" with small initial intensity $I_{S,0} \ll 0.001\, I_{R,0}$, i. e. we model a real beam-coupling experiment (two incident beams) with a beam intensity ratio of $1 : 1000$. Besides omitting numerical and conceptual problems with an arbitrary or undefined initial phase $\Phi_s(0)$ of a zero-intensity beam, this allows us to observe how the phase difference – i. e. the position of the interference pattern of the two beams relative to the grating – develops during the coupling process along the z direction. The initial phase in a beam diffraction setup (one incident beam) can then be derived as the limit $I_{S,0} \to 0$.

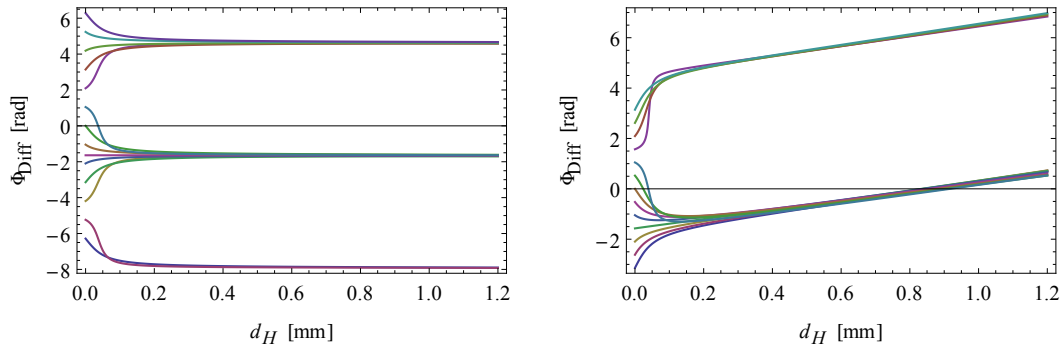

Figure 2.2.: Development of Φ_{Diff} inside the grating for $I_{S,0} = 0.0004\,\text{W/m}^2$, $\alpha_0 = 260\,\text{m}^{-1}$, $\alpha_1 = 130\,\text{m}^{-1}$, $n_0 = 2.1776$, $n_1 = -1.179 \cdot 10^{-4}$, in-Bragg (left) and off-Bragg (right).

For a first calculation, we use the parameters similar to the refractive grating published in [47]: $\alpha_0 = 260\,\text{m}^{-1}$, $\alpha_1 = 130\,\text{m}^{-1}$, $n_0 = 2.1776$, $n_1 = -1.179 \cdot 10^{-4}$. Consequently, the imaginary part of the permittivity is negligible[48]. Figure 2.2 shows the development of the phase difference $\Phi_{\text{Diff}}(z)$ inside the grating for $I_{S,0} = 0.0004\, I_{R,0}$ and different initial

values of $\Phi_{\text{Diff},0}$. It is obvious that all solutions to different boundary conditions converge to a single value (up to 2π equivalence). In the off-Bragg case, the phase differences again show asymptotic behavior to a linear function with a slope proportional to the off-Bragg parameter $\beta(z)$.

It is to be determined if this linear behavior holds true for any kind of grating. Figure 2.3 shows the development caused by a mixed grating. The refractive index grating from above has been maintained, while the absorption grating has been increased to $\alpha_0 = 2000\,\text{m}^{-1}$, $\alpha_1 = 2000\,\text{m}^{-1}$. The results in a ϵ_1' and ϵ_1'' of nearly equal size.

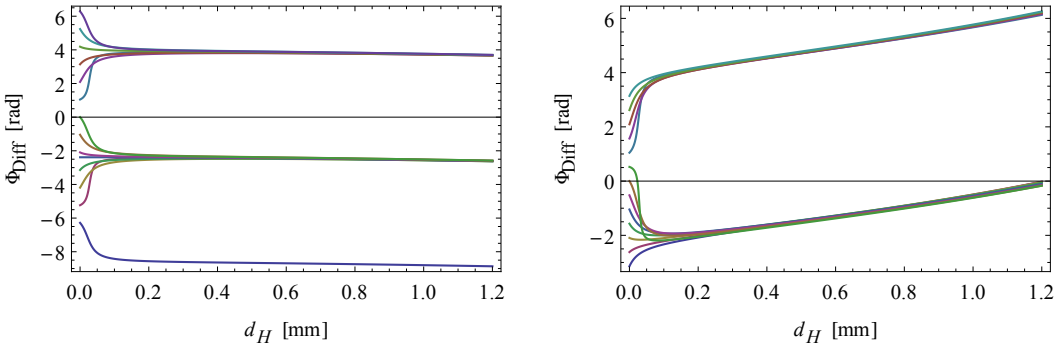

Figure 2.3.: Development of Φ_{Diff} inside the grating for $I_{S,0} = 0.0004\,\text{W/m}^2$, $\alpha_0 = 2000\,\text{m}^{-1}$, $\alpha_1 = 2000\,\text{m}^{-1}$, $n_0 = 2.1776$, $n_1 = -1.179 \cdot 10^{-4}$, in-Bragg (left) and off-Bragg (right).

It can be observed that the linear behavior is slightly disturbed. A final calculation is performed on a pure absorption grating with the same parameters as above. The results are shown in figure 2.4.

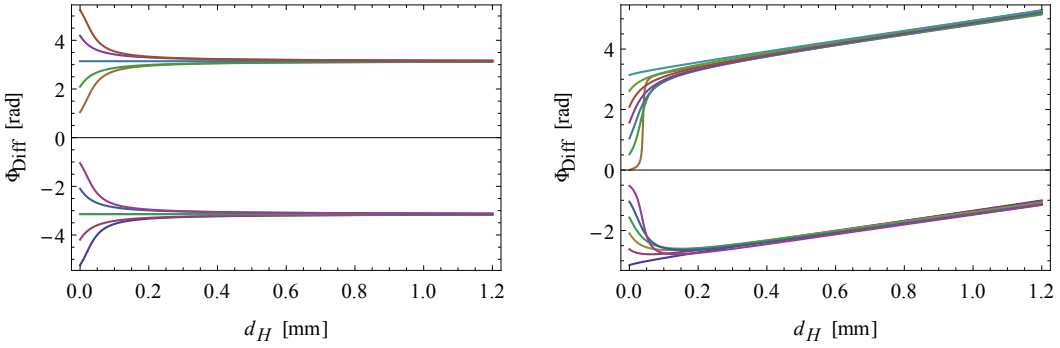

Figure 2.4.: Development of Φ_{Diff} inside the grating for $I_{S,0} = 0.0004\,\text{W/m}^2$, $\alpha_0 = 2000\,\text{m}^{-1}$, $\alpha_1 = 2000\,\text{m}^{-1}$, $n_0 = 2.1776$, $n_1 = 0$, in-Bragg (left) and off-Bragg (right).

In a real beam coupling experiment ($I_R \approx I_S$), however, for common gratings the

energy transfer between the two beams will not be high enough to shift Φ_{Diff} to an optimal value. Indeed, in not too thick volume gratings (which can, however, still be described with the established term "thick grating") in the sub-millimeter scale, the phases will not be shifted at all in first approximation, as shown in fig. (2.5). We will briefly discuss this case later on. For very thick gratings, though, simulations including the full phase equation may be necessary.

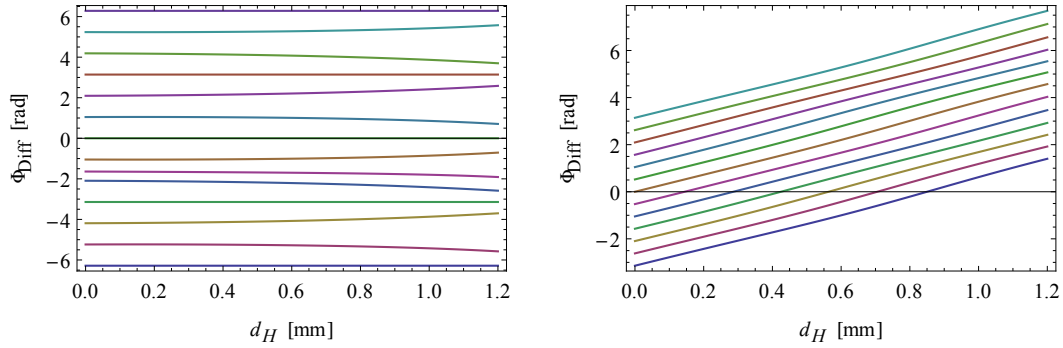

Figure 2.5.: Development of Φ_{Diff} in a beam coupling experiment, in-Bragg (left) and off-Bragg (right). Apart from $I_S = 1$, the same parameters as in fig. 2.2 have been applied.

Analytical examination

To determine $\Phi_{\text{Diff}}(0)$ for a diffraction, we evaluate eq. (2.5) at $z = 0$, inserting the boundary conditions $\bar{r}(0) = r_0$, $\bar{s}(0) = 0$. Obviously, every term containing $\bar{s}(z)$ vanishes, including the derivative. The remaining equation can be solved for $\Phi_{\text{Diff}}(0)$, giving

$$\Phi_{\text{Diff}}(0) = \arccos\left(\frac{\cos(\Phi_A)\,\epsilon_1''(\lambda) - \sin(\Phi_B)\,\epsilon_1'(\lambda)}{\sqrt{\epsilon_1''(\lambda)^2 + 2\sin(\Phi_A - \Phi_B)\,\epsilon_1''(\lambda)\epsilon_1'(\lambda) + \epsilon_1'(\lambda)^2}}\right). \tag{2.6}$$

Note that this holds true for any mixed grating. In the case of pure gratings, $\Phi_A = \Phi_B = 0$ can be assumed and the phase difference $\Phi_{\text{Diff}}(0)$ solves to $\pi/2$ for a pure absorption grating, and 0 for a pure refractive-index grating. This can be interpreted as constructive interference building up in regions of large refractive index and low absorption, as we described the grating using a cosine. Thus, there is an optimal relation between the grating and the interference pattern of the reference beam and the signal beam for coupling. In the photon picture one may think of the photons having a probability density that is highest in the low refraction index regions and in the low absorption regions. Due to the avoiding of absorption centers, this results in a higher total intensity of the outgoing beams than one would expect from the mean absorption of the grating. Note that this is in good agreement with the results published in [48, 49], where the highest diffraction efficiency of a mixed grating is achieved with a mixed $\pi/2$ phase

shift between the gratings. In that case, the interference pattern of the reference and the signal beam is in optimal position regarding both gratings. In the in-Bragg case, the system is able to maintain the optimal phase relation, while in the off-Bragg case, dephasing leads to a divergence from this optimal value.

The numerical examination of a pure refractive grating suggests $\Phi_{\text{Diff}}(z) = \Phi_{\text{Diff},0} + az$ as an ansatz. The slope a of the phase difference can likewise be obtained from the equation eq. (2.5).

Differentiating eq. (2.5) in z, evaluating in $z = 0$, and inserting the boundary conditions $\bar{r}(0) = r_0$, $\bar{s}(0) = 0$ leaves an equation containing a only in the term $ar_0 s'(0)$. Inserting the equation

$$\cos\left(\Phi_B - \Phi_{\text{Diff}}(0)\right) = -\frac{\sin\left(\Phi_A - \Phi_{\text{Diff}}(0)\right)\ \epsilon_1''(\lambda)}{\epsilon_1'(\lambda)}, \tag{2.7}$$

which we know from finding $\Phi_{\text{Diff}}(0)$ above, eliminates another two terms. Introducing eq. (2.4) simplifies the problem greatly, leaving an equation that can be solved to

$$a = -\frac{1}{2} n_0 k_0 \beta(\theta). \tag{2.8}$$

This is exactly the exponent of the first phase factor in eq. (30) of [48]. Indeed, this result could already be obtained from this equation. It can be easily shown that in case $\Phi = 0$ or π and $\epsilon_1''(\lambda) \leq \epsilon_1'(\lambda)$ this factor is the only complex quantity and thus governs the phase behaviour. Consequently, the linear phase shift holds true not only for pure refractive index gratings but for any grating fulfilling the above condition.

Using these results, the coupled-wave equations can be expressed as

$$\begin{aligned}
\bar{r}'(z) = &\frac{\cos\left(\Phi_A - \Phi_{\text{Diff},0} + \frac{\beta(\theta)}{2} z\right) k_0 \epsilon_1''(\lambda)}{4 n_0 \cos(\theta)} \bar{s}(z) \\
&+ \frac{\sin\left(\Phi_B - \Phi_{\text{Diff},0} + \frac{\beta(\theta)}{2} z\right) k_0 \epsilon_1'(\lambda)}{4 n_0 \cos(\theta)} \bar{s}(z)
\end{aligned} \tag{2.9}$$

$$\begin{aligned}
\bar{s}'(z) = &\frac{\cos\left(\Phi_A - \Phi_{\text{Diff},0} + \frac{\beta(\theta)}{2} z\right) k_0 \epsilon_1''(\lambda)}{4 n_0 \cos(\theta)} \bar{r}(z) \\
&- \frac{\sin\left(\Phi_B - \Phi_{\text{Diff},0} + \frac{\beta(\theta)}{2} z\right) k_0 \epsilon_1'(\lambda)}{4 n_0 \cos(\theta)} \bar{r}(z)
\end{aligned} \tag{2.10}$$

for any grating fulfilling $\Phi = 0$ or π and $\epsilon_1''(\lambda) \leq \epsilon_1'(\lambda)$.

On the other hand, in a beam-coupling experiment ($\bar{s}(0) \approx \bar{r}(0)$) within a "not too thick" grating, $\Phi_{\text{Diff}}(z)$ can be assumed to be approximately constant. Due to the large parameter space, general statements on the applicability of the approximation cannot be made and it should be tested via simulations on the particular parameter set in question.

Further simplifications are possible in several experimental setups. For example, substituting $\bar{r}(z) = r_0$, $\bar{s}(z) = s_0$ in eqs. (2.9),(2.10) in the in-Bragg case (i. e. assuming that the intensity changes are small through the crystal) resembles the beam-coupling equations derived in [50].

Real value analysis of the in-Bragg system

In the off-Bragg case, eqs. (2.9),(2.10) constitute a system of two first order ODEs with real, periodic coefficients. The elements of the corresponding non-constant matrix are given by

$$\hat{P}_{11} = \hat{P}_{22} = 0 \tag{2.11}$$

$$\hat{P}_{12} = \frac{\cos\left(\Phi_A - \Phi_{\text{Diff},0} + \frac{\beta(\theta)}{2}z\right) k_0 \epsilon_1''(\lambda)}{4n_0\cos(\theta)} + \frac{\sin\left(\Phi_B - \Phi_{\text{Diff},0} + \frac{\beta(\theta)}{2}z\right) k_0 \epsilon_1'(\lambda)}{4n_0\cos(\theta)} \tag{2.12}$$

$$\hat{P}_{21} = \frac{\cos\left(\Phi_A - \Phi_{\text{Diff},0} + \frac{\beta(\theta)}{2}z\right) k_0 \epsilon_1''(\lambda)}{4n_0\cos(\theta)} - \frac{\sin\left(\Phi_B - \Phi_{\text{Diff},0} + \frac{\beta(\theta)}{2}z\right) k_0 \epsilon_1'(\lambda)}{4n_0\cos(\theta)}. \tag{2.13}$$

A general strategy for the solution of such an equation does not exist. In the in-Bragg case, however, the coefficient matrix is constant and can be solved with basic methods, resulting in an analytically equivalent form to the one derived in [48]. The general solution of the in-Bragg problem is given by the following equation:

$$\begin{pmatrix} \bar{r} \\ \bar{s} \end{pmatrix} = C_1 \mathbf{P}_1 e^{p_1 z} + C_2 \mathbf{P}_2 e^{p_2 z}, \tag{2.14}$$

where $\mathbf{P}_{1,2}$ are the eigenvectors of $\hat{P}$ and $p_{1,2}$ are their related eigenvalues. $C_{1,2}$ emerge from the boundary conditions which – in case of a diffraction experiment – are $\bar{R}(0) = 1$, $\bar{S}(0) = 0$.

The result for a diffraction experiment ($I_s(0) = 0$) is

$$\bar{r}_{\text{IB}}(z) = \cosh\left(\frac{\sqrt{Z_A^2 - Z_B^2}k_0}{4n_0\cos(\theta_B)}z\right) r_0 \tag{2.15}$$

$$\bar{s}_{\text{IB}}(z) = -\sqrt{\frac{Z_A - Z_B}{Z_A + Z_B}}\sinh\left(\frac{\sqrt{Z_A^2 - Z_B^2}k_0}{4n_0\cos(\theta_B)}z\right) r_0, \tag{2.16}$$

where $Z_A = \epsilon_1''(\lambda)\cos\left(\Phi_A - \Phi_{\text{Diff},0}\right)$ and $Z_B = \epsilon_1'(\lambda)\sin\left(\Phi_B - \Phi_{\text{Diff},0}\right)$. Note that all amplitudes have to be multiplied by the factor $\exp(-\alpha_0 z/(2\cos(\theta))$ to reincorporate the Beer-Lambert factor. The final resulting intensities are then

$$I_{r,\text{IB}}(z) = I_0 A_{LB}(\theta)\cosh\left(\frac{\sqrt{P_A^2 - P_B^2}k_0}{4n_0\cos(\theta_B)}z\right)^2 \tag{2.17}$$

$$I_{s,\text{IB}}(z) = I_0 A_{LB}(\theta)\frac{P_A - P_B}{P_A + P_B}\sinh\left(\frac{\sqrt{P_A^2 - P_B^2}k_0}{4n_0\cos(\theta_B)}z\right)^2, \tag{2.18}$$

where $A_{LB}(\theta) = \exp(-\alpha_0 z/\cos(\theta))$ again is the absorption according to the Beer-Lambert law for the mean grating absorption.

3. Space-charge wave spectroscopy

The method of space-charge wave (SCW) spectroscopy is a powerful tool for material analysis [51, 52], originally associated with the field of photorefractive crystals and holography [53–59]. It can be used to conduct investigations not only on the defect structure of photoelectric crystals but also on the nature of charge transfer including the direction of carrier motion [60].

In recent years, it has been extended to various classes of wide-bandgap semiconductors [60, 61]. This allows the precise study of doping effects and their impact on the electrical characteristics of these materials, which is of utmost importance in state-of-the-art semiconductor science and technology [62, 63].

In one sentence, space-charge waves (SCW) can be described as eigenmodes of spacial-temporal oscillations of a space-charge density appearing in a system of traps and free carriers in semi-insulating solids when carriers move in an electric field [64]. SCW can be excited and detected via various methods, from which the most important are

1. running sinusoidal illumination pattern on a photorefractive crystal in a static electric field, using optical detection via the photorefractive effect [53],
2. static sinusoidal illumination pattern on a photorefractive crystal in an electric ac field, using optical detection via the photorefractive effect [55], and
3. sinusoidal illumination pattern with different movement patterns on photoelectric solids in a static electric field using electrical detection [58, 60].

The following explanations especially cover the latter version. For a more detailed description, one may refer to [19, 52]

For a theoretical description of the resonance behavior of SCW excitation, the band structure is described with a one-center model as depicted in figure 3.1. This configuration is well known, e. g. from holography [65–67].

The system essentially features the valence band (VB), the conduction band (CB) with the carrier density $n(x,t)$, a donor level with spatial and temporal dependent density $N_D(x,t)$ and an acceptor level with constant density N_A for charge compensation. The density of excited donors is described by $N_{D+}(x,t)$.

The dynamics of the system are usually described via the Kukhtarev or Kiev equations [68, 69]:

$$\partial_t n(x,t) = \frac{1}{e}\partial_x j(x,t) + g(x,t) - \frac{n(x,t)N_{D+}(x,t)}{\vartheta} \tag{3.1}$$

$$j(x,t) = \mu e n(x,t)E(x,t) + eD\partial_x n(x,t) \tag{3.2}$$

$$I(t) = \epsilon\epsilon_0\partial_t E(x,t) + j(x,t)_{,,} \tag{3.3}$$

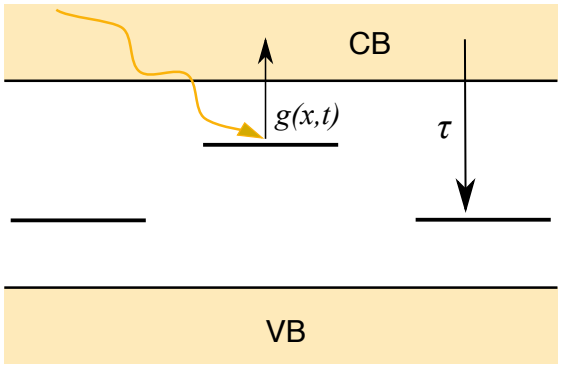

Figure 3.1: Energy-level diagram of a one center system. Electrons are excited by illumination with a generation rate $g(x,t)$ and a decay into traps after a mean relaxation time τ.

where $\partial_x = \partial/\partial_x$. Equation 3.1 is a rate equation for the energy levels, where e is the electron charge, $g(x,t)$ is the (in the presented case light-induced) generation rate, $\vartheta = \tau\,[N_A + n(t=0)]$ is the recombination rate and $j(x,t)$ is the current density described by equation 3.2. It consists of a field driven component proportional to the material-dependent carrier mobility μ and the electric filed and a diffusive component proportional to the density gradient a the diffusion constant D. Equation 3.2 is derived from the Poisson equation and the equation of continuity via integration and describes the spatially averaged total current density $I(t)$.

For low light intensities, i. e. outside the saturation region, $g(x,t)$ is proportional to the light intensity $W(x,t)$. Publication 3, that is part of this chapter, adepts the well-known solution model for oscillating illumination patterns

$$W_o(x,t) = W_0\Big(1 + m \cdot \cos\Big(Kx + \Theta\cos(\Omega t)\Big)\Big) \tag{3.4}$$

[70–73] to a new running pattern

$$W_r(x,t) = W_0\left(1 + \frac{m}{2}\cos(Kx) + \cos(Kx + \omega t)\right) \tag{3.5}$$

New effects in the resonance curve of the AC-current amplitude $\Delta I(\omega)$ are highlighted and explained.

Publication 4 uses $W_o(x,t)$, but extends the model for an external magnetic field perpendicular to the electric field and to the incidence of light. From a technological point of view, the influence of magnetic fields on SCWs is crucial for determining the Hall mobility of carriers. A closed solution for this system is presented and discussed. Experiments show remarkable agreement with the theoretical considerations.

3.1. Publications

In the field of space-charge wave spectroscopy, the author contributed to the following articles in scientific, peer-reviewed journals:

3. Hilling, B., T. Schemme, K.-M. Voit, H.-J. Schmidt, and M. Imlau. *"Space-charge Wave Excitation by Superposition of Static and Moving Interference Patterns."* Phys. Rev. B 80, no. 20 (November 23, 2009): 205118. doi:10.1103/PhysRevB.80.205118.

   Abstract: The optical excitation of space-charge waves (SCW) has been realized experimentally by superposition of static and moving light interference patterns with $Bi_{12}GeO_{20}$ as an example. A clear resonance behavior of the ac detected in an external electric circuit, as well as an inverse dispersion law, is verified, and a low frequency signal due to a modulation of the photoconductivity appears. The results are compared to the classical method using an oscillating light pattern for excitation. The optimized method allows for the detection of the charge carriers participating in SCW formation and yields an excitation of higher quality.

4. Petrov, D. V., A. V. Shamray, B. Hilling, K.-M. Voit, M. Lemmer, and M. Imlau. *"Orientational Dependencies of Space-charge Waves Under the Action of a Magnetic Field in GaAs:Cr."* Appl. Phys. B 103, no. 2 (May 1, 2011): 351–356. doi:10.1007/s00340-011-4490-7.

   Abstract: Space-charge wave (SCW) excitation is studied under the influence of an external magnetic field in GaAs:Cr depending on the orientational angle of the exciting oscillating sinusoidal interference pattern to the external electric field. It was found that the tilt of the SCW propagation direction induced by the magnetic field results in a shift of the orientational dependence curve. This feature allows determining the deviation angle of charge carriers' trajectory and their sign. A quantitative theoretical explanation of the effects is proposed and a theoretical expression for the SCW ac-current is given.

The abstracts are displayed with kind permission of the American Physical Society and the Springer-Verlag GmbH, Heidelberg. See appendix B on the inclusion of the full publications in the version at hand.

4. Photofunctional molecules

Photofunctional molecules feature functional reactions on certain light interaction. They may range from changes in the electronic structure, including ionization, to changes in the molecular configuration [74]. Especially the latter class inherits outstanding potential, for example in energy conversion and storage [75] or future computing applications. Today, optical data transfer and storage is already widely established [76, 77]. However, logic circuits still work on an electronic basis, necessitating optoelectronic bridges.

Using photoswitchable molecules allows to eliminate electronic, transistor-based components [78, 79], pioneering the third era of human automated computing, succeeding the mechanical [80–82] and the electronic generation[83–85]. On this background, comprehensive research has been conducted in the past years. Especially two advances necessitate an extensive review of existing spectroscopic models, which is given in publication 5 and applied to experimental data:

1. As desirable, most recent candidates, namely ruthenium-sulfoxide complexes, exhibit exceptional photochromic reactions. Consequently strong absorption dynamics during the pumping have to be taken into consideration.

2. By now, a state of research is reached in which industrial setups have to be taken into stronger consideration. While classical research setups feature a parallel alignment of pump and probe beam, most industrial applications require orthogonal alignment. The impact of these geometrical changes, especially in combination with the high absorption, has to be investigated theoretically.

Fundamentals, including the particular advantages of the molecules under consideration and their chemical structure, are given in the publication.

4.1. Publication

In the field of photofunctional molecules, the author contributed to the following article in a scientific, peer-reviewed journal:

5. Eicke, S., V. Dieckmann, A. Kruse, K.-M. Voit, L. Walder, and M. Imlau. *"Dynamics of the light-induced absorption in photochromic [Ru(bpy)$_2$(OSO)]$^+$"*
   Journal of Spectroscopy and Dynamics, 2013, *accepted 07 March 2013, publication imminent*

   Abstract: The dynamics of the light-induced absorption of a dense but fluid ensemble of photochromic [Ru(bpy)$_2$(OSO)]$^+$, that is determined within a pump-probe scheme, is analyzed by both, modeling and experimental investigations. The intensities of pump and probing beams are significantly attenuated by absorption involving the ground and photoisomerized states. Predictions of the derived model are (i) a dependence of the dynamics on the spatial position of the probing beam within the molecular ensemble, (ii) different dynamics for collinear or non-collinear propagation of pump- and probing beams and (iii) dynamics that depend on the molecular concentration of the ensemble. These predictions are experimentally verified in an appropriate pump-probe configurations along the boundary conditions of the model. We show that the findings can be successfully applied to analyze the temperature dependence of the dynamics of an ensemble of sulfoxide compounds. The relation of the model quantities to quantum yield and activation energy is discussed.

The abstract is displayed with kind permission of the Cognizure Corporation. See appendix B on the inclusion of the full publication in the version at hand.

5. Summary & Conclusion

Due to the cumulative nature of this thesis, all scientific novelties presented in the contained publications have been extensively introduced, discussed and summarized in the respective papers. Thus, a very short summary shall suffice here.

Chapter 2 ameliorates the theory of wave-coupling in thick holographic gratings by giving a full analytic description of out-of-phase complex-permittivity gratings. A quantitative discussion of the arising Borrmann effect is given. Furthermore, the theory is updated to modern terminology. A spectroscopic view is accentuated by accounting for the wavelength dependence of the involved quantities over the full optical range. In the unpublished-results section, some calculations on the phase behavior in the crystal during beam-coupling are presented.

In Chapter 3, the method of space-charge wave spectroscopy has been extended for the determination of the direction of carrier motion. Additionally, the influence of magnetic fields is investigated and theoretically described.

Chapter 4 examines the dynamics of light-induced absorption in ruthenium-sulfoxide complexes via pump-probe methods. The spectroscopic models have been adapted to the pronounced photochromic reaction of these molecules. Furthermore, a model for industrial $90°$ reading geometries has been developed and experimentally realized.

In the remaining part of the conclusion, I would like to catch up with the general thoughts raised in the introduction. In the publications compiled in this cumulative thesis, theoretical models from the field of nonlinear condensed-matter optics have not only been developed and discussed, but also linked to state-of-the-art experimental data. All topics share the fact that the established theoretical descriptions did not sufficiently cover modern experimental techniques and results. Most basic theories were developed in the 1960s and 1970s, which is shortly after the most important tool in modern optics, the laser, appeared. Since then, large parts of the theoretical optical community and the experimental one moved into different directions: While most theoreticians honed their models for precision at the cost of applicability and generality, experimentalists increased the complexity of their setups and faced a growing number of new effects. The results of this thesis were able to close this gap for some parts of the treated fields. It has been shown that the conjunction of empirical observation and sophisticated theoretical modeling, as described in the introduction, is still the central pillar of modern physics and should not be lost from sight.

A. Open access publications

The following publication are published open access and are available on the publisher's websites free of charge.

The paper published in MDPI Materials underlies the Creative Commons Attribution license. For the paper published in Optics Express, the copyright lies with the publisher.

Small-polaron based holograms in $LiNbO_3$ in the visible spectrum

H. Brüning * V. Dieckmann* B. Schoke* K.-M. Voit*
M. Imlau* G. Corradi† C. Merschjann‡

Published 29 May 2012

Published as **H. Brüning, V. Dieckmann, B. Schoke, K.-M. Voit, M. Imlau, G. Corradi, and C. Merschjann.** ***"Small-polaron Based Holograms in $LiNbO_3$ in the Visible Spectrum."*** in *Opt. Express 20, no. 12 (June 4, 2012): 13326–13336. doi:10.1364/OE.20.013326*.
©2012 Optical Society of America.

This paper was published in Optics Express and is made available as an electronic reprint with the permission of OSA. The paper can be found at the following URL on the OSA website: `http://dx.doi.org/10.1364/OE.20.013326`. Systematic or multiple reproduction or distribution to multiple locations via electronic or other means is prohibited and is subject to penalties under law.

Diffraction efficiency, relaxation behavior and dependence on pump-beam intensity of small-polaron based holograms are studied in thermally reduced, nominally undoped lithium niobate in the visible spectrum ($\lambda = 488\,\mathrm{nm}$). The pronounced phase gratings with diffraction efficiency up to $\eta = (10.8 \pm 1.0)\,\%$ appeared upon irradiation by single ns-laser pulses ($\lambda = 532\,\mathrm{nm}$) and are comprehensively assigned to the optical formation of spatially modulated densities of small bound $\mathrm{Nb}_{\mathrm{Li}}^{4+}$ electron polarons, $\mathrm{Nb}_{\mathrm{Li}}^{4+}$:$\mathrm{Nb}_{\mathrm{Nb}}^{4+}$ electron bipolarons, and O^{-} hole polarons. A remarkable quadratic dependence on the pump-beam intensity is discovered for the recording configuration $\mathbf{K} \parallel c$-axis and can be explained by the electro-optic contribution of the optically generated small bound polarons. We discuss the build-up of local space-charge fields via small-polaron based bulk photovoltaic currents.

*Department of Physics, University of Osnabrück, Osnabrück, Germany
†Wigner Research Centre for Physics, Budapest, Hungary
‡Helmholtz-Zentrum Berlin für Materialien und Energie GmbH, Berlin, Germany

1 Introduction

The recording of volume holograms in polar oxide crystals by means of optical formation of small bound polarons has been established as a novel type of hologram recording mechanism, with $LiNbO_3$ as an example, only recently [1]. An incoming fringe pattern is transferred to a population density hologram by exploiting the optical absorption, transport and strongly localized lattice distortion related with small bound polarons [2]. The concept of small-polaron based hologram formation has been developed to accelerate the hologram formation time in polar oxide crystals to the sub-μs-time regime as well as to enable a spectrally broad optical response from the visible to the near-infrared spectrum. Appropriate oxide crystals are inevitably required as hologram recording media for a variety of modern holographic applications like real-time holographic displays [3], volume holographic optical correlators [4] or tunable Bragg-filters for photonic networks [5]. In $LiNbO_3$, small polarons have formation times in the sub-ps time regime [6], thus, hologram recording with fs-, ps-, and ns-laser pulses can be expected. The respective small-polaron absorption features are broad (≈ 1 eV) and are positioned in the visible and near-infrared spectrum (2.5 eV, 1.6 eV and 1.0 eV) depending on the particular small polaron type [7, 8]. Thereby, an optical response for recording and reconstruction from 3.0 to 0.5 eV is likely.

So far, we have probed the polaron-based hologram features in the near-infrared spectrum ($\lambda = 785$ nm). This allowed us to uncover the dominating role of small bound Nb_{Li}^{4+} polarons (GP) in the appearance of mixed absorption and index volume gratings.

In this work, we focus on hologram features at a probing light wavelength of $\lambda = 488$ nm, i.e., a spectral range that is of utmost importance for a variety of modern holographic applications of $LiNbO_3$ such as real-time holographic displays [9]. The interest in the blue spectrum is particularly driven by our findings that hologram recording can be performed within a single 8 ns laser pulse while thermally-driven hologram self-decay takes place in the range of a few milliseconds at room temperature. Thus, thermally reduced $LiNbO_3$ represents a photosensitive, re-recordable hologram medium that is updatable at kHz frequencies.

From the point of view of small polarons, the blue spectrum is dominated by the presence of Nb_{Li}^{4+}:Nb_{Nb}^{4+} electron bipolarons (BP, absorption maximum at $\lambda \simeq 500$ nm) [7] and small O^- hole polarons (HP, $\lambda \simeq 500$ nm) [8]. These two kinds of polarons exhibit essentially different features with respect to light-matter-interaction: Bipolarons stable at room temperature, are dissociated (gated) optically by light exposure within a one-photon absorption process. The maximum addressable BP number density is determined by the respective number density in the ground state. In contrast, short-lived small bound hole polarons are generated via two-photon absorption. Their number density grows until all possible O^{2-} lattice sites, one in the vicinity of each Li vacancy, are saturated [8]. These processes can be easily distinguished experimentally by the study of the grating efficiency as a function of the pump-beam intensity.

We show that the hologram read-out in the visible spectrum can be comprehensively explained in the frame of a complex interplay of BP, HP and GP. In particular, we find an abnormal dispersive behavior that is due to the characteristic positions of the absorption

maxima of the small polarons involved. The dependence of the diffraction efficiency on the pump-beam intensity is mono-exponential for the case of probing the population saturation behavior of BP. In contrast, it follows a quadratic dependence without saturation behavior for the recording configuration that allows for a predominant electro-optic contribution. This finding can be explained by considering the presence of a small-polaron based bulk photovoltaic effect that is particularly related to the intrinsic defect structure. An analogous model to Fe-doped $LiNbO_3$ [10], that explains the build-up of localized electric space charge fields, is discussed.

With these results and our earlier findings [1], the recording of polaron-based holograms with ns-laser pulses in $LiNbO_3$ is demonstrated over a broad range in the visible spectrum. Further impact of the work is revealed by considering the possibility of recording with fs- and ps-laser pulses, thus enabling fs-holography. Also, we like to point to the possible transfer of the polaron concept for hologram recording to other oxide crystals like $KNbO_3$ [11].

2 Samples and experimental setup

Our studies were performed with single crystals of thermally reduced lithium niobate grown from a congruent, nominally undoped melt via Czochralski growth technique (Crystal Technology, Inc.). The sample under study (cf. Ref. [1]) with aperture $(a \times c) = (6.54 \pm 0.01) \times (5.69 \pm 0.01)\,\mathrm{mm}^2$ and thickness $d = (1.23 \pm 0.03)\,\mathrm{mm}$ has been thermally pre-treated by heating it for 6 hours at $T = (970 \pm 10)\,\mathrm{K}$ in a reducing atmosphere of $p < 10^{-4}\,\mathrm{mbar}$. Thus, high densities of $\mathrm{Nb}_{\mathrm{Li}}^{4+}$:$\mathrm{Nb}_{\mathrm{Nb}}^{4+}$ bipolarons (BP) and of small bound $\mathrm{Nb}_{\mathrm{Li}}^{4+}$-polarons (GP) [12, 13] were generated that are stable at room temperature. We have calculated the number densities N_{BP} and N_{GP} using the steady-state absorption for extraordinary light polarization at $\lambda = 488\,\mathrm{nm}$ and $\lambda = 785\,\mathrm{nm}$ and the absorption cross sections published in Refs. [1, 14]. All relevant parameters are summarized in Table 1.

Table 1: Absorption features and polaron number densities of the reduced lithium niobate sample under study in the steady state at room temperature. The sample is identical to the one used in Ref. [1].

sample properties and polaronic features	
crystal thickness d	$(1.23 \pm 0.03)\,\mathrm{mm}$
Fe content	$c_{\mathrm{Fe}} < 5\,\mathrm{ppm}$
$\alpha(488\,\mathrm{nm})$	$(667 \pm 30)\,\mathrm{m}^{-1}$
$\alpha(785\,\mathrm{nm})$	$(270 \pm 10)\,\mathrm{m}^{-1}$
N_{BP}	$(56 \pm 10)\cdot 10^{22}\,\mathrm{m}^{-3}$
N_{GP}	$(26 \pm 7)\cdot 10^{22}\,\mathrm{m}^{-3}$

Hologram recording and time-resolved detection of the hologram decay were per-

formed in a two-beam interferometer setup. A single pulse of a frequency-doubled YAG:Nd-laser (Innolas *Spitlight 600*, $\lambda_\mathrm{p} = 532\,\mathrm{nm}$ and average pulse duration $\tau_\mathrm{FWHM} \approx 8\,\mathrm{ns}$) was used for recording an unslanted volume grating (equal intensities $I_\mathrm{R} = I_\mathrm{S}$, parallel light polarization $\mathbf{e_R} = \mathbf{e_S}$, modulation depth $m = 1$, Bragg angle $\Theta_\mathrm{B} = 6.3°$). The decay of the grating was probed in the blue-green spectral range with the Bragg-matched beam of a continuous-wave laser at $\lambda_\mathrm{t} = 488\,\mathrm{nm}$ (Coherent *Sapphire*, $I_0 = 10\,\mathrm{kW/m^2}$). Time-dependent data collection via a Si-PIN diode and digital storage oscilloscope was limited to the range $1\,\mu\mathrm{s}$ $-100\,\mathrm{s}$ in order to suppress unwanted signal contributions from thermal gratings [15]. The sample temperature was adjusted by a PID-controlled thermoelectric element from room temperature up to 410 K.

3 Experimental results

Figure 1 depicts the temporal dynamics of the intensity of the first order diffracted probe beam obtained upon hologram recording with a single 8 ns-laser pulse. The intensity $I^{(1\mathrm{st})}(t)$, plotted on a logarithmic time scale, is normalized to the intensity of the incoming probe beam I_0 taking into account Fresnel reflection and thus corresponds to the efficiency η of the diffraction process. The light polarizations of pump and

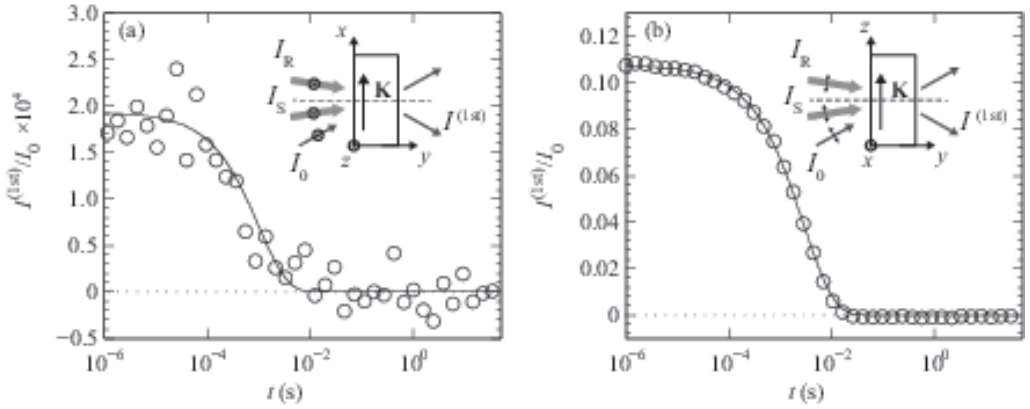

Figure 1: Semilogarithmic plot of the temporal dynamics of the normalized intensity of the first order diffracted beam $I^{(1\mathrm{st})}/I_0$ for (a) $\mathbf{K} \perp c$-axis (s-polarization) and (b) $\mathbf{K} \parallel c$-axis (p-polarization). Recording conditions: $\lambda_\mathrm{p} = 532\,\mathrm{nm}$, $\mathbf{e}_\mathrm{p} \parallel c$-axis and Bragg angle $\Theta_\mathrm{B} = 6.3°$. $I_\mathrm{p} = I_\mathrm{R} + I_\mathrm{S} = 380\,\mathrm{GW/m^2}$. Bragg-matched probing conditions: $\lambda = 488\,\mathrm{nm}$, $\mathbf{e} \parallel c$-axis. The solid lines correspond to fits of Eq. (1) to the data. The insets sketch the respective recording and probing configurations.

probe beams were aligned parallel to the polar c-axis of the sample corresponding to s-polarization in configuration (a) and p-polarization in configuration (b). The grating vector of the recorded hologram $\mathbf{K}$ was chosen either perpendicular (a) or parallel (b) to the c-axis as sketched in the insets. Thereby, in configuration (a) the corresponding

elements of the electro-optic ($r_{331} = 0$) and photovoltaic tensor ($\beta_{133} = 0$) equal zero, whereas in configuration (b) they are non-zero ($r_{223} \neq 0$, $r_{333} \neq 0$, $\beta_{311} \neq 0$, $\beta_{333} \neq 0$) [16]. All experiments were performed for a Bragg-matched read-out beam. Higher diffraction orders were not observed. This accords with our previous findings on the rocking curve that unambiguously verified the presence of a volume grating for this type of hologram recording mechanism and set of recording parameters [1].

Qualitatively, both gratings decay with a similar temporal dependence. The striking observation in the two spectra is the severely different starting amplitude at $t = 1\mu$s of the diffraction efficiency that is by a factor of approximately 500 larger in configuration (b) compared with (a). Fitting a stretched exponential function:

$$\frac{I^{(1\mathrm{st})}(t)}{I_0} = \frac{I^{(1\mathrm{st})}(t=0)}{I_0} \exp\left[-\left(\frac{t}{\tau}\right)^{\beta}\right] \tag{1}$$

to the experimental data (solid lines) yields the starting amplitudes $I^{(1\mathrm{st})}(t = 1\mu\mathrm{s})/I_0$, the decay time constant τ and the stretching factor β as summarized in Table 2. We note that Eq. (1) accords with the empirical dielectric decay function introduced by Kohlrausch, Williams and Watts (KWW) [17].

Table 2: Parameters obtained from fitting Eq. (1) to the experimental data depicted in Fig. 1 and of Eq. (6) to the data in Fig. 2.

	$\mathbf{K} \perp c$-axis	$\mathbf{K} \parallel c$-axis
$I^{(1\mathrm{st})}(t = 1\mu\mathrm{s})/I_0$	$(1.9 \pm 0.8) \cdot 10^{-4}$	(0.108 ± 0.010)
τ	(1.0 ± 0.3) ms	(2.78 ± 0.30) ms
β	(0.78 ± 0.20)	(0.73 ± 0.10)
$\eta^{\mathrm{sat.}}$	$(1.8 \pm 0.8) \cdot 10^{-4}$	
I_c	$(52 \pm 10)\,\mathrm{GW/m^2}$	

In the next step, we have studied the dependence of the starting amplitude on the intensity of the recording beams, see Fig. 2. We find that the diffraction efficiency saturates at a value of about $1.8 \cdot 10^{-4}$ and pump beam intensities larger than $\approx 200\,\mathrm{GW/m^2}$ using the recording configuration (a). In contrast, $I^{(1\mathrm{st})}(t = 1\mu\mathrm{s})/I_0$ increases as a function of I_p in a superlinear way for configuration (b), i.e., saturation is not observed up to the maximum available pump beam intensity of $380\,\mathrm{GW/m^2}$.

According to these findings, we need to verify the relation between the recorded gratings and the optically-induced formation of small polarons for configuration (b). For this purpose, the activation energy related to the grating decay has been determined by means of temperature dependence measurements $\tau(T)$ in a range of 300 K to 410 K. Performing an Arrhenius plot a linear dependence is found allowing for the determination of the activation energy to $E_\mathrm{A} = (0.57 \pm 0.07)$ eV. This value can be compared with literature values for the activation energies of different types of small polarons in $LiNbO_3$ and points to the activation energy of the small bound electron polaron, Nb_{Li}^{4+}

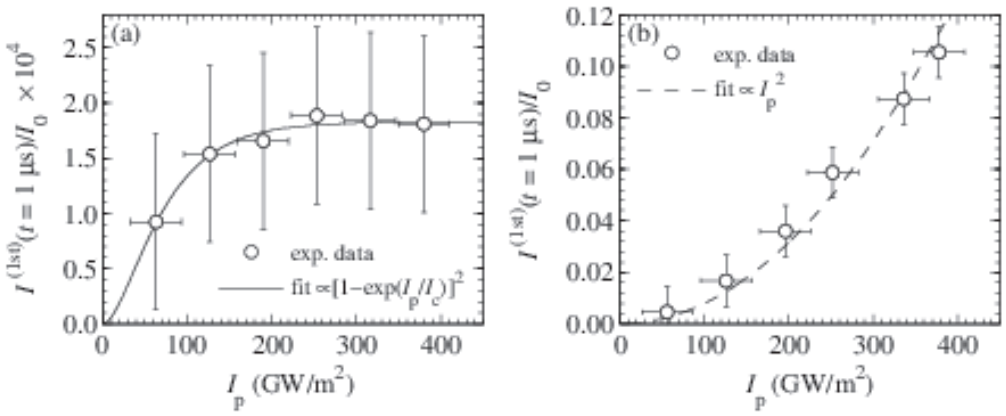

Figure 2: Normalized intensity of the first order diffracted beam $I^{(1\mathrm{st})}/I_0$ at $t = 1\,\mu$s as a function of pump intensity I_p for (a) $\mathbf{K} \perp c$-axis (*s*-polarization) and (b) $\mathbf{K} \parallel c$-axis (*p*-polarization) using the same recording and probing condition as in Fig. 1. The solid line corresponds to a fit of a saturation function Eq. (6) while the dashed line represents a fit of a quadratic intensity dependence to the data.

for which Schirmer *et al.* obtained a value of 0.62 eV from conductivity measurements [18].

4 Discussion

Our results highlight the prominent features of polaron-based holograms in the visible spectrum in thermally reduced lithium niobate. For the field of applications, the striking features are the diffraction efficiency of $\eta = (0.108 \pm 0.01)$ by means of single 8 ns-laser pulse recording ($I_\mathrm{p} = 380\,\mathrm{GW/m^2}$) and the hologram self-decay within a few miliseconds at room temperature. Taking into account the crystal thickness of $d = 1.23\,\mathrm{mm}$ this corresponds to a photosensitivity [19] of:

$$S|_\mathrm{ns}^{488\,\mathrm{nm}} = \frac{\delta\sqrt{\eta}}{\delta t}\frac{1}{I_\mathrm{p} d} \simeq 8.4\,\mathrm{cm/J} \quad , \tag{2}$$

i.e. a value that is by one order of magnitude larger compared with holograms recorded via the photorefractive effect [19, 20].

From the point of view of small polarons, there are two outstanding findings associated with the visible spectrum:

- The amplitude of the diffraction efficiency at 488 nm is reduced by a factor of two in comparison with probing at 785 nm, i.e. an abnormal dispersion behavior is found.

- The intensity dependence of the diffraction efficiency is qualitatively different for the recording geometries $\mathbf{K} \perp c$ and $\mathbf{K} \parallel c$. We will discuss these two findings below along the expectations for polaron-based hologram recording in the visible.

The further properties have already been reported for the near-infrared spectral range [1] and give strong evidence for the polaronic origin of the hologram recording and read-out process:

- ▷ a stretched-exponential decay of the diffraction efficiency,
- ▷ a hologram lifetime in the ms-range,
- ▷ a thermally activated hologram decay,
- ▷ an activation energy of the latter that corresponds to the activation energy of the small bound $\mathrm{Nb}_{\mathrm{Li}}^{4+}$ polaron and
- ▷ a pronounced dependence of the diffraction efficiency on the recording geometry.

We should like to note the assumptions made in the following discussion: First, the action of extrinsic defect centers, that foster hologram recording via the photorefractive effect, is not considered [21]. This is justified because the number density of extrinsic photorefractive/transition metal centers, such as Fe, is far below 5 ppm in our nominally undoped $LiNbO_3$ samples [14]. Furthermore, the thermal reduction pre-treatment results in a considerable transfer of the valence state from acceptor to donor levels. For instance, the number density of Fe^{3+} is considerably damped $c(\mathrm{Fe}^{3+}) \ll 1$, but it is decisive for the photorefractive response as the amplitude of the index change is linearly dependent on $c(\mathrm{Fe}^{3+})$ [22]. Second, the role of small free $\mathrm{Nb}_{\mathrm{Nb}}^{4+}$ electron polaron densities is neglected because of their sub-μs-lifetime [23] and the chosen limitation of the temporal dynamics to the time range $t \geq 1\mu$s.

4.1 Hologram recording by spatially modulated polaron densities

Exposure to a spatially modulated intensity pattern $I(x) = I_{\mathrm{p}}[1 + \cos(|\mathbf{K}|x)]$ results in the appearance of spatially modulated polaron densities. Densities $N_{\mathrm{GP,HP}}$ of small bound electron and small hole polarons are increased in the bright region of the fringe pattern while the bipolaron density N_{BP} is diminished in the same regions. In the dark regions there are no changes of polaron densities. The formation time of the small polaron density is limited by a sequence of processes starting from the optical excitation of a charge-carrier by absorption and ending with self-localization at a $\mathrm{Nb}_{\mathrm{Li}}^{5+}$-site via electron-phonon coupling. The period in-between is characterized by coherent electron transport in the conduction band. Because of its coherence in the presence of electron-lattice coupling this intermediate state can be regarded as a large polaron. The formation time of small free polarons at room temperature has been reported for Mg-doped $LiNbO_3$ to ≈ 110 fs [6] while small bound polarons appear within 400 fs [24] after the optical pulse. If the duration of illumination exceeds the polaron formation

time, a repetitive excitation of charge carriers from localized states becomes possible. Thereby, the distance of the small polaron with respect to the initial polaron site can be increased significantly. This may affect the appearance of polaron-based photovoltaic currents (cf. section (4.4)), or the dynamics of the hologram recording process.

As the polaron densities are related to the polaron absorptions $\alpha_{\mathrm{GP,HP,BP}}$ of the respective types by constant factors (the absorption cross sections $\sigma_{\mathrm{GP,HP,BP}}$), the polaron absorptions become spatially modulated and together yield the overall absorption modulation $\alpha(x)$ with amplitude α_1 around a mean value $(\alpha_0 + \alpha_1)$ in a crystal with ground state absorption α_0 of the unexposed sample (see Fig. 3(a)). This absorption modulation

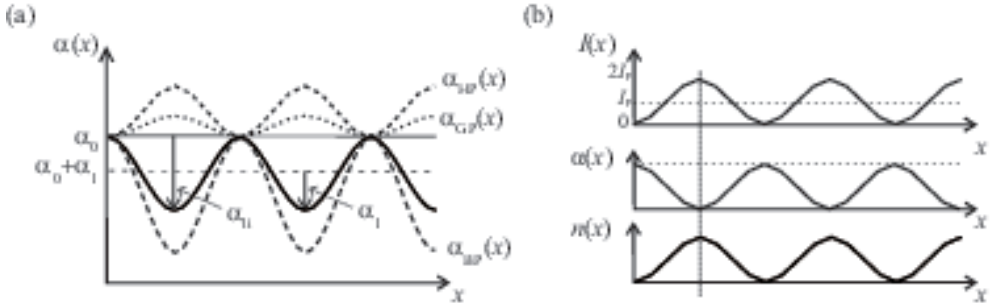

Figure 3: (a) Spatial modulation of the absorption coefficient $\alpha(x)$ with amplitude α_1 and average value of $\alpha_0 + \alpha_1$. The overall absorption change in the maximum of the fringe pattern α_{li} is assembled from absorption changes of the individual polaron types: $\alpha_{\mathrm{GP,HP,BP}}$. All absorption contributions are related to $\lambda = 488\,\mathrm{nm}$ and extraordinary light polarization.
(b) Sinusoidal intensity pattern $I(x)$ applied for exposure with average intensity $I_{\mathrm{p}} = I_{\mathrm{R}} + I_{\mathrm{S}}$ and modulation depth unity resulting in a modulated density of polarons and, therefore, a modulated change of absorption $\alpha(x)$. This modulated absorption change is linked to a modulated change of the index of refraction $n(x)$ via the Kramers-Kronig relation as shown in Fig. 7 in Ref. [1].

is causally related to a spatial modulation of the index of refraction $n_1(x)$ (see Fig. 3(b)), i.e., by considering the interplay of the different polaron density modulations, we end up with a population density grating. Its diffraction efficiency is determined from the maximum amplitude of the change of the complex susceptibility arising from the optical generation of small polarons.

4.2 Dispersion of diffraction efficiency

The energetic positions and bandwidths of the absorption features of the small polarons involved [7, 8], their absorption cross sections [14] and dependence on the pump beam intensity [12] are well documented in literature. Hence, it is possible to estimate the maximum value of the absorption change ($\equiv 2\alpha_1 = \alpha_{\mathrm{li}}$) for the sample under study and applied pump beam intensity as a function of wavelength (see Fig. 7 in Ref. [1]).

As a result, we find $\alpha_1(488\,\mathrm{nm}) = (-40 \pm 15)\,\mathrm{m}^{-1}$ at $\lambda = 488\,\mathrm{nm}$, so that the light fringe pattern $I(x)$ and the spatial absorption modulation $\alpha(x)$ are phase-shifted by π with respect to each other, as depicted in Fig. 3(b). At the same time, the knowledge of the dispersive absorption features allows for the calculation of the causally related changes $n_1(\lambda)$ of the index of refraction via Kramers-Kronig-relation [25]. It yields $n_1(488\,\mathrm{nm}) = (-3.4 \pm 1.0) \cdot 10^{-6}$ and a spatial modulation of the index of refraction $n(x)$ that is in phase with $I(x)$ (Fig. 3(b)). The modulations $\alpha(x)$ and $n(x)$ resemble a mixed diffraction grating with efficiency η that is given by Kogelnik's coupled wave theory [26]:

$$\begin{aligned} \eta(\lambda) &= \exp\left(\frac{-2\left(\alpha_0(\lambda)+\alpha_1(\lambda)\right)d_\mathrm{h}}{\cos\Theta_\mathrm{B}}\right) \\ &\quad \times\left[\sin^2\left(\frac{\pi n_1(\lambda)d_\mathrm{h}}{\lambda\cos\Theta_\mathrm{B}}\right)+\sinh^2\left(\frac{\alpha_1(\lambda)d_\mathrm{h}}{2\cos\Theta_\mathrm{B}}\right)\right]. \end{aligned} \tag{3}$$

Here, $d_\mathrm{h} \leq d$ denotes the effective thickness of the recorded hologram and d is the thickness of the crystal. At 488 nm, we end up with an estimate for the diffraction efficiency $\eta^{\mathrm{est.}}(488\,\mathrm{nm}) = (0.7 \pm 1.0) \cdot 10^{-4}$ with $\alpha_0(488\,\mathrm{nm}) = (667 \pm 30)\,\mathrm{m}^{-1}$ and $d_\mathrm{h} = (0.61 \pm 0.07)$ mm taken from Ref. [1]. We have taken into account absorption losses in the crystal volume $(d - d_\mathrm{h})$ due to the reduced effective grating thickness. This corresponds to an additional absorption factor not included in Eq. (3) that results in an estimated diffraction efficiency of $\eta^{\mathrm{est.}}(\lambda) = \eta(\lambda) \cdot [\exp(-2(\alpha_0 + \alpha_1)(d - d_\mathrm{h})/\cos\Theta_\mathrm{B})]$. Deviations from a sinusoidal intensity pattern due to scattering, beam profile inhomogeneities and the reported nonlinear response of $\alpha_\mathrm{li}(I_\mathrm{p})$ on the pump intensity are neglected.
In Fig. 4(a), we have plotted the dependence $\eta^{\mathrm{est.}}(\lambda)$ (black line). The experimentally determined values for probing wavelengths 488 nm (△) and 785 nm (□) and $\mathbf{K} \perp c$-axis have been added for comparison. A good agreement between the estimate and experimental data is found. Moreover, we should like to point out the considerable decrease of the diffraction efficiency from the near-infrared to the blue spectral range in the estimated spectrum. It is a result of the rather different positions of the absorption features of the small polarons involved. In detail, both the index grating with $n_{1,\mathrm{BP}}$ and the absorption grating with $\alpha_{1,\mathrm{GP}}$ related to bipolaron and bound polaron density alterations, respectively, likewise contribute to the diffraction efficiency at 488 nm. The hole polaron density can be neglected. In contrast, it was shown that the diffraction efficiency at 785 nm is mainly due to the action of the absorption amplitude related to the small bound $\mathrm{Nb}_\mathrm{Li}^{4+}$ polaron (center of absorption feature at 1.6 eV), i.e., the contribution of $n_{1,\mathrm{GP}}$ and of susceptibility changes related to bipolarons and hole polarons could be neglected [1]. This fact is highlighted in Fig. 4(b) by the dispersion of the ratio of the diffraction efficiency for a pure absorption grating and a pure index grating $\eta(n_1 = 0)/\eta(\alpha_1 = 0)$. As the estimate of the diffraction efficiency only slightly depends on the direction of the grating vector, with a correction of $\cos(2\theta_\mathrm{B}) \approx 0.96$ for p-polarization and probing wavelength 488 nm [26], it is valid for both recording configurations under study.

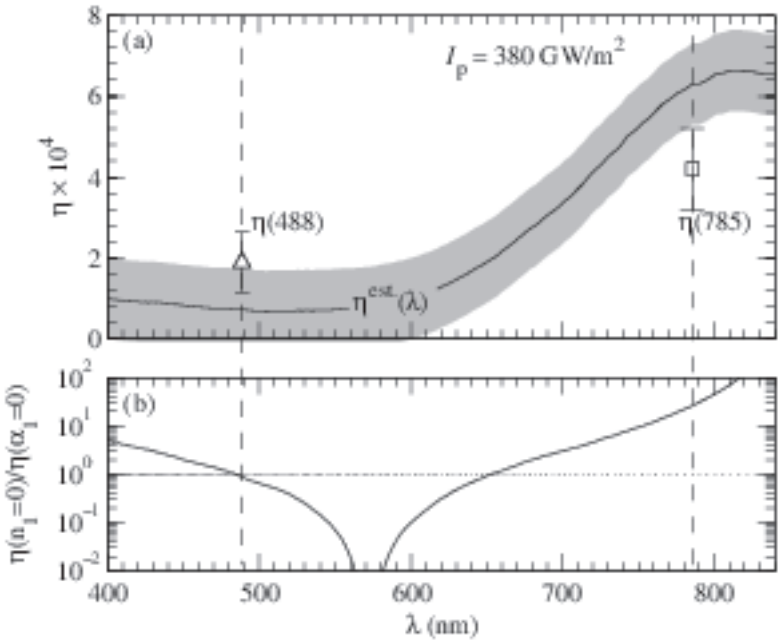

Figure 4: (a) Dispersion of the diffraction efficiency $\eta^{\mathrm{est.}}(\lambda)$ (solid line) that has been estimated according to Eq. (3) and the parameters published in Ref. [1]. The grey area denotes the error for $\eta^{\mathrm{est.}}(\lambda)$. The experimentally determined efficiencies at a probing wavelength of 488 nm (△, this work) and 785 nm (□, Ref. [1]) have been added for comparison. (b) Dispersion of the ratio of the diffraction efficiency for a pure absorption grating and a pure index grating. A predominant contribution of the absorption grating is found at 785 nm while amplitude and index grating likewise contribute to the overall efficiency at 488 nm.

4.3 Intensity dependence of diffraction efficiency

The key in understanding the saturation behavior of the diffraction efficiency at 488 nm as a function of pump beam intensity (Fig. 2(a)) is the intensity dependence of the small polaron densities involved in the hologram recording process, i.e., of bipolarons and bound polarons. According to our model, the bipolaron density is reduced via optical gating processes in the bright regions of the fringe pattern and yields an increase of the number density of small bound polarons by $N_{\mathrm{li,GP}}$ with

$$N_{\mathrm{li,GP}} = 2N_{\mathrm{li,BP}} \quad . \tag{4}$$

Here, $N_{\mathrm{li,BP}}$ denotes the number density of optically gated bipolarons. Because of the limited number density of bipolarons N_{BP} in the groundstate, a saturation behavior according to

$$N_{\mathrm{li,BP}} = N_{\mathrm{BP}} \left[1 - \exp\left(\frac{-I_{\mathrm{p}}}{I_{\mathrm{c}}} \right) \right] \tag{5}$$

is to be expected and has been experimentally verified by means of the intensity dependence of the light-induced, transient absorption at 488 nm in Ref. [12]. Because of the relation given by Eq. (4), the intensity dependence of small bound polarons shows saturation with the same characteristic intensity I_c, but an amplitude by a factor of two larger compared with Eq. (5). Furthermore, the absorption amplitude and the increase of polaron number density are directly linked via the absorption cross section. Hence, saturation as a function of pump beam intensity also appears for the amplitudes $\alpha_{1,\mathrm{BP,GP,HP}}$ and, taking into account Kramers-Kronig relation, for $n_{1,\mathrm{GP,BP,HP}}$. The latter enter equation Eq. (3), so that the diffraction efficiency inevitably shows saturation, as well. For small amplitudes α_1, n_1 and $\alpha_1 \ll \alpha_0$, we can approximate

$$\eta(I_\mathrm{p}) \approx (c_1 n_1(I_\mathrm{p}))^2 + (c_2 \alpha_1(I_\mathrm{p}))^2 = \eta^{\mathrm{sat.}} \left[1 - \exp\left(\frac{I_\mathrm{p}}{I_\mathrm{c}}\right)\right]^2 \quad . \tag{6}$$

The function is determined by only two fitting parameters: the saturation value $\eta^{\mathrm{sat.}}$, and the characteristic intensity I_c. Obviously, the fit can be applied to describe the intensity behavior within the error bars as depicted by the solid line in Fig. 2. The resulting fitting parameters are summarized in Table 2, the characteristic intensity I_c is of the same order of magnitude as the characteristic intensity of the light-induced absorption as reported in Ref. [12].

4.4 Dependence on the recording configuration

Understanding the dependence of the diffraction efficiency on the recording configuration $\mathbf{K} \perp c$-axis and $\mathbf{K} \parallel c$-axis remains a challenging task. While the situation for $\mathbf{K} \perp c$-axis is completely explained in the model of a spatially modulated polaron density, further physical processes need to be taken into account to model the results for $\mathbf{K} \parallel c$-axis. It is reasonable to assign the pronounced increase of the diffraction efficiency to the action of the linear electro-optic effect because $r_{331} = 0$, $r_{223} \neq 0$, and $r_{333} \neq 0$. Moreover, a predominant contribution of the index grating over the absorption grating is inferred from the efficiency exceeding the theoretical limit $3.7\,\%$ of pure lossy gratings. As a consequence, the build-up of an electric field with light exposure is required. At the same time, the stretched-exponential grating decay and its temperature dependence with an activation energy of $E_\mathrm{A} = (0.57 \pm 0.07)\,\mathrm{eV}$ unambiguously assign the temporal behavior of the diffraction signal to the decay of a spatially modulated density of small bound $\mathrm{Nb}_\mathrm{Li}^{4+}$ polarons. Thus, a relation between the small polaron density and the electric field, both spatially modulated along the direction of $\mathbf{K}$, must be postulated. The electric field strength that modulates the index with amplitude $n_1 = (-2.0 \pm 0.5) \cdot 10^{-4}$ can be estimated via $E = -2n_1/(n_\mathrm{e}^3 r_{333})$ (cf. Ref. [1]). With $n_\mathrm{e}(488\,\mathrm{nm}) = (2.2556 \pm 0.0005)$ [27] and $r_{333}(488\,\mathrm{nm}) = 34.4\,\mathrm{pm/V}$ [28] we get $E \approx 10\,\mathrm{kV/cm}$ that is much larger than the saturation field for diffusion transport mechanisms $E_\mathrm{diff} = (k_\mathrm{B}T/e)(2\pi/\Lambda) \approx 0.67\,\mathrm{kV/cm}$. Hence, a photovoltaic transport mechanism can be concluded, similar to the small polaron based model approach that explains the bulk photovoltaic effect in Fe-doped $LiNbO_3$ [10].

As a consequence of this conclusion, the electric field E and thereby n_1 must show a dependence on the pump beam intensity I_p. In fact, the photovoltaic current density is given by $j_\mathrm{phv} \sim \beta I_\mathrm{p}$ with the effective element of the photovoltaic tensor β. The dependence $n_1(I_\mathrm{p})$ is reflected by the data in Fig. 2(b), where a pronounced increase of the diffraction efficiency η on the pump beam intensity is depicted. Here we note, that η can be approximated by $\eta \sim n_1^2$ for small amplitudes n_1 according to Eq. (3), i.e., $\eta = a \cdot I_\mathrm{p}^2$ for a linear dependence of n_1 on I_p. Therefore, we have fitted a quadratic function to the experimental data (dashed line in Fig. 2(b)) obtaining $a = (8 \pm 1) \cdot 10^{-25}\,\mathrm{m}^4/\mathrm{W}^2$. Good agreement between the fit and the experimental data is found over a broad range of intensities, thus additionally supporting the conclusion of a bulk photovoltaic effect related to the optical formation of small polarons that is at the origin of the hologram recording mechanism for the configuration $\mathbf{K} \parallel c$-axis.

We finally note that nonlinearities of the diffraction efficiency are reported in photorefractive-recording of holograms with ns-laser pulses in transition-metal doped $LiNbO_3$, as well [29]. Contrary to solely polaron-based hologram recording, the simultaneous interplay of carriers excited from intrinsic and extrinsic defect centers needs to be considered. Thereby, an intensity limit of the nonlinearity results that represents a striking difference to our findings.

5 Conclusion

In conclusion, polaron-based recording of holograms in $LiNbO_3$ is verified in the visible spectrum. It obeys characteristic features that distinguish the recording process clearly from laser pulse recording via the photorefractive effect involving extrinsic traps [30–32], but can be closely related to the early findings of Schirmer and von der Linde [33, 34]. A remarkable hologram recording sensitivity of $S = 8.4\,\mathrm{cm/J}$ being nonlinearly dependent on the pump beam intensity is verified. Our results clearly indicate the impact of small bound polarons as optically addressable quasi-particles that have, so far, been identified as metastable intermediate centers in photorefractive two-step recording mechanisms [35–37]. All results underline the validity of our small polaron approach for the recording of volume holograms in $LiNbO_3$. Taking into account the formation time of small polarons in the sub-ps regime [6, 24, 38], the small polaron approach may be also applied for fs-holography.

From the materials' point of view, nominally undoped $LiNbO_3$ becomes more attractive as hologram material for modern holographic applications, including real-time holographic displays. It can be expected that equivalent recording mechanisms are present for a variety of other oxide crystals, as well. For instance, pronounced small polaron densities can also be generated by single laser pulses in $KNbO_3$ and $BaTiO_3$ [11].

Acknowledgment

The authors thank Gerda Cornelsen and Werner Geisler for sample preparation and the Deutsche Forschungsgemeinschaft (projects IM37/5, INST 190/137-1) and the Deutscher Akademischer Austausch Dienst in cooperation with the Hungarian Scholarship Board Office (projects 50445542, 54377942 and P-MÖB/840 and 29696) for financial support.

References

[1] M. Imlau, H. Brüning, B. Schoke, R.-S. Hardt, D. Conradi, and C. Merschjann, "Hologram recording via spatial density modulation of $Nb_{Li}^{4+/5+}$ antisites in lithium niobate," Opt. Express **19**, 15322–15338 (2011).

[2] D. Emin, "Polaron" in *McGraw-Hill Encyclopedia of Science and Technology*, (McGraw-Hill, New York, 2007) 125

[3] P.-A. Blanche, A. Bablumian, R. Voorakaranam, C. Christenson, W. Lin, T. Gu, D. Flores, P. Wang, W.-Y. Hsieh, M. Kathaperumal, B. Rachwal, O. Siddiqui, J. Thomas, R. A. Norwood, M. Yamamoto, and N. Peyghambarian, "Holographic three-dimensional telepresence using large-area photorefractive polymer," Nature **468**, 80–83 (2010).

[4] C. Gu, . Fu, and J.-R. Lien, "Correlation patterns and cross-talk noise in volume holographic optical correlators," J. Opt. Soc. Am. A **12**, 861–868 (1995).

[5] D. Sadot and E. Boimovich, "Tunable optical filters for dense wdm networks," Communications Magazine, IEEE **36**, 50 –55 (1998).

[6] Y. Qiu, K. B. Ucer, and R. T. Williams, "Formation time of a small electron polaron in $LiNbO_3$: measurements and interpretation," Phys. Status Solidi C **2**, 232–235 (2005).

[7] O. F. Schirmer, M. Imlau, C. Merschjann, and B. Schoke, "Electron small polarons and bipolarons in $LiNbO_3$," J. Phys.: Condens. Matter. **21**, 123201 (2009).

[8] O. F. Schirmer, "O^- Bound small polarons in oxide materials," J. Phys.: Condens. Matter **18**, R667–R704 (2006).

[9] S. Tay, P.-A. Blanche, R. Voorakaranam, A. V. Tunc, W. Lin, S. Rokutanda, T. Gu, D. Flores, P. Wang, G. Li, P. St Hilaire, J. Thomas, R. A. Norwood, M. Yamamoto, and N. Peyghambarian, "An updatable holographic three-dimensional display," Nature **451**, 694–698 (2008).

[10] O. F. Schirmer, M. Imlau, and C. Merschjann, "Bulk photovoltaic effect of $LiNbO_3$:Fe and its small-polaron-based microscopic interpretation," Phys. Rev. B **83**, 165106 (2011).

[11] S. Torbruegge, M. Imlau, B. Schoke, C. Merschjann, O. F. Schirmer, S. Vernay, A. Gross, V. Wesemann, and D. Rytz, "Optically generated small electron and hole polarons in nominally undoped and Fe-doped $KNbO_3$ investigated by transient absorption spectroscopy," Phys. Rev. B **78**, 125112 (2008).

[12] C. Merschjann, B. Schoke, and M. Imlau, "Influence of chemical reduction on the particular number densities of light–induced small electron and hole polarons in nominally pure $LiNbO_3$," Phys. Rev. B **76**, 085114 (2007).

[13] J. Koppitz, O. F. Schirmer, and A. I. Kuznetsov, "Thermal dissociation of bipolarons in reduced undoped $LiNbO_3$," Europhys. Lett. **4**, 1055–1059 (1987).

[14] C. Merschjann, B. Schoke, D. Conradi, M. Imlau, G. Corradi, and K. Polgar, "Absorption cross sections and number densities of electron and hole polarons in congruently melting $LiNbO_3$," J. Phys.: Condens. Matter **21**, 015906 (2009).

[15] F. Jermann and K. Buse, "Light-induced thermal gratings in $LiNbO_3$:Fe," Appl. Phys. B **59**, 437–443 (1994).

[16] R. S. Weis and T. K. Gaylord, "Lithium niobate: summery of physical properties and crystal structure," Appl. Phys. A **37**, 191–203 (1985).

[17] G. Williams and D. C. Watts, "Non–symmetrical dielectric relaxation behaviour arising from a simple empirical decay function," Trans. Faraday. Soc **66**, 80–85 (1970).

[18] O. F. Schirmer, H.-J. Reyher, and M. Woehlecke, "Characterization of point defects in photorefractive oxide crystals by paramagnetic resonance methods" in *Insulting Materials for Optoelectronics: New Developments*, (World Scientific Publishing, Singapore, 1995), 93–124.

[19] L. Hesselink, S. S. Orlov, A. Lie, A. Akella, D. Lande, and R. R. Neurgaonkar, "Photorefractive materials for nonvolatile volume holographic data storage," Science **282**, 1089 (1998).

[20] K. Buse, "Light-induced charge transport processes in photorefractive crystals II: Materials," Appl. Phys. B **64**, 391–407 (1997).

[21] M. Imlau, "Defects and photorefraction: A relation with mutual benefit," Phys. Status Solidi A **204**, 642–652 (2007).

[22] J. Imbrock, S. Wevering, K. Buse, and E. Krätzig, "Nonvolatile holographic storage in photorefractive lithium tantalate crystals with laser pulses," J. Opt. Soc. Am. B **16**, 1392–1397 (1999).

[23] D. Conradi, C. Merschjann, B. Schoke, M. Imlau, G. Corradi, and K. Polgár, "Influence of Mg doping on the behaviour of polaronic light-induced absorption in $LiNbO_3$," Phys. Stat. Sol. RRL **2**, 284–286 (2008).

[24] O. Beyer, D. Maxein, T. Woike, and K. Buse, "Generation of small bound polarons in lithium niobate crystals on the subpicosecond time scale," Appl. Phys. B **83**, 527–530 (2006).

[25] V. Lucarini, J. J. Saarinen, K.-E. Peiponen, and E. M. Vartiainen, eds., *Kramers-Kronig Relations in Optical Materials Research* (Springer Verlag, 2005).

[26] H. Kogelnik, "Coupled wave theory for thick hologram gratings," Bell Syst. Tech. J. **48**, 2909 (1969).

[27] D. S. Smith, H. D. Riccius, and R. P. Edwin, "Refractive indices of lithium niobate," Opt. Commun. **17**, 332–335 (1976).

[28] T. Fujiwara, M. Takahasi, M. Ohama, A. J. Ikushima, Y. Furukawa, and K. Kitamura, "Comparison of electro-optic effect between stoichiometric and congruent $LiNbO_3$," Electron. Lett. **35**, 499–501 (1999).

[29] C.-T. Chen, D. M. Kim, and D. von der Linde, "Efficient hologram recording in $LiNbO_3$:Fe using optical pulses," Appl. Phys. Lett. **34**, 321–324 (1979).

[30] D. Maxein, J. Bückers, D. Haertle, and K. Buse, "Photorefraction in $LiNbO_3$:Fe crystals with femtosecond pulses at 532 nm," Appl. Phys. B **95**, 399–405 (2009)

[31] C. Nölleke, J. Imbrock, and C. Denz, "Two-step holographic recording in photorefractive lithium niobate crystals using ultrashort laser pulses," Appl. Phys. B **95**, 391–397 (2009).

[32] M. Simon, F. Jermann, and E. Krätzig, "Photorefractive effects in LiNbO3:Fe, me at high light intensities," Opt. Mat. **4**, 286 – 289 (1995).

[33] O. F. Schirmer and D. von der Linde, "Two-photon and x-ray-induced Nb^{4+} and O^- small polarons in $LiNbO_3$," Appl. Phys. Lett. **33**, 35 (1978).

[34] D. von der Linde, O. F. Schirmer, and H. Kurz, "Intrinsic photorefractive effect of $LiNbO_3$," Appl. Phys. A **15**, 153–156 (1978).

[35] G. A. Brost, R. A. Motes, and J. R. Rotge, "Intensity-dependent absorption and photorefractive effects in barium titanate," J. Opt. Soc. Am. B **5**, 1879–1885 (1988).

[36] H. Vormann and E. Krätzig, "Two step excitation in $LiTaO_3$:Fe for optical data storage," Solid State Communications **49**, 843–847 (1984).

[37] Y. S. Bai and R. Kachru, "Nonvolatile holographic storage with two-step recording in lithium niobate using cw lasers," Phys. Rev. Lett. **78**, 2944–2947 (1997).

[38] S. Sasamoto, J. Hirohashi, and S. Ashihara, "Polaron dynamics in lithium niobate upon femtosecond pulse irradiation: Influence of magnesium doping and stoichiometry control," J. Appl. Phys. **105**, 083102 (2009).

Holographic Spectroscopy: Wavelength-Dependent Analysis of Photosensitive Materials by Means of Holographic Techniques

Kay-Michael Voit* Mirco Imlau*

Published 23 January 2013

Published as **K.-M. Voit and M. Imlau.** ***"Holographic Spectroscopy: Wavelength-Dependent Analysis of Photosensitive Materials by Means of Holographic Techniques."*** in *MDPI Materials 6, no. 1 (January 23, 2013): 334–358. doi:10.3390/ma6010334* under Creative Commons Attribution license.

Holographic spectroscopy is highlighted as a powerful tool for the analysis of photosensitive materials with pronounced alterations of the complex permittivity over a broad range in the visible spectrum, due to the advances made both in the fields of advanced holographic media and highly tunable lasers systems. To analytically discuss consequences for in- and off-Bragg reconstruction, we revised Kogelnik's coupled wave theory strictly on the basis of complex permittivities. We extended it to comply with modern experimental parameters such as out-of-phase mixed holograms and highly modulated gratings. A spatially modulated, wavelength-dependent permittivity that superimposes a spatially homogeneous wavelength-dependent ground state spectrum is taken into account for signal wave reconstruction with bulky elementary mixed gratings as an example. The dispersion characteristics of the respective diffraction efficiency is modelled for color-center-absorption and absorption of strongly localized carriers. As an example for the theoretical possibilities of our newly derived set of equations, we present a quantitative analysis of the Borrmann effect connected to out-of-phase gratings, providing easier and more intuitive methods for the derivation of their grating parameters.

*School of Physics, Osnabrück University, Barbarastr. 7, Osnabrück 49069, Germany

1 Introduction

Holography [1, 2] provides impressive tools for the analysis of photosensitive materials at
optical frequencies: test holograms can be recorded by optical means, and phase-front as well as amplitude-distribution of the reconstructed signal waves are detected.

Applying an appropriate theoretical model for the analysis yields the modulation depth $\Delta\epsilon$ of the material's complex permittivity modulation and, if present, of the phase-shift between refractive index and absorption grating Φ. Thereby, the photo-physical processes underlying the holographic recording of optically induced gratings, *i.e.*, the materials' photosensitivity in general, can be studied. (Such processes can be rather complex, such as the photorefractive effect that combines optical excitation of charge carriers in wide-band gap dielectrics, charge transport phenomena, the build-up of electric space-charge fields due to re-trapping in dark regions of the fringe pattern and the modulation of the refraction index via the Pockels effect.) It is the starting point for a targeted design of hologram recording media. Also, the optimum boundary conditions for hologram recording, taking into account the large variety of upcoming applications of modern holography in photonics [3, 4], such as for instance real-time holographic displays, can be determined.

Prominent examples for the successful application of holography for material analysis are photorefractive crystals, *i.e.*, crystals that obey the photorefractive effect for hologram recording. A second example is molecular holographic media built from transition-metal-compounds. Here, the targeted design of hologram recording materials related to a broad range of parameters including photosensitivity, spectral sensitivity and hologram lifetime has been demonstrated [5, 6].

The correct analysis of phase and amplitude of the reconstructed signal wave from the test hologram is the key point of material characterization by means of holography. Boundary conditions for the derivation of the analysis have to be chosen adequately to experimental conditions and material parameters. Several publications in literature face this type of analysis in detail for isotropic media [7–16] with Kogelnik's *coupled wave theory for thick hologram gratings* [17] being the most recognized one. Anisotropic media were studied thoroughly by Montemezzani and Zgonik [18] and Sturman *et al*. [19] by vectorial theories and consideration of the tensorial properties of the permittivity. This enabled the analysis of such important classes of photosensitive materials as semiconductors and sillenites. In other words, the underlying theoretical problem has been solved decades ago and the derived set of formula is applied to a manifold of hologram recording media and phenomena.

However, some of the chosen boundary conditions do not fully comply with experimental parameters of modern holographic recording setups or the features of advanced hologram recording media. From the experimental point of view, tunable lasers have become state-of-the-art, thus, admitting hologram reconstruction over a broad range in the optical spectrum and the application of the holographic principle for spectroscopy. Advanced hologram recording media, such as garnets, nematic liquid crystal cells, photopolymers or molecular crystals, feature pronounced alterations of the complex di-

electric permittivity. Some of these materials also show an arbitrary phase shift between the modulation of the real and the imaginary part of the permittivity. These conditions have been described by Guibelalde [7], but the derived equations show a high grade of formal complexity that prevents most further analysis [20].

For a broader range of applications, a more manageable set of formula is preferable, that particularly allows for a higher flexibility with respect to the set of boundary conditions. We have revised the derivation of the coupled wave theory accordingly by keeping the permittivity and its optically induced alteration as complex measure throughout the manuscript. We use the scalar permittivity. Thus, the theory presented is applicable to isotropic media and materials and setups in which an effective scalar permittivity may be assumed and the modulated permittivity tensor maintains diagonal form [18].

It turns out that the derived set of formula enables the analytical expression of measures that have not been reported in literature, so far—while classical measures still are involved. As an example, we introduce an analytically simple expression for the intensity ratio of the plus- and minus-first-order diffracted waves (*Borrmann*-effect), which allows easier characterisation of complex mixed grating structures. Moreover, a quantitative analysis for hologram reconstruction taking into account angular detuning and mixed, out-of-phase gratings is presented (*rocking curve*). All measures are presented as wavelength-dependent properties, thus enabling the analysis of the dispersive features of hologram reconstruction in presence of a pronounced spectrum of the ground state absorption. While experimental basics have been described in [21], a complete theoretical analysis of this holographic spectroscopy method is not yet present in literature. The dispersion related features are highlighted with hologram reconstruction at test holograms recorded via dopants and via small bound polarons as an example.

2 Recording a Test Hologram and the Properties of Its Permittivity

2.1 Recording of a Test Hologram

The superposition of two identical, mutually tilted coherent plane (or spherical) waves is a simple way to record test holograms. The respective fringe pattern is a one-dimensional (or radially symmetrical) intensity modulation aligned parallel to the samples' entrance surface. Maxima and minima refer to constructive and destructive interference. From the point of view of the holographic principle, the two indistinguishable waves can be assigned unambiguously to reference (R-) and signal (S-) waves by choosing one of the beams for signal wave reconstruction. The signal is regarded as a point source positioned at infinite distance from the hologram recording medium.

The corresponding optical setup for the case of plane phase fronts is depicted in Figure 1. Monochromatic laser light of a coherent, tunable laser source with flat-top intensity profile and planar wave-front is split into two identical beams (In case that a Gaussian intensity profile is present at the laser source output, an optical system

for the transfer of Gaussian to flat-top-intensity profile [22] can be included in the setup). The symmetric configuration of the beam paths secures equal optical path lengths for R- and S-waves measured between the beamsplitter BS2 and the hologram recording medium (sample). At least, a path length match within the coherence length of the laser is required. Together with an adjustment of the beam intensities such that $I_{\mathrm{R}} = |R_0|^2 = I_{\mathrm{S}} = |S_0|^2$ as well as a precise parallel adjustment of the electric field vectors $\mathbf{e}_{\mathrm{R}} \parallel \mathbf{e}_{\mathrm{S}}$ via the polarizers P, a fringe pattern with maximum modulation depth $m = 2\mathbf{e}_{\mathrm{R}}\mathbf{e}_{\mathrm{S}}|R_0 S_0|/(|R_0|^2 + S_0|^2) = 1$ is obtained. Here, R_0, S_0 denote the electric field amplitudes of the R- and S-waves outside the medium. Recording of the hologram can be controlled via the shutter SH1.

We note that the homogeneity of the intensity profiles of the recording beams is optimized via the spatial frequency filter SFF (lenses L1 and L2, and pinhole PH) that represents a low-pass optical filter by positioning a pinhole ($\ll 100\,\mu$m) precisely within the Fourier plane of lens L1 (For the case of intense ns-pulses, the pinhole needs to be placed within an evacuated chamber in order to suppress plasma formation.) The precise adjustment of lens L2 is mandatory to keep the planar wavefront (This can be controlled simply by optical inspection of an interference pattern generated by a plane parallel plate inserted into the beam path and slightly tilted with respect to the beam direction. Alternatively, a Shack Hartmann wavefront sensor may be used).

The spatial intensity modulation that results from the interference between the R- and S-waves is aligned within the plane of incidence and orthogonal to the samples' normal, *i.e.*, along x-direction according to the inset of Figure 1. It represents a one-dimensional sinusoidal intensity distribution best described by $I(x) = |R_0 + S_0|^2 = (|R_0|^2 + |S_0|^2)[1 + m\cos(Kx + \Phi_0)]$ with the modulation depth $0 \leq m \leq 1$, the spatial frequency of the grating $K = |\mathbf{K}| = 2\pi/\Lambda$, and the wavelength related to the intensity modulation Λ ($\mathbf{K} = \mathbf{k}_{\mathrm{R}} - \mathbf{k}_{\mathrm{S}}$, see inset of Figure 1). Here, $\mathbf{k}_{\mathrm{R}}$ and $\mathbf{k}_{\mathrm{S}}$ denote the wavevectors of the R- and S-wave with $|\mathbf{k}_{\mathrm{R}}| = |\mathbf{k}_{\mathrm{S}}| = 2\pi/\lambda$. The wavelength $\Lambda = \lambda/2\sin(\theta)$ is determined by the recording wavelengths and the angle of incidence $\theta = \theta_{\mathrm{R}} = \theta_{\mathrm{S}}$ that is measured with respect to the samples' normal. The phase position Φ_0 takes into account the relative phase adjustment of the R- and S-waves. Here, it is independent on time ($\Phi_o(t) = \Phi_0$) because of $\lambda = \lambda_{\mathrm{R}} = \lambda_{\mathrm{S}}$.

The characteristics of this optical setup comply with the simplifications of the theoretical analysis shown in Table 1.

2.2 Properties of the Permittivity of the Test Hologram

The analysis of the interaction of a coherent light wave with the test hologram starts with the Maxwell equations, particularly, by deducing the Helmholtz equation

$$\Delta E(\mathbf{r}) + k_0^2 \hat{\epsilon}(\mathbf{r}, \lambda)\mu E(\mathbf{r}) = 0 \tag{1}$$

where $E(\mathbf{r})$ is the electric field component perpendicular to the gradient of $\epsilon(\mathbf{r}, \lambda)$, (The given equation holds true for most experimental setups, where $\epsilon(\mathbf{r}, \lambda)$ is modulated parallel to the surface of the optical table and $\mathbf{E}$ is perpendicular to the table. In any

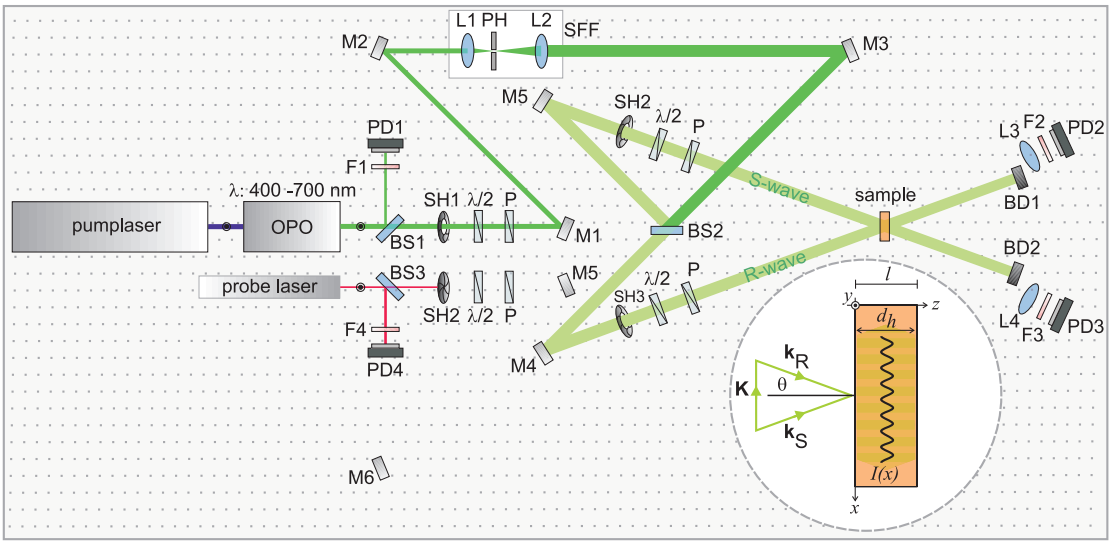

Figure 1: Sketch of an optical setup for the recording of a test hologram: reference (R) and signal (S) waves that are mutually coherent and feature a flat-top intensity distribution and planar wavefronts, superimpose in a photosensitive medium of thickness l and generate a sinusoidal intensity distribution. M1–M6: mirrors; L1–L4: lenses; BS1–BS3: beam splitters, F1–F4: filters, P: polarizers; $\lambda/2$: half-wave retarder plates; SH1–SH3: computer-controlled beam shutters; PD1-PD4: Si-PIN diodes; BD1,BD2: beam dumps; SFF: spatial frequency filter, PH: pin-hole. The direction of the corresponding wavevectors of the recording beams ($\mathbf{k}_\mathrm{R}$, $\mathbf{k}_\mathrm{S}$) and the intensity distribution with respect to cartesian coordinates $I(x)$ is depicted in the inset.

other case, additional terms may have to be considered in the wave equation due to the anisotropic medium.) k_0 is the wavenumber in vacuum and $\epsilon(\mathbf{r}, \lambda)$ is the spatially dependent absolute permittivity. The relative magnetic permeability μ_r is assumed to be unity. Common experimental media, however, are described in terms of the (real) refractive index and the absorption. All these quantities may strongly depend on the wavelength of the interacting electromagnetic wave and thus may be examined using spectroscopic methods.

In contrast to former derivations, we assumed the refractive index and the absorption index to be the fundamentally modulated quantities. This is justified by the fact that the relative complex permittivity $\epsilon(\lambda)$ is the natural quantity of Equation (1).

Let us first have a look at the connection to the refractive index n and the absorption index κ with regard to a sinusoidally modulated mixed grating with a common grating vector $\mathbf{K}$, but potentially different phase shifts Φ_n and Φ_κ (out-of-phase gratings) (The phase shifts are given in relation to the origin that is defined by the interference pattern

Table 1: Characteristics of the optical setup and their relation to simplifications made in the theoretical analysis.

Characteristic of the optical setup	**Simplification for the theoretical analysis**
hologram recording is performed with equal wavelengths of R- and S-waves *degenerate wave-mixing*)	$\lambda_\mathrm{R} = \lambda_\mathrm{S}$, *i.e.*, $\lvert\mathbf{k}_\mathrm{R}\rvert = \lvert\mathbf{k}_\mathrm{S}\rvert = 2\pi/\lambda$
hologram recording is performed by the superposition of planar wave fronts	sinusoidal permittivity modulation *
R- and S-waves feature flat-top intensity profile	the electric field amplitudes are constant within the beam paths and the beam is assumed to have infinite diameter
hologram recording is performed with equal directions of the electric field vectors of R- and S-wave and with equal intensities	$\lvert R_0\rvert^2 = \lvert S_0\rvert^2$, *i.e.*, the modulation depth becomes unity ($m = 1$), $\mathbf{e}_R \cdot \mathbf{e}_S = 1$
hologram recording is homogeneously over the entire volume, *i.e.*, exponential decrease of the grating parameters in z-direction is excluded (cf. [9]) **	permittivity modulation is not z-dependent
wave vector of the hologram is directed perpendicularly to the samples' normal	permittivity modulation is aligned parallel to x-axis (*unslanted* hologram)

* Under the given conditions, a sinusoidal modulation is realized if hologram recording responses linear to the intensity of the recording beam superposition of planar wave fronts. However, at large modulation depth, the recording of holographic gratings is typically nonlinear [23, 24]. In these cases, the permittivity modulation will not be sinusoidal, but a sine of the corresponding periodicity will usually be the dominating Fourier component. In the following sections, we will argue that within limits, the derived theory is still applicable then; ** Simply assuming a smaller effective grating depth than the crystal has shown the same effects in praxis.

of two incident beams without phase shifts):

$$n(\mathbf{r},\lambda) = n_0(\lambda) + n_1(\lambda)\cos(\mathbf{K}\cdot\mathbf{r} + \Phi_n) \tag{2}$$

$$\kappa(\mathbf{r},\lambda) = \kappa_0(\lambda) + \kappa_1(\lambda)\cos(\mathbf{K}\cdot\mathbf{r} + \Phi_\kappa) \tag{3}$$

where $\mathbf{K} = (K_x, 0, 0)^t$ is the grating vector of a non-slanted grating. As $\mathbf{n}(\mathbf{r},\lambda) = n(\mathbf{r},\lambda)(1 + i\kappa(\mathbf{r},\lambda))$ is the complex refractive index and $\epsilon(\mathbf{r},\lambda) = \mathbf{n}(\mathbf{r},\lambda)^2$ (assuming the permeability $\mu_r = 1$ and frequencies in the optical range), this results in

$$\begin{aligned}\epsilon(\mathbf{r},\lambda) = {} & n_0(\lambda)^2 + 2n_0(\lambda)n_1(\lambda)\cos(\mathbf{K}\cdot\mathbf{r} + \Phi_n) \\ & - 2n_0(\lambda)^2\kappa_0(\lambda)\kappa_1(\lambda)\cos(\mathbf{K}\cdot\mathbf{r} + \Phi_\kappa) \\ & + i[2n_0(\lambda)^2\kappa_0(\lambda) + 2n_0(\lambda)^2\kappa_1(\lambda)\cos(\mathbf{K}\cdot\mathbf{r} + \Phi_\kappa) \\ & + 4n_0(\lambda)n_1(\lambda)\kappa_0(\lambda)\cos(\mathbf{K}\cdot\mathbf{r} + \Phi_n)]\end{aligned} \tag{4}$$

We have omitted several terms in Equation (4) for two reasons: 1. The first class are terms that are nonlinear in κ_0. These terms are left out as $\kappa_0 \ll 1$. (In the optical range, if $\kappa_0 \approx 1$, $\alpha_0 \approx 10^8\,\mathrm{m}^{-1}$, according to $\alpha = 2k_0 n_0 \kappa_0$. Compared with common experimental values in the order of magnitude of 10^2, this can be considered extremely high, thus justifying the assumption of $\kappa_0 \ll 1$.) We like to note, however, that they can be incorporated into further calculation at the cost of slightly higher complexity but without generating new problems, as they are still proportional to $\cos(\mathbf{K}\cdot\mathbf{r} + \Phi_\kappa)$ or $\cos(\mathbf{K}\cdot\mathbf{r} + \Phi_n)$. 2. The second class consists of terms nonlinear in κ_1, n_1 and thus in a mixture of these cosine terms. Here, we can argue again that κ_1, $n_1 \ll 1$, *i.e.*, the light induced alterations are small, but a more convenient argument will be presented in the later discussion in Section 3.2.

The first cosine term in Equation (4) of the real part is the refractive index grating depending on n_1 and the first one in the imaginary part is the absorption grating depending on κ_1. Additionally, there is a real term which acts like a refractive-index grating though it is governed by κ_1, and carries the phase shift of the absorption grating. Furthermore, there is an imaginary one which correspondingly acts like an absorption grating but is proportional to n_1 and carries the phase shift of the refractive index grating. However, these terms are much smaller in most usual cases and may be neglected.

As the sum of two trigonometric functions of one frequency is another trigonometric function with the same frequency, ϵ can be written as

$$\begin{aligned}\epsilon(\mathbf{r},\lambda) = {} & \epsilon_0'(\lambda) + \epsilon_1'(\lambda)\cos(\mathbf{K}\cdot\mathbf{r} + \Phi_B) \\ & + i\left(\epsilon_0''(\lambda) + \epsilon_1''(\lambda)\cos(\mathbf{K}\cdot\mathbf{r} + \Phi_A)\right)\end{aligned} \tag{5}$$

where

$$\epsilon_0'(\lambda) = n_0(\lambda)^2 \tag{6}$$
$$\epsilon_0''(\lambda) = 2n_0(\lambda)^2\kappa_0(\lambda) \tag{7}$$
$$\epsilon_1'(\lambda) = \sqrt{R_B(\lambda)^2 + I_B(\lambda)^2} \tag{8}$$
$$\epsilon_1''(\lambda) = \sqrt{R_A(\lambda)^2 + I_A(\lambda)^2} \tag{9}$$
$$\Phi_A(\lambda) = \pm\arccos\left(R_A(\lambda)/\epsilon_1''(\lambda)\right) \quad \text{(positive if } R_A(\lambda) < 0\text{)} \tag{10}$$
$$\Phi_B(\lambda) = \pm\arccos\left(R_B(\lambda)/\epsilon_1'(\lambda)\right) \quad \text{(positive if } R_B(\lambda) < 0\text{)} \tag{11}$$
$$R_A(\lambda) = 2n_0(\lambda)^2\kappa_1(\lambda)\cos(\Phi_\kappa) + 4n_0(\lambda)n_1(\lambda)\kappa_0(\lambda)\cos(\Phi_n) \tag{12}$$
$$I_A(\lambda) = 2n_0(\lambda)^2\kappa_1(\lambda)\sin(\Phi_\kappa) + 4n_0(\lambda)n_1(\lambda)\kappa_0(\lambda)\sin(\Phi_n) \tag{13}$$
$$R_B(\lambda) = -2n_0(\lambda)^2\kappa_0(\lambda)\kappa_1(\lambda)\cos(\Phi_\kappa) + 2n_0(\lambda)n_1(\lambda)\kappa_0(\lambda)\cos(\Phi_n) \tag{14}$$
$$I_B(\lambda) = -2n_0(\lambda)^2\kappa_0(\lambda)\kappa_1(\lambda)\sin(\Phi_\kappa) + 2n_0(\lambda)n_1(\lambda)\kappa_0(\lambda)\sin(\Phi_n) \tag{15}$$

are the cumulated real and imaginary modulations of the permittivity and their phase shifts. Thus, a sinusoidal grating in n and κ is also a sinusoidal grating in ϵ in good approximation. In contrast to [17] and [7], however, we will proceed in our calculation using the permittivity.

3 Dispersion of First Order Diffracted Waves

3.1 Signal Wave Reconstruction

Upon the recording of the test hologram, the complex permittivity ϵ of the sample will be modulated along the x-direction. Assuming a linear recording mechanism, a sinusoidal modulation proportional to $I(x)$ can be expected. Hence, this permittivity grating is also characterized by the wave vector $\mathbf{K}$. Reconstruction of the signal wave S can be performed by exposure of $\mathbf{K}$ with a monochromatic wave (wavevector $\mathbf{k}$, $|\mathbf{k}| = 2\pi/\lambda$ and angle of incidence θ measured with respect to the hologram's normal). Wavelength and angle of incidence can be chosen in a rather broad range provided that the complex permittivity allows for wave propagation in the medium and the permittivity modulation extends into the desired reconstruction wavelength range. The wavelength and the propagation direction, *i.e.*, the wavevector of the reconstructed wave are unambiguously determined by momentum conservation, resulting in the wavevector $\mathbf{k}_S = \mathbf{k}_R - \mathbf{K}$ (cf. Figure 2). We note here that for an arbitrarily chosen reconstruction wave $\mathbf{k}_R$ in the majority of cases $|\mathbf{k}_R| \neq |\mathbf{k}_S|$ and the angle of the reference wave to the hologram's normal will differ from the angle of the signal wave.

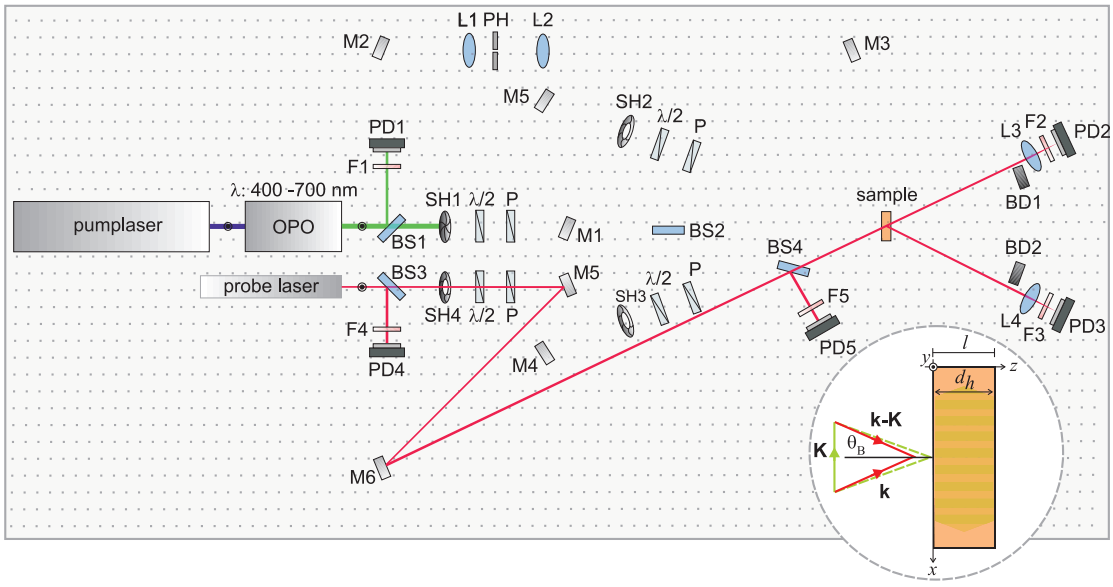

Figure 2: Sketch of an optical setup for the reconstruction of a test hologram: Closing of shutter SH1 stops the hologram recording process. Then, reconstruction with a wavelength different from the recording wavelength is enabled by opening shutter SH4. The direction of the probe beam, particularly the angle of incidence with respect to the samples' normal, is adjusted according to momentum conservation depicted in the inset figure.

However, the appearance of wavelengths in the reconstructed beam spectrum different from the wavelength of the reconstructing wave is impossible, *i.e.*, ($|\mathbf{k_S}| = |\mathbf{k_R}|$),

if frequency conversion or inelastic scattering phenomena (e.g., Raman scattering) are not to be considered in the holographic medium under study. In this particular case, conservation of energy enforces a specific angle of incidence for a given wavelength of the reconstruction wave, commonly denoted as the *Bragg* angle θ_{B} and determined by $\theta_{\mathrm{B}} = \arcsin(\lambda/2\Lambda)$. We note that the Bragg angle and the angle of recording coincide ($\theta_{\mathrm{B}} = \theta$) solely for identical wavelengths of recording and reconstruction beams.

Conservation of energy and momentum defines a sharp constraint for the possibility of wave reconstruction for a given grating vector **K**. However, in any practical situation, this condition is softened by at least two effects, leading to the well known rocking curve (*i.e.*, the shape of the signal wave's intensity profile upon angular or wavelength detuning from the Bragg condition): 1. Every existing laser system has a certain wavelength bandwidth. Consequently, there is not only one writing wavelength λ but a range $[\lambda - \delta\lambda, \lambda + \delta\lambda]$, which is resembled either by the range of possible reconstruction wavelengths under a certain angle of incidence or the range of angles for a given wavelength; 2. The sharpness of a grating is inversely proportional to the dimensions of the grating (cf. Figure 24.5a,b in [25]). In z-direction, the uncertainty of the Bragg condition of a grating with thickness d is given by $2\pi/d$. Consequently, the Bragg condition is a property of thick holograms. In x-direction, the dependency on the dimensions is even more obvious, as for an extension of the illumination that is smaller than Λ, the modulation would lose its grating characteristics. As commonly used beam diameters typically illuminate several hundreds or thousands of grating periods, finiteness in x-direction can be neglected. The finiteness of the grating in z-direction, however, which is governed either by the thickness of the crystal or the effective penetration depth of the recording beam, is covered. The z-dependency will be considerable for common samples and may be used to determine the effective grating thickness d_{eff}.

The spectral width of the recording beam is assumed to be sharp compared with other effects in the theory, but related effects can be addressed via the spectroscopic methods presented in the following.

From the experimental point of view, this implies that reconstruction of the signal beam S can be simply performed by exposure of the recorded grating to the reference beam, *i.e.*, by shutting the signal beam via shutter SH3. Then, the Bragg condition is automatically fulfilled. Alternatively, probing wavelengths different from the recording wavelength can be used provided the fulfilment of the Bragg condition via angular adjustment (The experimental values (wavelengths, angle of incidence) are determined outside the hologram media. In contrast, the theoretical derivation of the underlying wave coupling process proceeds for measures inside the sample. Hence, wavelengths and propagation angle of recording and probe beams in the experiment must be corrected for refraction.)

The basic setup for signal beam reconstruction exemplarily for a particular probing wavelength λ slightly larger than the recording wavelength is sketched in Figure 2.

Compared with Figure 1, shutters SH1 and SH4 have been closed and opened, respectively. Bragg-matched read-out is verified by choosing an appropriate angle of incidence. Furthermore, the hologram lifetime τ_{h} is much larger than the time required for reconstruction. The reconstructed signal beam is detected by its intensity using

photodiode PD3, *i.e.*, the presence of a hologram is verified by an intensity $|S|^2 > 0$. Its quality is defined via the diffraction efficiency $\eta_1 = |S|^2/|R_0|^2$, that is determined predominantly by the amplitude of change of the complex permittivity as shown in the following theoretical analysis.

With this setup in mind and the properties of the Bragg condition mentioned above, we are able to study the dispersive properties of the recorded grating by applying a tunable probe laser. Technically, the angular adjustment for each probing wavelength can be performed by different means. We here mention the application of a motorized linear or rotation stage for automatic adjustment of the reconstruction beam. But also the rotation of the hologram medium itself can be considered in the case of a sufficient hologram lifetime. White light generation using an ultrafast laser system has become very attractive for generation of a broad-band light intensity spectrum. Its divergence angle can be adjusted properly to match with the angular range of the Bragg condition.

The determination of grating parameters over a broad spectral range then can be used for an exhausting analysis of the photophysical effects that are underlying the hologram recording (*holographic spectroscopy*). It should be noted, that tuning the recording wavelength is also possible, as indicated by the tunable laser source applied for hologram recording in Figure 1. In this case, the dispersive properties of the photosensitive response are retrieved.

3.2 Coupled-Wave Theory

Reconstruction can be understood as light diffraction at a thick, periodic permittivity grating. We will construct a first order coupled-wave theory modulation according to the simplified sketch in the inset of Figure 1.

Introducing Equation (5) into Equation (1) results in a linear partial differential equation (PDE) with complex, periodic coefficients. The problem including the boundary conditions is isotropic in y direction and $\mathbf{K}$-periodic in x direction, but still strongly depends on the z direction. Consequently, an ansatz for the solution of an incoming beam with wave vector $\mathbf{k} = k_0 \left(\epsilon_0'(\lambda)\right)^{1/2} (\sin(\theta), 0, \cos(\theta))^t$ is provided by the Fourier series $E(\mathbf{r}) = \sum_{n=-\infty}^{\infty} A_n(z) \exp\left(i(\mathbf{k} - n\mathbf{K}) \cdot \mathbf{r}\right)$. The terms in the sum may be interpreted as diffracted beams with wave vector $\mathbf{k} - n\mathbf{K}$ and complex amplitude $A_n(z)$. We will refer to them as the n-th diffraction orders.

By equating coefficients of the exponential functions, an infinite set of ordinary second order differential equations can be derived. The influence of the second order has been discussed in [26]. Due to the fact that it is small even in heavily modulated thick gratings, we will neglect it in the following.

The resulting ordinary differential equations (ODEs) have the form

$$A_n'(z) = aA_{n-1}(z) + b_n A_n(z) + cA_{n+1}(z) \tag{16}$$

where a, b, c are complex numbers. This coupling between the Fourier coefficients, *i.e.*, the outgoing waves, emerges from the terms $\exp(i\mathbf{K} \cdot \mathbf{r})$ and $\exp(-i\mathbf{K} \cdot \mathbf{r})$ of the exponential representation of ϵ being multiplied with E and thus resulting in a term

$A_n(z)\exp((\mathbf{k}-(n\pm 1)\mathbf{K})\cdot\mathbf{r})$. Consequently, every equation of the complete infinite set is iteratively coupled to any other via the equations between.

In a diffraction experiment, only $A_0(0)\neq 0$ in the boundary conditions and, due to the iterative coupling, $A_n(z)\neq 0$, if and only if one of its neighbouring coefficients $A_m(z)\neq 0$ for $m=n\pm 1$. Thus, the beam intensity can only build up "from the inside to the outside", *i.e.*, from lower to higher absolute diffraction orders.

The system (16) of coupled differential equations can be written in vector form as

$$\mathbf{A}'(z)=\hat{\mathbf{B}}\mathbf{A} \tag{17}$$

where $\hat{\mathbf{B}}$ is an infinite tridiagonal matrix. Equation (17) will have the formal solution $\mathbf{A}(z)=\exp\left(\hat{\mathbf{B}}z\right)\mathbf{A}(0)$. In order to evaluate it one needs the eigenvalues and eigenvectors of $\hat{\mathbf{B}}$. They could be determined numerically, or, because the entries of the secondary diagonals of B are typically three orders of magnitude smaller than its diagonal elements, by means of the perturbation theory. Then we are faced with the following problem: In the in-Bragg case ($\theta=\theta_B$) two diagonal elements of $\hat{\mathbf{B}}$ coincide, namely $b_1=b_0$, and one has to invoke the twofold degenerate perturbation theory. However, in the far-off-Bragg case (e.g., $\theta\gg\theta_B$) the non-degenerate perturbation theory has to be applied. Both theories give different results and the need for a unified approximation that can be applied in the whole domain arises. It turns out that the two-coupled wave approximation (Kogelnik ansatz) can be viewed as an interpolation between the results of perturbation theory in the two extremal cases in-Bragg and far-off-Bragg, as far as the two waves $A_0(z)$ and $A_1(z)$ are concerned. The details of this argument will be published elsewhere. Here we take these remarks only as an additional justification to follow the Kogelnik ansatz for the diffraction problem.

Instead, this purely mathematical approach may be greatly simplified by taking into account the physical nature of the problem. As explained above, due to momentum and energy conservation the Bragg condition, allows for only up to one signal beam. The previous considerations demand this beam to be described by $A_{\pm 1}(z)$: Depending on the sign of the angle of incidence and the choice of the direction of K, $A_{\pm 1}(z)\exp(i(\mathbf{k}-\mathbf{K})\cdot\mathbf{r})$ is thus the only possible wave satisfying the Bragg condition for the incident beam $A_0(z)\exp(i(\mathbf{k})\cdot\mathbf{r})$. All other parts of the solution are assumed to be damped exponentially and do thus not develop notably. It has been shown [27, 28] that these higher diffractions do not play a role even for high diffraction efficiencies for incidence angles below 45°. The damping effect even for minor deviations of the remaining reference beam from the Bragg angle will be shown in the off-Bragg case, which will be discussed later.

Furthermore, this constitutes our additional argument to omit the second class of nonlinear terms in Section 2, as any contribution proportional to $\cos(n\mathbf{K}\cdot\mathbf{r}+\phi)$, $|n|>1$, would couple only into the higher orders of the Fourier series shown above and thus induce a beam violating the Bragg condition. (They would, however define an additional Bragg angle, but are neglected due to the considerable lower diffraction efficiency. This fact is especially important for periodic gratings that deviate from the sinusoidal form, such as gratings that are excited up to the saturation region [29]. At least for smaller

deviations, the present theory may still be applied, only using the first order of their Fourier series, as any other order couples in beams violating the Bragg condition.)

These considerations result in a two-wave ansatz

$$E(\mathbf{r}) = R(z)\exp\left(i\mathbf{k}\cdot\mathbf{r}\right) + S(z)\exp\left(i(\mathbf{k}\pm\mathbf{K})\cdot\mathbf{r}\right) \tag{18}$$

where $R(z) = A_0(z)$ is the incident reference beam, $S(z) = A_1(z)$ is the diffracted signal beam and again, the sign depends on the angle of incidence and the choice of the direction of K. Compared with the ansatz by Kogelnik, which uses the negative sign, this version allows to take into account the effects of non-phase-symmetrical gratings, *i.e.*, gratings with $\Phi \neq 0$ or $\Phi \neq \pi$, which are not invariant against a reflection about the z-axis. We will, however, proceed with the negative sign, which is valid for a grating vector and beam incidence in (partially) positive x direction ($\theta > 0$), and integrate the incidence for $\theta < 0$ via the symmetry argument $\theta \to -\theta \Rightarrow \Phi \to -\Phi$.

We note that a solution taking into account higher orders of diffraction (Rigorous Coupled-Wave Theory) has been presented in [8, 30–32]. A comparison with Kogelnik's theory has recently been given in [33]. These orders are especially important for thin gratings, where the damping effect of the violation of the Bragg conditions is less relevant. The off-Bragg directional performance of this choice for a **k**-vector, the beta-value method (BVM) published in [9] has been studied experimentally in comparison with the Kogelnik ansatz in [34].

Inserting Equation (18) into Equation (1) and substituting $\alpha_0 = 2k_0\left(\epsilon_0'(\lambda)\right)^{1/2}\kappa_0$ gives the following two coupled-wave equations:

$$\begin{aligned}\frac{\mathrm{d}R(z)}{\mathrm{d}z} = &-\frac{\alpha_0}{2\cos(\theta)}R(z)\\ &-\frac{e^{i\Phi_A}k_0\epsilon_1''(\lambda)S(z)}{4\left(\epsilon_0'(\lambda)\right)^{1/2}\cos(\theta)} + \frac{ie^{i\Phi_B}k_0\epsilon_1'(\lambda)S(z)}{4\left(\epsilon_0'(\lambda)\right)^{1/2}\cos(\theta)}\end{aligned} \tag{19}$$

$$\begin{aligned}\frac{\mathrm{d}S(z)}{\mathrm{d}z} = &-\frac{\alpha_0}{2\cos(\theta)}S(z)\\ &-\frac{e^{-i\Phi_A}k_0\epsilon_1''(\lambda)R(z)}{4\left(\epsilon_0'(\lambda)\right)^{1/2}\cos(\theta)} + \frac{ie^{-i\Phi_B}k_0\epsilon_1'(\lambda)R(z)}{4\left(\epsilon_0'(\lambda)\right)^{1/2}\cos(\theta)}\\ &+ i\left(\frac{K_x^2}{2k_0\left(\epsilon_0'(\lambda)\right)^{1/2}\cos(\theta)} - K_x\tan(\theta)\right)S(z)\end{aligned} \tag{20}$$

As explained in the initial table, the illumination is assumed to be constant in y-direction and infinitely large. Thus the equation does not depend on y.

In the limit case of a zero grating modulation $\epsilon_1' = \epsilon_1'' = 0$, the first term of each equation, *i.e.*, the diagonal of the differential equation system, remains and gives the well known Beer–Lambert law for the base absorption in the material. With non-zero grating modulation, a Beer–Lambert-like exponential decay is maintained, but it is governed by the mean absorption of the grating. It then contributes to the different

decay characteristics of the transmitted and diffracted beams. The diagonal can be eliminated in the following by introducing the law into the ansatz using the substitution $R(z) = \bar{R}(z)\exp(-\alpha_0 z/(2\cos(\theta))$ and $S(z) = \bar{S}(z)\exp(-\alpha_0 z/(2\cos(\theta))$, resulting in the equations

$$\frac{\mathrm{d}\bar{R}(z)}{\mathrm{d}z} = \frac{e^{i\Phi_A} k_0 \epsilon_1''(\lambda)\bar{S}(z)}{4\left(\epsilon_0'(\lambda)\right)^{1/2}\cos(\theta)} - \frac{ie^{i\Phi_B} k_0 \epsilon_1'(\lambda)\bar{S}(z)}{4\left(\epsilon_0'(\lambda)\right)^{1/2}\cos(\theta)} \tag{21}$$

$$\begin{aligned}\frac{\mathrm{d}\bar{S}(z)}{\mathrm{d}z} = &\frac{e^{-i\Phi_A} k_0 \epsilon_1''(\lambda)\bar{R}(z)}{4\left(\epsilon_0'(\lambda)\right)^{1/2}\cos(\theta)} - \frac{ie^{-i\Phi_B} k_0 \epsilon_1'(\lambda)\bar{R}(z)}{4\left(\epsilon_0'(\lambda)\right)^{1/2}\cos(\theta)} \\ &+ i\left(\frac{K_x^2}{2k_0\left(\epsilon_0'(\lambda)\right)^{1/2}\cos(\theta)} - K_x\tan(\theta)\right)\bar{S}(z)\end{aligned} \tag{22}$$

Here and in the following, the barred variables represent quantities adjusted by the mean absorption.

In this form, Equation (21) is reduced solely to the coupling, as the two terms are governed by the amplitude of the other beam, $S(z)$. Equation (22) shows similar coupling terms, but also feature an additional term in the last line of Equation (22), becoming zero in the case that $\theta = \theta_B = \arcsin(K_x/(2k_0\left(\epsilon_0'(\lambda)\right)^{1/2}))$, *i.e.*, if the Bragg condition is fulfilled. Introducing this formula into the last line, *i.e.*, expressing K_x through θ_B, results in a coefficient

$$\left(k_0\epsilon_0'(\lambda)\right)^{1/2}\left(\frac{2\sin\left(\theta_B\right)^2}{\cos(\theta)} - 2\sin(\theta_B)\tan(\theta)\right) \tag{23}$$

From this, we define the off-Bragg parameter as

$$\beta(\theta) = \frac{2\sin\left(\theta_B\right)^2}{\cos(\theta)} - 2\sin(\theta_B)\tan(\theta) \tag{24}$$

The Taylor series given in the second line of Equation (24) is fairly accurate over the range of most rocking curves even for large Bragg angles. Thus, for calculations in the vicinity of the Bragg angle, the approximation

$$\beta(\theta) \approx 2(\theta_B - \theta)\sin(\theta_B) \tag{25}$$

may be used.

3.3 Diffraction Efficiency of Out-of-Phase Mixed Gratings

For an analytical examination, we express Equations (21) and (22) in vector form. The coefficient matrix of the resulting ODE is

$$\hat{A} = \begin{pmatrix} i\beta(\theta)k_0\left(\epsilon_0'(\lambda)\right)^{1/2} & \kappa_- \\ \kappa_+ & 0 \end{pmatrix} \tag{26}$$

with

$$\kappa_{\pm} = -\frac{k_0 \left(\exp(i \pm \Phi_A)\epsilon_1''(\lambda) - i \exp(i \pm \Phi_B)\epsilon_1'(\lambda)\right)}{4 \left(\epsilon_0'(\lambda)\right)^{1/2} \cos(\theta)} \tag{27}$$

This form of the coupling coefficients exhibits a much higher degree of symmetry than the ones used in other publications. One reason for this is the use of one complex quantity, *i.e.*, the permittivity, instead of the two real quantities refractive index and absorption. Indeed, this allows for a considerably better algebraic simplification of the results obtained from the differential equations. Therefore, we will not need to use the abbreviations $\kappa_{\pm}$ in the following.

In a diffraction experiment, there is no natural choice for $x = 0$, as there is no initial interference pattern. Consequently, one of the phase offsets of the gratings can be chosen as 0 without loss of generality. Thus, only the difference between Φ_A and Φ_B matters and the phase difference $\phi_{\text{Diff}}(z)$ between the reference and the signal wave establishes itself accordingly. In the following, we choose $\Phi_B = 0$ and $\Phi_A = \Phi$.

The general solution of the problem is given by

$$\begin{pmatrix} \bar{R} \\ \bar{S} \end{pmatrix} = C_1 \mathbf{A}_1 e^{a_1 z} + C_2 \mathbf{A}_2 e^{a_2 z} \tag{28}$$

where $\mathbf{A}_{1,2}$ are the eigenvectors of $\hat{A}$ and $a_{1,2}$ are their related eigenvalues. The coefficients $C_{1,2}$ emerge from the boundary conditions, which in the most general case with a normalized reference intensity are $\bar{R}(0) = 1$, $\bar{S}(0) = S(0)/|R(0)|$, whereby $S(0) = 0$ in a diffraction experiment. Both the eigensystem and the equation emerging from the boundary conditions can be solved via standard algebraic methods without approximations. Using the boundary condition $S(0) = 0$, the differential equation solved to

$$\begin{aligned}\bar{R}(z,\theta) = {} & e^{\frac{1}{2} i \beta(|\theta|) \left(\epsilon_0'(\lambda)\right)^{1/2} z k_0} \\ & \left(\cos\left(\frac{z k_0 \sqrt{\left(2\beta(|\theta|)\cos(\theta)\epsilon_0'(\lambda)\right)^2 - \epsilon_1''(\lambda)^2 + 2i\cos(\Phi)\,\epsilon_1''(\lambda)\epsilon_1'(\lambda) + \epsilon_1'(\lambda)^2}}{4\left(\epsilon_0'(\lambda)\right)^{1/2}\cos(\theta)} \right) \right. \\ & \left. - \frac{i(2\beta(|\theta|)\cos(\theta)\epsilon_0'(\lambda)) \sin\left(\frac{z k_0 \sqrt{\left(2\beta(|\theta|)\cos(\theta)\epsilon_0'(\lambda)\right)^2 - \epsilon_1''(\lambda)^2 + 2i\cos(\Phi)\epsilon_1''(\lambda)\epsilon_1'(\lambda) + \epsilon_1'(\lambda)^2}}{4\left(\epsilon_0'(\lambda)\right)^{1/2}\cos(\theta)} \right)}{\sqrt{\left(2\beta(|\theta|)\cos(\theta)\epsilon_0'(\lambda)\right)^2 - \epsilon_1''(\lambda)^2 + 2i\cos(\Phi)\,\epsilon_1''(\lambda)\epsilon_1'(\lambda) + \epsilon_1'(\lambda)^2}} \right)\end{aligned} \tag{29}$$

and

$$\begin{aligned}\bar{S}(z,\theta) = {} & i e^{\frac{1}{2} i \beta(|\theta|) \left(\epsilon_0'(\lambda)\right)^{1/2} z k_0} \left(\epsilon_1'(\lambda) + i e^{-i \operatorname{sgn}(\theta) \Phi} \epsilon_1''(\lambda)\right) \\ & \frac{\sin\left(\frac{\sqrt{\left(2\beta(|\theta|)\cos(\theta)\epsilon_0'(\lambda)\right)^2 - \epsilon_1''(\lambda)^2 + 2i\cos(\Phi)\epsilon_1''(\lambda)\epsilon_1'(\lambda) + \epsilon_1'(\lambda)^2}\, k_0 z}{4\left(\epsilon_0'(\lambda)\right)^{1/2}\cos(\theta)} \right)}{\sqrt{\left(2\beta(|\theta|)\cos(\theta)\epsilon_0'(\lambda)\right)^2 - \epsilon_1''(\lambda)^2 + 2i\cos(\Phi)\,\epsilon_1''(\lambda)\epsilon_1'(\lambda) + \epsilon_1'(\lambda)^2}}\end{aligned} \tag{30}$$

Here, we have already introduced the symmetry argument, manifesting in the form the absolute value of θ and the sign function in front of Φ.

The diffraction efficiency, still assuming $\bar{S}(0) = 0$, is given by

$$\eta_1 = \frac{I_S(z)}{I_R(0)} = A_{LB}(\theta) \left| \frac{\bar{S}(z)}{\bar{R}(0)} \right|^2 \tag{31}$$

where $A_{LB}(\theta) = \exp(-\alpha_0 z / (2\cos(\theta)))$ is the ground absorption from the Beer–Lambert law.

Note again that α_0 is the mean absorption coefficient of the grating and does in general not equal the absorption coefficient of the crystal before the grating is written. This is particularly important when a writing pattern does not penetrate the full depth of the crystal and the absorption behind the grating has to be added to the calculation of the result (see e.g., discussion in [5]). Application of the above results leads to the general equation for arbitrary mixed out-of-phase gratings.

$$\eta_1(z,\theta) = A_{\mathrm{LB}}(\theta) \left| \epsilon_1'(\lambda) + i e^{\mathrm{sgn}(\theta) i \Phi} \epsilon_1''(\lambda) \right|^2 \frac{\left| \sin\left(\frac{\sqrt{\left(2\beta(|\theta|)\cos(\theta)\epsilon_0'(\lambda)\right)^2 - \epsilon_1''(\lambda)^2 + 2i\cos(\Phi)\epsilon_1''(\lambda)\epsilon_1'(\lambda) + \epsilon_1'(\lambda)^2} k_0 z}{4\left(\epsilon_0'(\lambda)\right)^{1/2}\cos(\theta)} \right) \right|^2}{\left| \left(2\beta(|\theta|)\cos(\theta)\epsilon_0'(\lambda)\right)^2 - \epsilon_1''(\lambda)^2 + 2i\cos(\Phi)\epsilon_1''(\lambda)\epsilon_1'(\lambda) + \epsilon_1'(\lambda)^2 \right|} \tag{32}$$

As this equation depends on all three grating parameters, ϵ_1', ϵ_1'' and Φ, a comprehensive plot is not possible. We will discuss various aspects and limit cases in the following.

First, note that in this representation only the second factor depends on the sign of the grating phase, as it only appears as the argument of even functions in the fraction. The argument of the square root and the absolute value in the denominator, $(2\beta(|\theta|)\cos(\theta)\epsilon_0'(\lambda))^2 - \epsilon_1''(\lambda)^2 + 2i\cos(\Phi)\epsilon_1''(\lambda)\epsilon_1'(\lambda) + \epsilon_1'(\lambda)^2$, is real for any pure grating ($n_1 = 0$ or $\alpha_1 = 0$) or for gratings with $\Phi = \pm\pi/2$. In the latter case, it is also positive under the condition $\epsilon_1''(\lambda) \leq \epsilon_1'(\lambda)$. The only complex element in $S(z)$ then is a global factor $\exp(2i\epsilon_0'(\lambda)\beta(|\theta|)k_0 z)$, resembling a phase shift linear to the off-Bragg factor $\beta(|\theta|)$. In out-of-phase gratings, however, the term $2i\cos(\Phi)\epsilon_1''(\lambda)\epsilon_1'(\lambda)$ adds an imaginary component.

3.4 Pure Refractive Index and Absorption Gratings

Pure gratings are a special case of in-phase gratings. In the case of a pure refraction grating ($\alpha_1 = 0$), the diffraction efficiency reduces to

$$\eta_1(z,\theta) = A_{\mathrm{LB}}(\theta)\epsilon_1'(\lambda)^2 \frac{\sin\left(\frac{\sqrt{\epsilon_1'(\lambda)^2 + \left(2\beta(|\theta|)\cos(\theta)\epsilon_0'(\lambda)\right)^2} k_0 z}{4\left(\epsilon_0'(\lambda)\right)^{1/2}\cos(\theta)} \right)^2}{\left(2\beta(|\theta|)\cos(\theta)\epsilon_0'(\lambda)\right)^2 + \epsilon_1'(\lambda)^2} \tag{33}$$

and, in case of a pure absorption grating ($n_1 = 0$), to

$$\eta_1(z,\theta) = A_{\mathrm{LB}}(\theta)\epsilon_1''(\lambda)^2 \frac{\left|\sinh\left(\frac{\sqrt{\epsilon_1''(\lambda)^2 - \left(2\beta(|\theta|)\cos(\theta)\epsilon_0'(\lambda)\right)^2}k_0 z}{4\left(\epsilon_0'(\lambda)\right)^{1/2}\cos(\theta)}\right)\right|^2}{\left|\left(2\beta(|\theta|)\cos(\theta)\epsilon_0'(\lambda)\right)^2 - \epsilon_1''(\lambda)^2\right|} \tag{34}$$

The hyperbolic sine in Equation (34) is achieved by extracting i from the square root according to $|\sin(ix)| = |\sinh(x)|$, resulting in the well-known forms for pure gratings. Notice, however, that thinking in terms of a hyperbolic z dependency of Equation (34) does only make sense in the vicinity of the Bragg angle as the square root will be imaginary again for larger $\beta(|\theta|)$.

3.5 In-Bragg Cases

In the in-Bragg case, Equation (32) simplifies to

$$\begin{aligned}\eta_1(z,\theta_B) =& A_{\mathrm{LB}}(\theta_B)\frac{\epsilon_1''(\lambda)^2 + 2\mathrm{sgn}(\theta)\sin(\Phi)\,\epsilon_1''(\lambda)\epsilon_1'(\lambda) + \epsilon_1'(\lambda)^2}{\sqrt{\epsilon_1''(\lambda)^4 + 2\cos(2\Phi)\,\epsilon_1''(\lambda)^2\epsilon_1'(\lambda)^2 + \epsilon_1'(\lambda)^4}}\cdot \\ & \left|\sin\left(\frac{\sqrt{\epsilon_1'(\lambda)^2 + 2i\cos(\Phi)\epsilon_1''(\lambda)\epsilon_1'(\lambda) - \epsilon_1''(\lambda)^2}k_0 z}{4\left(\epsilon_0'(\lambda)\right)^{1/2}\cos(\theta)}\right)\right|^2\end{aligned} \tag{35}$$

In pure gratings the coefficient outside the modulo cancels down, resulting in the in-Bragg expressions

$$\begin{aligned}\eta_1(z,\theta_B) &= A_{\mathrm{LB}}(\theta)\sin\left(\frac{\epsilon_1'(\lambda)k_0 z}{4\left(\epsilon_0'(\lambda)\right)^{1/2}\cos(\theta)}\right)^2 \\ &= A_{\mathrm{LB}}(\theta)\sin\left(\frac{n_1(\lambda)k_0 z}{2\cos(\theta)}\right)^2\end{aligned} \tag{36}$$

and

$$\begin{aligned}\eta_1(z,\theta_B) &= A_{\mathrm{LB}}(\theta)\left|\sinh\left(\frac{\epsilon_1''(\lambda)k_0 z}{4\left(\epsilon_0'(\lambda)\right)^{1/2}\cos(\theta)}\right)\right|^2 \\ &= A_{\mathrm{LB}}(\theta)\left|\sinh\left(\frac{n_0(\lambda)\kappa_1(\lambda)k_0 z}{2\cos(\theta)}\right)\right|^2 \\ &= A_{\mathrm{LB}}(\theta)\left|\sinh\left(\frac{\alpha_1 z}{4\cos(\theta)}\right)\right|^2\end{aligned} \tag{37}$$

The last lines in both cases resemble the results in [17].

Note that we have neglected the real permittivity modulation induced by an absorption index modulation and the imaginary modulation induced by a refractive index

modulation discussed in Section 2, as these are considerably smaller than the main contribution in common setups. Then,

$$\epsilon_1'(\lambda) = 2n_0 n_1 \text{ and } \epsilon_1''(\lambda) = \frac{n_0 \alpha_1}{k_0} \tag{38}$$

respectively.

In agreement with Kogelnik's work, the maximal diffraction efficiency of a pure absorption grating is $1/27$ or about 3.7%. This value is achieved in the Bragg angle for $\alpha_0 = \alpha_1$ and $\alpha_0 z/(4\cos(\theta_B)) = \arccos(2/\sqrt{3}) \approx 0.55$. In a pure refractive grating with $\alpha_0 = 0$, the maximal diffraction efficiency is 100%, obviously.

3.6 Transmission Efficiency

The general expression for the 0-th order (transmission) efficiency $\eta_0 = |R(z)/R(0)|$, including off-Bragg, is slightly more extensive, consisting of a sum of two terms:

$$\eta_0 = A_{\mathrm{LB}}(\theta)\left| \cos\left(\frac{z k_0 \sqrt{(2\beta(|\theta|)\cos(\theta)\epsilon_0'(\lambda))^2 - \epsilon_1''(\lambda)^2 + 2i\cos(\Phi)\,\epsilon_1''(\lambda)\epsilon_1'(\lambda) + \epsilon_1'(\lambda)^2}}{4\left(\epsilon_0'(\lambda)\right)^{1/2}\cos(\theta)} \right) \right.$$
$$\left. - \frac{i(2\beta(|\theta|)\cos(\theta)\epsilon_0'(\lambda))\sin\left(\frac{z k_0 \sqrt{\left(2\beta(|\theta|)\cos(\theta)\epsilon_0'(\lambda)\right)^2 - \epsilon_1''(\lambda)^2 + 2i\cos(\Phi)\epsilon_1''(\lambda)\epsilon_1'(\lambda) + \epsilon_1'(\lambda)^2}}{4\left(\epsilon_0'(\lambda)\right)^{1/2}\cos(\theta)} \right)}{\sqrt{(2\beta(|\theta|)\cos(\theta)\epsilon_0'(\lambda))^2 - \epsilon_1''(\lambda)^2 + 2i\cos(\Phi)\,\epsilon_1''(\lambda)\epsilon_1'(\lambda) + \epsilon_1'(\lambda)^2}} \right|^2 \tag{39}$$

In the general in-Bragg case, this reduces to

$$\eta_0 = A_{\mathrm{LB}}(\theta)\left| \cos\left(\frac{z k_0 \sqrt{\epsilon_1'(\lambda)^2 + 2i\cos(\Phi)\,\epsilon_1''(\lambda)\epsilon_1'(\lambda) - \epsilon_1'(\lambda)^2}}{4\left(\epsilon_0'(\lambda)\right)^{1/2}\cos(\theta)} \right) \right|^2 \tag{40}$$

For a pure refractive grating with $\alpha_0 = 0$, $\eta_0 + \eta_1 = 1$ as expected.

4 Examples

Pure gratings have been extensively discussed in literature for the last 40+ years since the previously mentioned groundbreaking paper by Kogelnik. In the following, we will discuss two more complex cases, which have come into the focus of attention only in the last few years, due to the progress made in the fields of advanced materials and tunable lasers.

4.1 Spectroscopic in-Bragg Analysis of the Diffraction Efficiency

Usually, the diffraction efficiency is measured for a single wavelength of an angular range around the Bragg angle. The resulting curve is called rocking curve and examples

are shown and discussed in the next section. Here, we will examine the dependency of the diffraction efficiency of mixed gratings of the reference-beam wavelength over a broad optical spectrum range.

The description of the complex permittivity related to a recorded hologram considers both the ground state permittivity and the optically induced change of the permittivity. The ground state permittivity is decisive for the overall transmittance of the recording and reconstruction waves. Particularly, it determines the efficiency of hologram reconstruction which is its key measure.

With respect to dispersive measurements of the efficiency, the ground state permittivity thus needs to be taken into account. Otherwise, misinterpretation of the efficiency may occur, *i.e.*, losses of the efficiency as a function of the wavelength due to an increase of the mean imaginary part of the permittivity may be understood as a reduction of the amplitude of the permittivity change.

In the following, we will show our results on two exemplary systems, both modelled on lithium niobate. The base absorption coefficient and refractive index are modelled by using a simple resonator model. It results in a pronounced absorption band at the lower edge of the optical spectrum, *i.e.*, at high photon energies, with a band edge ($\alpha = 20\,\mathrm{cm}^{-1}$) at 300 nm for lithium niobate grown from the congruently melting composition. Exposure to light with photon energies in the vicinity of the band edge energy can be applied for the recording of holograms via the mechanism of interband photorefraction [35]. The tail of this absorption further determines the fundamental absorption in the visible and near-infrared spectrum, and is important for near-infrared recording mechanisms of holograms in lithium niobate [36].

We now add a Gaussian-shaped absorption spectrum around 500 nm resembling the absorption band of Fe^{2+} in Fe-doped lithium niobate and reveal the spectrum depicted in Figure 3 (a). Alternatively, we model a broad and asymmetric absorption spectrum of the form

$$\alpha(\lambda) \propto \lambda \exp\left(-\frac{(2E_p - \hbar c/\lambda)^2}{4E_p \hbar\omega_0}\right) \tag{41}$$

according to the theoretical description of optical features of small bound polarons. This type of absorption, shown in Figure 3 (b) exemplarily for the small bound Nb_{Li}^{4+} electron polaron centered at 1.6 eV, describes the light-induced small polaron transfer from a specific lattice site to one of its next-neighbouring site. (For the given example, from a Nb_{Li}^{4+} lattice site to one of the eight Nb_{Nb}^{5+} sites, to which the defect is octahedrally coordinated.) Thus, the absorption is characterized by a minimum energy E_p and a representative phonon energy of the system $\hbar\omega_0$ [37]. Here, c denotes the speed of light in vacuum and ω_0 is the phonon frequency.

Contrary to the dominating oscillator for the band-to-band transition, the strengths of the Fe^{2+} and small polaron absorption characteristics are strongly affected by light-exposure: The electron is excited from Fe^{2+} to the valence band, thus Fe^{3+} remains, featuring an extremely sharp absorption band [38]. The light-induced optical transfer of the electron from the Nb_{Li}^{4+} polaronic site to its neighbouring Nb_{Nb}^{5+} site results in the disappearance of the near-infrared band at 1.6 eV, while an absorption band of the small

free Nb_{Nb}^{4+} electron polaron builds up at approximately 1.0 eV.

Taking into account these optically induced alterations of the absorption bands and the fact that potentially both bands can diminish completely, we can model the causally related light-induced change of the refractive index via Kramers–Kronig relation. Figure 3 shows the dispersion of the optically induced index amplitude n_1 free of the dispersion of the index $n_0(\lambda)$. In comparison with the classical recording of phase holograms via the photorefractive effect [39], we note that the dispersion of the index amplitude features a change of the sign within the optical spectrum so that spectra with both positive and negative dispersion appear. This feature has been experimentally verified for small-polaron recording of holograms in lithium niobate in [40].

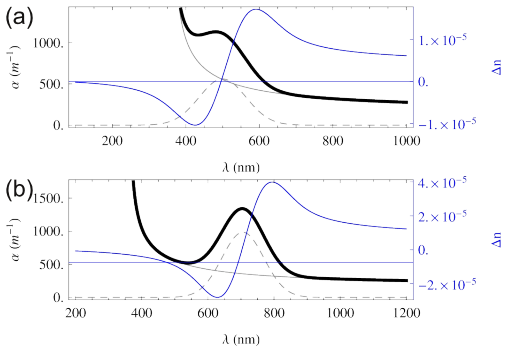

Figure 3: Full absorption coefficient (thick black), base absorption (grey black), modulated absorption band (dashed black) and refractive index change emerging from Kramers–Kronig relation (blue) for Gaussian absorption band related to Fe-doping (a) and polaronic absorption (b).

For in-Bragg measurements, the Bragg angle has to be adjusted for each wavelength. The Bragg angle transforms according to

$$\theta_B(\lambda) = \arcsin\left(\frac{\lambda\left(\epsilon_0'(\lambda_R)\right)^{1/2}}{\lambda_R\left(\epsilon_0'(\lambda)\right)^{1/2}}\sin(\theta_{B,R})\right) \tag{42}$$

where $\theta_{B,R}$ is a known Bragg angle for a reference wavelength λ_R.

Using the exemplary permittivities derived above, the curves shown in Figure 4 emerge.

Obviously, the induced refractive index change has a significant influence on the diffraction efficiency aside from the absorption maximum, while the contribution of both gratings is in the same order of magnitude in the ranges of their maximal amplitudes. The overall curve is a simple sum of the two pure gratings. Numerical analysis shows that the FWHM of the rocking curve is maintained over the complete spectrum under consideration. This is in strong agreement with the explanation for the lack of definition of the grating given in Section 3.1, as the effects involved are not wavelength dependent.

Notice that these effects are only necessarily true for phase-symmetrical gratings. We will examine non-phase-symmetric gratings in the following sections.

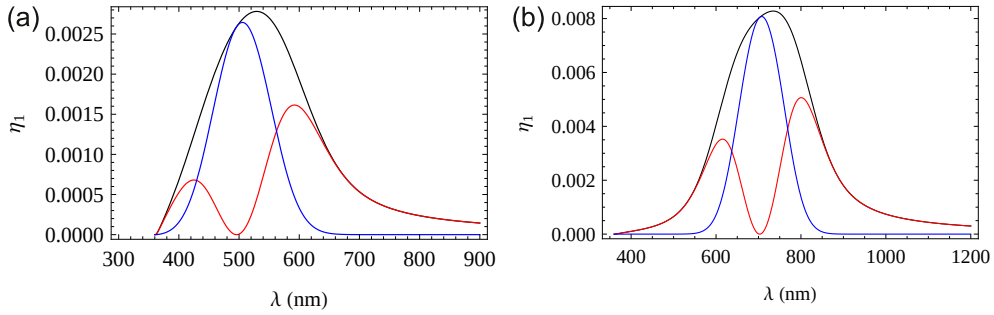

Figure 4: Diffraction efficiency for a Gaussian absorption band (a) and a polaronic absorption band (b). Each figure shows the overall diffraction efficiency (black) and the efficiency from the pure absorption (blue) and the pure refractive index grating (red).

4.2 Effects of Phase Shifts in Mixed Gratings

For a pure refractive or absorption grating, the analysis of the grating parameters is trivial. The modulation depth of the particular grating can be derived from the in-Bragg diffraction efficiency $\eta_1 = I_s(z)/I_0$ from Equations (36) and (37).

Only in the case that the effective grating thickness d_h is smaller than the sample thickness d—for example through holographic recording in strongly absorbing materials—the rocking curve is required to determine the actual grating parameters in the form of an effective grating thickness, as the in-Bragg results only allow to determine the $z\epsilon_1'(\lambda)$ product. However, they allow a decent estimation as a starting value for a fit using Equations (33) and (34).

For mixed and potentially out-of-phase gratings, for which experimental evidence has been provided in [41], the situation is more complicated [42, 43]. First theoretical results for a related Borrmann effect have been presented in [44] and a comprehensive discussion is given in [20] including a qualitative discussion of the Borrmann effect in the diffraction efficiency of the positive and negative range of the angle of incidence. Basically, out-of-phase gratings result in different first order diffraction efficiencies for positive and negative Bragg angles $\eta_1(\pm\theta)$ and a shift of the maximal zeroth order diffraction efficiency away from the Bragg angle. Examplary plots are given in Figure 5. We have chosen $\epsilon_1''(\lambda) = \epsilon_1'(\lambda)$, as this configuration gives the most pronounced effects.

While the effect itself has been described qualitatively in the literature cited above, a quantitative theoretical description has not been presented yet. We will analyse the ratio of first order diffraction efficiencies between the positive and negative angle range in the following section.

Note that against this background, a quantity like the "Japanese diffraction efficiency" $\eta_1/(\eta_0 + \eta_1)$ is meaningless as an intrinsic scalar attribute of the grating, as in such gratings, the value may strongly depend on the direction of incidence.

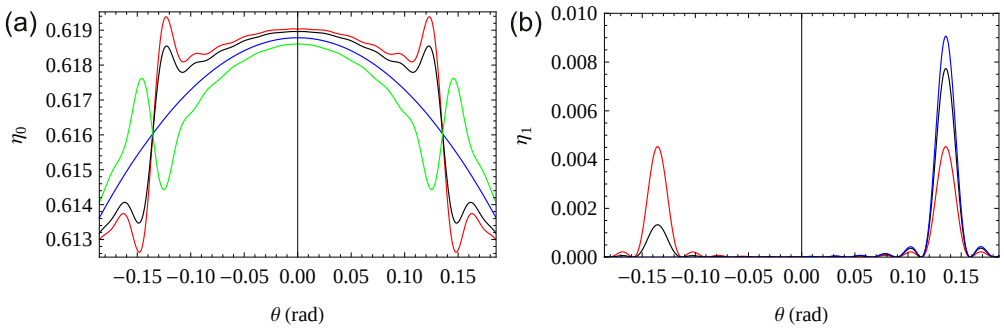

Figure 5: Zeroth (a) and first order (b) diffraction efficiency for $\epsilon_1''(\lambda) = \epsilon_1'(\lambda) = 1,13 \times 10^{-3}\,\mathrm{F{\cdot}m^{-1}}$. Figure (a): $\Phi = 0$ (red), $\Phi = \pi/4$ (black), $\Phi = \pi/2$ (blue), $\Phi = 3\pi/4$ (green). Figure (b): $\Phi = 0$ (red), $\Phi = \pi/4$ and $\Phi = 3\pi/4$ (black), $\Phi = \pi/2$ (blue).

5 Quantitative Analysis of the Borrmann Effect

Due to the simplification of the formal representation presented above, the quotient $\eta_1(\theta_B)/\eta_1(-\theta_B)$ can be calculated very easily from Equation (35). As only the denominator in Equation (35) depends on the direction of the incident beam, we simply get

$$\begin{aligned}
\frac{\eta_1(\theta)}{\eta_1(-\theta)} &= \frac{\epsilon_1''(\lambda)^2 + 2\sin(\Phi)\,\epsilon_1''(\lambda)\epsilon_1'(\lambda) + \epsilon_1'(\lambda)^2}{\epsilon_1''(\lambda)^2 - 2\sin(\Phi)\,\epsilon_1''(\lambda)\epsilon_1'(\lambda) + \epsilon_1'(\lambda)^2} \\
&= \frac{1 + Q_{\mathrm{BA}}^2 + 2Q_{\mathrm{BA}}\sin(\Phi)}{1 + Q_{\mathrm{BA}}^2 - 2Q_{\mathrm{BA}}\sin(\Phi)} \\
&= \left| \frac{\epsilon_1'(\lambda) + ie^{-i\Phi}\epsilon_1''(\lambda)}{\epsilon_1'(\lambda) + ie^{i\Phi}\epsilon_1''(\lambda)} \right|^2 \\
&= \left| \frac{Q_{\mathrm{BA}} + ie^{-i\Phi}}{Q_{\mathrm{BA}} + ie^{i\Phi}} \right|^2
\end{aligned} \tag{43}$$

where $Q_{\mathrm{BA}} = \epsilon_1'(\lambda)/\epsilon_1''(\lambda)$. The same can be achieved using the complete off-Bragg Equation (32) resulting in the last two lines of Equation (43). Thus, the ratio is constant over the full rocking curve.

Equation (43) fulfils the necessary symmetry condition $f(\Phi) = f(2\pi - \Phi)^{-1}$ and reaches its maximum at $\Phi = \pi/2$. This is expected as, in this case, the interference pattern of the reference and signal beam appears in its optimal position (*i.e.*, in the position that would emerge in pure gratings) relative to both gratings in either the positive or the negative angular range. The corresponding graph is shown in Figure 6. (b) shows a high signal-to-noise ratio for Q_{BA} in the range of at least 0 to 5. For larger ratios between real and imaginary part of the permittivity, accurate measurements may be difficult. The pole at $\Phi = \pi/2$ corresponds to the blue curve in Figure 5 (a), where the signal beam vanishes in the negative Bragg angle.

For a mixed grating ($\epsilon_1''(\lambda) \neq 0 \neq \epsilon_1'(\lambda)$), due to the symmetry of the sine, Equation (43) will always have a solution of the form $\Phi = \pi/2 \pm \Delta\Phi(Q_{BA})$ or $\Phi = -\pi/2 \pm \Delta\Phi(Q_{BA})$. This corresponds to the black curve in Figure 5 (a) representing $\Phi = \pi/4$ and $\Phi = 3\pi/4$. These two results may only be distinguished by regarding the zeroth order diffraction efficiency. It has been shown in [20] that $|\Phi| < \pi/2$ if and only if $\eta_0(\theta = 0) < A_{LB}(0)$.

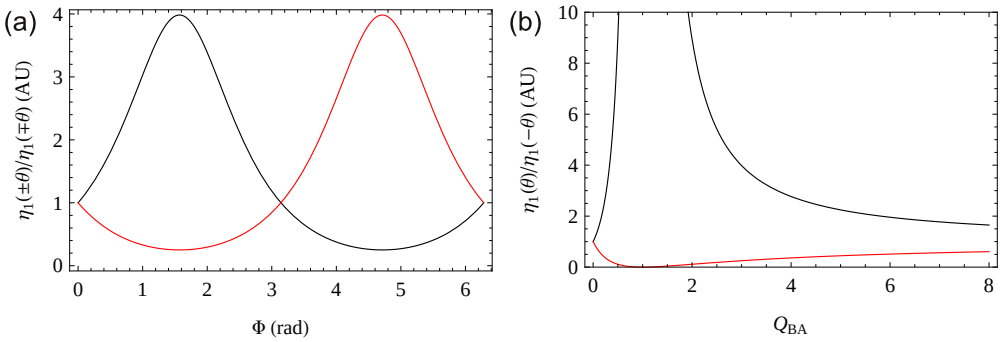

Figure 6: Proportions $\eta_1(\theta)/\eta_1(-\theta)$ (black) and $\eta_1(-\theta)/\eta_1(\theta)$ (red). In figure (a), the phase shift Φ-depending ratios are show for $Q_{BA} = 3$. In figure (b) the Q_{BA}-depending ratios are given for $\Phi = \pi/2$.

Equation (43) can be solved for Q_{BA}, resulting in

$$Q_{\mathrm{BA}} = \frac{\left(\frac{\eta_1(\theta)}{\eta_1(-\theta)} + 1\right)\sin(\Phi) \pm \sqrt{\left(\frac{\eta_1(\theta)}{\eta_1(-\theta)} + 1\right)^2 \sin(\Phi)^2 - \left(\frac{\eta_1(\theta)}{\eta_1(-\theta)} - 1\right)^2}}{\frac{\eta_1(\theta)}{\eta_1(-\theta)} - 1} \tag{44}$$

or for Φ, yielding

$$\begin{aligned} \Phi &= \pi - \arcsin\left(\frac{(1+Q_{\mathrm{BA}}^2) - \left(\frac{\eta_1(\theta)}{\eta_1(-\theta)} - 1\right)}{2Q_{\mathrm{BA}} - \left(\frac{\eta_1(\theta)}{\eta_1(-\theta)} + 1\right)}\right) + 2\pi N \quad \text{or} \\ \Phi &= \arcsin\left(\frac{(1+Q_{\mathrm{BA}}^2) - \left(\frac{\eta_1(\theta)}{\eta_1(-\theta)} - 1\right)}{2Q_{\mathrm{BA}} - \left(\frac{\eta_1(\theta)}{\eta_1(-\theta)} + 1\right)}\right) + 2\pi N \end{aligned} \tag{45}$$

where N is an integer. The two solutions for Φ may be distinguished as mentioned above. Obviously, only positive quotients Q_{BA} have physical nature, resulting in Figure 7. For $\eta_1(\theta)/\eta_1(-\theta) \to 1$, the loop tends towards a rectangular curve delimited be the axes and $\Phi = \pi$ and $Q_{\mathrm{BA}} = \infty$. This proves that a first order diffraction efficiency symmetric with respect to the read-out angle is only achievable with pure gratings or symmetric gratings (*i.e.*, $\Phi = 0$ of $\Phi = \pi$).

To determine all three independent grating parameters ϵ_1', ϵ_1'' and Φ, at least three independent data points are needed. In-Bragg, these could be $\eta_1(\pm\theta_B)$ and $\eta_0(\theta_B)$. Unfortunately, as shown in Figure 5 (where $\eta_0(\theta_B)$ is nearly the same for all Φ), $\eta_0(\theta_B)$ has a very low signal-to-noise ratio and thus does not qualify for the examination.

Consequently, either off-Bragg or a different setup, for example involving two incident beams, is necessary.

Finding an analytical expression for the shift of the extrema around the Bragg angle of Equation (21) is incomparably harder than the previous calculations. The equation has the structure

$$\eta_0 = \sin\left(k(\theta)z\right)^2 + (1 + \Delta(\theta))\cos\left(\left(k(\theta) + \Delta k(\theta)\right)z\right)^2 \tag{46}$$

where $\Delta(\theta), \Delta k(\theta) \ll 1$ and thus $\eta_0 \approx 1$ according to $\sin(x)^2 + \cos(x)^2 = 1$. Thus, it is not enough to examine only a part of the full term.

Currently, the most efficient way for the examination of the grating appears to be inserting Equation (45) into Equations (35) and (39) at $\theta = \theta_{\text{max}}$—reducing the parameter space to two dimensions—and solving for $\epsilon_1''(\lambda)$, $\epsilon_1'(\lambda)$ numerically.

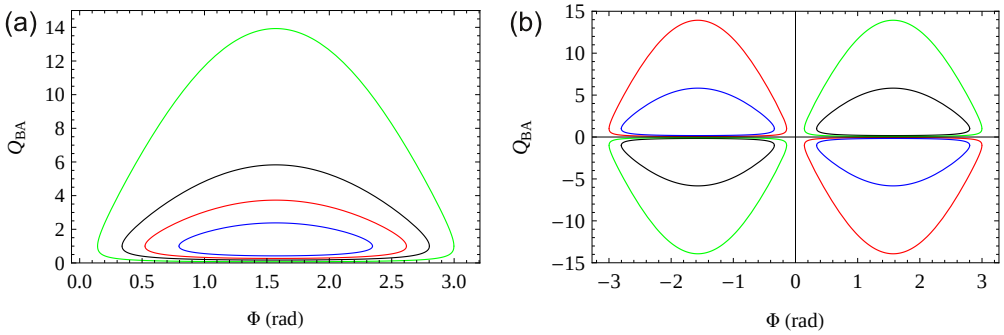

Figure 7: Graph of Equation (44). Figure (a) shows the relation between Q_{BA} and Φ, for $\eta_1(\theta)/\eta_1(-\theta) = 4/3$ (green), 2 (black), 3 (red), 6 (blue). Figure (b) shows the complete mathematical solution including $\eta_1(\theta)/\eta_1(-\theta) < 1$, for $\eta_1(\theta)/\eta_1(-\theta) = 4/3$ (green), 2 (black), $3/4$ (red), $1/2$ (blue).

6 Conclusions

Until recently, analyses in the field of holographic spectroscopy have not been necessary in
electro-optics, as the fundamental mechanisms show little dispersion characteristics. However, methods like the absorption-induced change of the refractive index and new photosensitive materials have brought wavelength-dependent holograms with pronounced photosensitivities over the entire optical spectrum range into the focus of attention.

Kogelnik's coupled-wave theory is still a valuable basis for the study of these topical problems. However, the original works make assumptions that do not comply with all modern experimental setups. Successive works closed some of these gaps at the cost of significantly increased algebraic complexity. The set of equations presented here

reduces this complexity to a level that allows advanced analysis of even those effects that occur only in complex gratings (Borrmann effect). As an example, the analytic tools supplied in this paper are applied not only to describe the dispersion behaviour of such gratings, but also to investigate dependencies on the direction of incidence on out-of-phase mixed gratings, that can be observed, e.g., in holographic polymer dispersed liquid crystals. Using our quantitative analysis, it is possible to determine the full set of grating parameters (real and imaginary part of the permittivity modulation, and phase shift between these modulations) of such systems.

Acknowledgements

We would like to thank Heinz-Jürgen Schmidt for the valuable suggestion regarding the mathematical backgrounds of the analysis, Romano Rupp for the helpful discussions and starting points at the beginning of the derivation, and Hauke Brüning for supplying experimental data used during the testing of the results. Financial support by the DFG (project No. IM37/5 and INST190/137-1) is gratefully acknowledged.

References

1. Gabor, D. A new microscopic principle. *Nature* **1948**, *161*, 777–778.
2. Imlau, M.; Fally, M.; Coufal, H.; Burr, G.; Sincerbox, G. Holography and Optical Storage. In *Springer Handbook of Lasers and Optics*; Träger, F., Ed.; Springer: New York, NY, USA, 2007; pp. 1205–1249.
3. Moser, C.; Havermeyer, F. Method and Apparatus for Large Spectral Coverage Measurement of Volume Holographic Gratings. U.S. Patent 8,049,885, 1 November 2011.
4. Moser, C.; Havermeyer, F. Measurement of Volume Holographic Gratings. U.S. Patent 8,139,212, 20 March 2012.
5. Imlau, M.; Brüning, H.; Schoke, B.; Hardt, R.; Conradi, D.; Merschjann, C. Hologram recording via spatial density modulation of $Nb_{Li}{}^{4+/5+}$ antisites in lithium niobate. *Opt. Express* **2011**, *19*, 15322–15338.
6. Dieckmann, V.; Eicke, S.; Springfeld, K.; Imlau, M. Transition metal compounds towards holography. *Materials* **2012**, *5*, 1155–1175.
7. Guibelalde, E. Coupled wave analysis for out-of-phase mixed thick hologram gratings. *Opt. Quantum Electron.* **1984**, *16*, 173–178.
8. Moharam, M.G.; Gaylord, T.K. Rigorous coupled-wave analysis of planar-grating diffraction. *J. Opt. Soc. Am.* **1981**, *71*, 811–818.

9. Uchida, N. Calculation of diffraction efficiency in hologram gratings attenuated along the direction perpendicular to the grating vector. *J. Opt. Soc. Am.* **1973**, *63*, 280–287.

10. Kukhtarev, N.V.; Markov, V.B.; Odulov, S.G.; Soskin, M.S.; Vinetskii, V.L. Holographic storage in electrooptic crystals. I. steady state. *Ferroelectrics* **1978**, *22*, 949–960.

11. Kukhtarev, N.V.; Markov, V.B.; Odulov, S.G.; Soskin, M.S.; Vinetskii, V.L. Holographic storage in electrooptic crystals. II. Beam coupling—Light amplification. *Ferroelectrics* **1978**, *22*, 961–964.

12. Russell, P. Optical volume holography. *Phys. Rep.* **1981**, *71*, 209–312.

13. Strait, J.; Reed, J.D.; Kukhtarev, N.V. Orientational dependence of photorefractive two-beam coupling in InP:Fe. *Opt. Lett.* **1990**, *15*, 209–211.

14. Sturman, B.I.; Webb, D.J.; Kowarschik, R.; Shamonina, E.; Ringhofer, K.H. Exact solution of the Bragg-diffraction problem in sillenites. *J. Opt. Soc. Am. B* **1994**, *11*, 1813–1819.

15. Sheridan, J.T. Generalization of the boundary diffraction method for volume gratings. *J. Opt. Soc. Am. A* **1994**, *11*, 649–656.

16. Michael, R.; Gleeson, J.G.; John, T.S. Optimisation of photopolymers for holographic applications using the non-local photo-polymerization driven diffusion model. *Opt. Express* **2011**, *19*, 22423–22436.

17. Kogelnik, H. Coupled wave theory for thick hologram gratings. *Bell Syst. Tech. J.* **1969**, *48*, 2909–2947.

18. Montemezzani, G.; Zgonik, M. Light diffraction at mixed phase and absorption gratings in anisotropic media for arbitrary geometries. *Phys. Rev. E* **1997**, *55*, 1035–1047.

19. Sturman, B.I.; Podivilov, E.V.; Ringhofer, K.H.; Shamonina, E.; Kamenov, V.P.; Nippolainen, E.; Prokofiev, V.V.; Kamshilin, A.A. Theory of photorefractive vectorial wave coupling in cubic crystals. *Phys. Rev. E* **1999**, *60*, 3332–3352.

20. Fally, M.; Ellabban, M.; Drevensek-Olenik, I. Out-of-phase mixed holographic gratings: A quantative analysis. *Opt. Express* **2008**, *16*, 6528–6536.

21. Haarer, D.; Spiess, H.W. *Spektroskopie Amorpher und Kristalliner Festkörper*; Springer DE: Heidelberg, Germany, 1995.

22. Shafer, D. Gaussian to Flat-Top intensity distributing lens. *Opt. Laser Technol.* **1982**, *14*, 159–160.

23. Au, L.B.; Solymar, L. Space-charge field in photorefractive materials at large modulation. *Opt. Lett.* **1988**, *13*, 660–662.

24. Ellen, O.; Frederick, V.; Lambertus, H. Higher-order analysis of the photorefractive effect for large modulation depths. *J. Opt. Soc. Am. A* **1986**, *3*, 181–187.

25. Träger, F. *Springer Handbook of Lasers and Optics*, 2nd ed.; Springer: Heidelberg, Germany, 2012.

26. Sheridan, J. A comparison of diffraction theories for off-bragg replay. *J. Mod. Opt.* **1992**, *39*, 1709–1718.

27. Solymar, L.; Cooke, D.J. *Volume Holography and Volume Gratings*; Academic Press Inc: Waltham, MA, USA, 1982.

28. Syms, R.R.A. *Practical Volume Holography*; Clarendon Press: Oxford, UK, 1990.

29. Hartwig, U.; Peithmann, K.; Sturman, B.; Buse, K. Strong permanent reversible diffraction gratings in copper-doped lithium niobate crystals caused by a zero-electric-field photorefractive effect. *Appl. Phys. B* **2004**, *80*, 227–230.

30. Gaylord, T.K.; Moharam, M.G. Planar dielectric grating diffraction theories. *Appl. Phys. B Lasers Opt.* **1982**, *28*, 1–14.

31. Moharam, M.G.; Gaylord, T.K. Rigorous coupled-wave analysis of grating diffraction—E-mode polarization and losses. *J. Opt. Soc. Am.* **1983**, *73*, 451–455.

32. Moharam, M.G.; Grann, E.B.; Pommet, D.A.; Gaylord, T.K. Formulation for stable and efficient implementation of the rigorous coupled-wave analysis of binary gratings. *J. Opt. Soc. Am. A* **1995**, *12*, 1068–1076.

33. Gallego, S.; Cristian, N.; Estepa, L.A.; Ortuño, M.; Márquez, A.; Francés, J.; Pascual, I.; Beléndez, A. Volume holograms in photopolymers: Comparison between analytical and rigorous theories. *Materials* **2012**, *5*, 1373–1388.

34. Fally, M.; Klepp, J.; Tomita, Y. An experimental study on the validity of diffraction theories for off-Bragg replay of volume holographic gratings. *Appl. Phys. B Lasers Opt.* **2012**, 1–8.

35. Dittrich, P.; Koziarska-Glinka, B.; Montemezzani, G.; Günter, P.; Takekawa, S.; Kitamura, K.; Furukawa, Y. Deep-ultraviolet interband photorefraction in lithium tantalate. *J. Opt. Soc. Am. B* **2004**, *21*, 632–639.

36. Krätzig, E.; Buse, K. Two-Step processes and IR recording in photorefractive crystals. *Top. Appl. Phys.* **2003**, *86*, 23–40.

37. Schirmer, O.F.; Imlau, M.; Merschjann, C.; Schoke, B. Electron small polarons and bipolarons in $LiNbO_3$. *J. Phys. Condens. Matt.* **2009**, *21*, 123201:1-123201:29

38. Schirmer, O.; Thiemann, O.; Wöhlecke, M. Defects in $LiNbO_3$—I. Experimental aspects. *J. Phys. Chem. Solids* **1991**, *52*, 185–200.

39. Günter, P.; Huignard, J.P. *Photorefractive Materials and Their Applications 1: Basic Effects*; Springer: Berlin, Germany, 2006.

40. Brüning, H.; Dieckmann, V.; Schoke, B.; Voit, K.; Imlau, M.; Corradi, G.; Merschjann, C. Small-polaron based holograms in $LiNbO_3$ in the visible spectrum. *Opt. Express* **2012**, *20*, 13326–13336.

41. Neipp, C.; Pascual, I.; Beléndez, A. Experimental evidence of mixed gratings with a phase difference between the phase and amplitude grating in volume holograms. *Opt. Express* **2002**, *10*, 1374–1383.

42. Kahmann, F. Separate and simultaneous investigation of absorption gratings and refractive-index gratings by beam-coupling analysis. *J. Opt. Soc. Am. A* **1993**, *10*, 1562–1569.

43. Fally, M. Separate and simultaneous investigation of absorption gratings and refractive-index gratings by beam-coupling analysis: Comment. *J. Opt. Soc. Am. A* **2006**, *23*, 2662–2663.

44. Carretero, L.; Madrigal, R.F.; Fimia, A.; Blaya, S.; Beléndez, A. Study of angular responses of mixed amplitude–phase holographic gratings: Shifted Borrmann effect. *Opt. Lett.* **2001**, *26*, 786–788.

B. Publications with proprietary licenses

All publication that are not contained in appendix A are published under proprietary licenses. In the archived printed copies, all publications are included with permission of the respective publishers. In the online version, they are omitted for license reasons. All publications are available for purchase at the publishers websites.

C. Contributions to conferences

During the development of this thesis, the following contributions have been presented on national and international conferences:

- Voit, K.-M., B. Hilling, H.-J. Schmidt, and M. Imlau. *"Theoretical discussion of present and novel optical methods for space-charge wave analysis"*
  DPG-Frühjahrstagung 2009, Dresden, Germany
- Voit, K.-M., B. Hilling, H.-J. Schmidt, and M. Imlau. *"Theoretical discussion of space-charge wave properties at low frequencies far from resonance"*
  Photorefractive Materials, Effects, and Devices 2009, Bad Honnef, Germany
- Voit, K.-M., B. Hilling, H.-J. Schmidt, and M. Imlau. *"Improvements of defect analysis by space-charge wave spectroscopy in semiconductors"*
  Europhysical Conference on Defects in Insulating Materials 2010, Pécs, Hungary
- Voit, K.-M., B. Hilling, H.-J. Schmidt, and M. Imlau. *"Improvements of defect analysis by space-charge wave spectroscopy in semiconductors"*
  APS March Meeting 2011, Dallas, USA
- Voit, K.-M., H. Brüning, and M. Imlau. *"Exact numerical and analytical studies of in-crystal phase shifts in off-Bragg two-beam coupling"*
  Photorefractive Materials, Effects, and Devices 2011, Ensenada, Mexico
- Voit, K.-M., H. Brüning, and M. Imlau. *"Quantitative examination of out-of-phase mixed holographic gratings"*
  APS March Meeting 2012, Boston, USA
- Voit, K.-M., H. Brüning, and M. Imlau. *"Quantitative examination of out-of-phase mixed holographic gratings"*
  DPG-Frühjahrstagung 2012, Berlin, Germany

Bibliography

[1] John Fauvel and Jeremy Gray. *The History of mathematics*. Macmillan Education in association with the Open University, 1987. ISBN: 9780333427910.

[2] Edward A. Bender. *An Introduction to Mathematical Modeling*. Courier Dover Publications, 2000. ISBN: 9780486411804.

[3] Herbert Stachowiak. *Modelle : Konstruktion der Wirklichkeit*. Kritische Information 101. München: Fink, 1983. ISBN: 3-7705-1962-0.

[4] Neil A. Gershenfeld. *The nature of mathematical modeling*. Reprinted with corr. Cambridge [u.a.]: Cambridge Univ. Press, 2000. ISBN: 0-521-57095-6.

[5] Edward N. Lorenz. *The Essence of Chaos*. University of Washington Press, 1995. ISBN: 9780295975146.

[6] Richard Levins. *Evolution in Changing Environments: Some Theoretical Explorations*. Princeton University Press, 1968. ISBN: 9780691080628.

[7] Georges Ifrah. *Universalgeschichte der Zahlen*. 6., Aufl. Zweitausendeins, 2008. ISBN: 3861507048.

[8] Karl-Heinz Schlote. *Chronologie der Naturwissenschaften: der Weg der Mathematik und der Naturwissenschaften von den Anfängen in das 21. Jahrhundert*. Harri Deutsch Verlag, 2002. ISBN: 9783817116102.

[9] Kay-Michael Voit. *Elemente vorantiker Mathematik [Elektronische Ressource]*. Wallenhorst: Kay-Michael Voit, 2007. URL: `http://nbn-resolving.de/urn:nbn:de:101:1-2013011615415`.

[10] Michel Serres. *Elemente eine Geschichte der Wissenschaft*. 2nd ed. Suhrkamp Verlag, 1998. ISBN: 3518289551.

[11] André Pichot. *Die Geburt der Wissenschaft : von den Babyloniern zu den frühen Griechen*. Sonderausg. Köln: Parkland-Verl., 2000. ISBN: 3-88059-978-5.

[12] Otto Neugebauer et al. *Mathematical cuneiform texts*. New Haven, Conn.: Pub. jointly by the American Oriental Society and the American Schools of Oriental Research, 1945.

[13] Eleanor Robson. *Mesopotamian Mathematics, 2100-1600 Bc: Technical Constants in Bureaucracy and Education*. Oxford University Press, 1999. ISBN: 9780198152460.

[14] Stephen F. Mason. *Geschichte der Naturwissenschaft in der Entwicklung ihrer Denkweisen*. Dt. Ausg. Kröners Taschenausgabe. Stuttgart: Kröner, 1974. ISBN: 3-520-30702-2.

[15] Wolfgang Balzer. *Empirische Theorien: Modelle - Strukturen - Beispiele : die Grundzüge der modernen Wissenschaftstheorie*. Vol. 20. Braunschweig: Vieweg, 1982. ISBN: 3-528-08513-4.

[16] Thomas S. Kuhn. *The Copernican revolution : planetary astronomy in the development of western thought*. Cambridge, Mass. [u.a.]: Harvard Univ. Pr., 1985. ISBN: 0-674-17103-9.

[17] Thomas S. Kuhn. *Die Entstehung des Neuen : Studien zur Struktur der Wissenschaftsgeschichte*. 1. Aufl., [Nachdr.] Suhrkamp-Taschenbuch Wissenschaft : Stw. Frankfurt am Main: Suhrkamp, 2002. ISBN: 3-518-27836-3.

[18] H. Kogelnik. "Coupled wave theory for thick hologram gratings". In: *The Bell System Technical Journal, Vol. 48, no. 9, November 1969, pp. 2909-2947* 48 (1969), pp. 2947, 2909.

[19] V. V. Bryksin and M. P. Petrov. "Electric currents generated by space-charge waves in high-resistivity semiconductors". In: *Physics of the Solid State* 48.7 (2006), pp. 1234–1243. ISSN: 1063-7834, 1090-6460. DOI: 10.1134/S1063783406070043.

[20] Henry C. Kessler. "The kinetics of light absorption in photobleaching media". In: *The Journal of Physical Chemistry* 71.8 (1967), pp. 2736–2737. ISSN: 0022-3654. DOI: 10.1021/j100867a058.

[21] Eugene L. Simmons. "Photochemistry of solid layers. Reaction rates". In: *The Journal of Physical Chemistry* 75.4 (1971), pp. 588–590. ISSN: 0022-3654. DOI: 10.1021/j100674a026.

[22] Volker Dieckmann. *Lichtinduzierte Isomerisierung in Sulfoxid- und Nitrosyl-Komplexen: Photosensitivität und Modifikation*. Logos Berlin, 2010. ISBN: 3832525211.

[23] D. Gabor. "A New Microscopic Principle". In: *Nature* 161.4098 (1948), pp. 777–778. ISSN: 0028-0836. DOI: 10.1038/161777a0.

[24] Kazuhiko Ohnuma and Fujio Iwata. "Color rainbow hologram and color reproduction". In: *Applied Optics* 27.18 (1988), pp. 3859–3863. DOI: 10.1364/AO.27.003859.

[25] E. N. Leith and J. Upatnieks. "Reconstructed Wavefronts and Communication Theory". In: *Journal of the Optical Society of America* 52.10 (1962), pp. 1123–1128. DOI: 10.1364/JOSA.52.001123.

[26] Yu N. Denisyuk. "On the Reproduction of the Optical Properties of an Object by the Wave Field of Its Scattered Radiation." In: *Optics and Spectroscopy* 15.279 (1963). ISSN: 0030-400X.

[27] Yu N. Denisyuk. "On the Reproduction of the Optical Properties of an Object by the Wave Field of Its Scattered Radiation. II". In: *Optics and Spectroscopy* 18 (1965), p. 152. ISSN: 0030-400X.

[28] Yu. N. Denisyuk. "My Way in Holography". In: *Leonardo* 25.5 (1992). ArticleType: research-article / Issue Title: Archives of Holography: A Partial View of a Three-Dimensional World: Special Issue / Full publication date: 1992 / Copyright © 1992 Leonardo, pp. 425–430. ISSN: 0024-094X. DOI: 10.2307/1575749.

[29] T. H. Maiman. "Stimulated Optical Radiation in Ruby". In: *Nature* 187 (1960), pp. 493–494. DOI: 10.1038/187493a0.

[30] M. Quintanilla and A. M. de Frutos. "Holographic filter that transforms a Gaussian into a uniform beam". In: *Applied Optics* 20.5 (1981), p. 879. ISSN: 0003-6935, 1539-4522. DOI: 10.1364/AO.20.000879.

[31] Jose R. Margarinos and Daniel J. Coleman. "Holographic Mirrors". In: *Optical Engineering* 24.5 (1985), pp. 245769–245769. ISSN: 0091-3286. DOI: 10.1117/12.7973573.

[32] Jose R. Magarinos and John F. Cueva. *Multi-layer holographic notch filter*. U.S. Classification: 359/8; 351/44; 359/15; 359/19; 359/24 International Classification: G02B 532. 1992.

[33] George A. Rakuljic and Victor Leyva. "Volume holographic narrow-band optical filter". In: *Optics Letters* 18.6 (1993), pp. 459–461. DOI: 10.1364/OL.18.000459.

[34] C. Joubert et al. "Phase volume holographic optical components for high-brightness single-LCD projectors". In: *Applied Optics* 36.20 (1997), pp. 4761–4771. DOI: 10.1364/AO.36.004761.

[35] R. a. M. Hikmet and H. Kemperman. "Electrically switchable mirrors and optical components made from liquid-crystal gels". In: *Nature* 392.6675 (1998), pp. 476–479. ISSN: 0028-0836. DOI: 10.1038/33110.

[36] Peter Günter and Jean Pierre Huignard. *Photorefractive Materials and Their Applications III: Applications*. 2007th ed. Springer, 2007. ISBN: 0387344438.

[37] Th. Woike et al. "New information storage elements on the basis of metastable electronic states". In: *Optics Communications* 106.1–3 (1994), pp. 6–10. ISSN: 0030-4018. DOI: 10.1016/0030-4018(94)90048-5.

[38] Savaş Tay et al. "An updatable holographic three-dimensional display". In: *Nature* 451.7179 (2008), pp. 694–698. ISSN: 0028-0836. DOI: 10.1038/nature06596.

[39] L. Solymar and D. J. Cooke. *Volume holography and volume gratings*. London [u.a.]: Acad. Press, 1981. ISBN: 0-12-654580-4.

[40] P. Hariharan. *Optical holography : principles, techniques and applications*. Cambridge [u.a.]: Cambridge Univ. Pr., 1984. ISBN: 0-521-24348-3.

[41] L. B. Lesem, P. M. Hirsch, and J. A. Jordan,Jr. "Scientific Applications: Computer synthesis of Holograms for 3-D display". In: *Commun. ACM* 11.10 (1968), 661–674. ISSN: 0001-0782. DOI: 10.1145/364096.364111.

[42] Wai Hon Lee. "Sampled Fourier Transform Hologram Generated by Computer". In: *Applied Optics* 9.3 (1970), pp. 639–643. DOI: 10.1364/AO.9.000639.

[43] Detlef Leseberg and Olof Bryngdahl. "Computer-generated rainbow holograms". In: *Applied Optics* 23.14 (1984), pp. 2441–2447. DOI: 10.1364/AO.23.002441.

[44] Detlef Leseberg and Christian Frère. "Computer-generated holograms of 3-D objects composed of tilted planar segments". In: *Applied Optics* 27.14 (1988), pp. 3020–3024. DOI: 10.1364/AO.27.003020.

[45] Nandor Bokor and Zsolt Papp. "Computational method for testing computer-generated holograms". In: *Optical Engineering* 35.10 (1996), pp. 2810–2815. ISSN: 0091-3286. DOI: 10.1117/1.600965.

[46] Fahri Yaraş, Hoonjong Kang, and Levent Onural. "Real-time phase-only color holographic video display system using LED illumination". In: *Applied Optics* 48.34 (2009), H48–H53. DOI: 10.1364/AO.48.000H48.

[47] M. Imlau et al. "Hologram recording via spatial density modulation of NbLi4+/5+ antisites in lithium niobate". In: *Optics Express* 19.16 (2011), pp. 15322–15338. DOI: 10.1364/OE.19.015322.

[48] Kay-Michael Voit and Mirco Imlau. "Holographic Spectroscopy: Wavelength-Dependent Analysis of Photosensitive Materials by Means of Holographic Techniques". In: *MDPI Materials* 6.1 (2013), pp. 334–358. DOI: 10.3390/ma6010334.

[49] Martin Fally, Mostafa Ellabban, and Irena Drevensek-Olenik. "Out-of-phase mixed holographic gratings : a quantative analysis". In: *Optics Express* 16.9 (2008), pp. 6528–6536. DOI: 10.1364/OE.16.006528.

[50] K. Sutter and P. Günter. "Photorefractive gratings in the organic crystal 2-cyclooctylamino-5-nitropyridine doped with 7,7,8,8-tetracyanoquinodimethane". In: *Journal of the Optical Society of America B* 7.12 (1990), pp. 2274–2278. DOI: 10.1364/JOSAB.7.002274.

[51] M. Imlau. "Defects and photorefraction: A relation with mutual benefit". In: *physica status solidi (a)* 204.3 (2007), 642–652. ISSN: 1862-6319. DOI: 10.1002/pssa.200673784.

[52] Michaela Lemmer. *Space-charge wave spectroscopy of wide bandgap semiconductors*. Osnabrück: Lemmer, Michaela, 2008.

[53] J.P. Huignard and A. Marrakchi. "Coherent signal beam amplification in two-wave mixing experiments with photorefractive Bi12SiO20 crystals". In: *Optics Communications* 38.4 (1981), pp. 249–254. ISSN: 0030-4018. DOI: 10.1016/0030-4018(81)90392-8.

[54] S.I. Stepanov, V.V. Kulikov, and M.P. Petrov. ""Running" holograms in photorefractive Bi12SiO20 crystals". In: *Optics Communications* 44.1 (1982), pp. 19–23. ISSN: 0030-4018. DOI: 10.1016/0030-4018(82)90006-2.

[55] S.I. Stepanov and M.P. Petrov. "Efficient unstationary holographic recording in photorefractive crystals under an external alternating electric field". In: *Optics Communications* 53.5 (1985), pp. 292–295. ISSN: 0030-4018. DOI: 10.1016/0030-4018(85)90265-2.

[56] M. P. Petrov et al. "Non-steady-state photo electromotive-force induced by dynamic gratings in partially compensated photoconductors". In: *Journal of Applied Physics* 68.5 (1990), pp. 2216 –2225. ISSN: 0021-8979. DOI: 10.1063/1.346525.

[57] B. I. Sturman et al. "Space-charge waves in photorefractive crystals and their-parametric excitation". In: *Journal of the Optical Society of America B* 10.10 (1993), pp. 1919–1932. DOI: 10.1364/JOSAB.10.001919.

[58] M. P. Petrov et al. "Grating oscillations in photorefractive crystals". In: *Optics Letters* 22.14 (1997), pp. 1083–1085. DOI: 10.1364/OL.22.001083.

[59] Henrik C. Pedersen, D. J. Webb, and Per M. Johansen. "Fundamental characteristics of space-charge waves in photorefractive sillenite crystals". In: *Journal of the Optical Society of America B* 15.10 (1998), pp. 2573–2580. DOI: 10.1364/JOSAB.15.002573.

[60] B. Hilling et al. "Space-charge wave excitation by superposition of static and moving interference patterns". In: *Physical Review B* 80.20 (2009), p. 205118. DOI: 10.1103/PhysRevB.80.205118.

[61] M. P. Petrov et al. "Trap recharging wave mode with a linear dispersion law for space-charge waves in CdTe:Ge". In: *Physical Review B* 74.8 (2006), p. 085202. DOI: 10.1103/PhysRevB.74.085202.

[62] Laszlo Solymar and Donald Walsh. *Electrical properties of materials*. 7. ed. Oxford [u.a.]: Oxford Univ. Press, 2004. ISBN: 0-19-926793-6.

[63] Rolf E. Hummel. *Electronic properties of materials*. 4. ed. New York, NY [u.a.]: Springer, 2011. ISBN: 978-1-441-98163-9.

[64] R. F. Kazarinov, R. A. Suris, and B. I. Fuks. "Thermal-current instability in compensated semiconductors". In: *Sov. Phy. Semicond.* 6.500 (1972).

[65] Peter Günter et al. *Photorefractive Materials and Their Applications I: Fundamental Phenomena*. 1st ed. Springer, 1988. ISBN: 3540183329.

[66] K. Buse. "Light-induced charge transport processes in photorefractive crystals I: Models and experimental methods". In: *Applied Physics B* 64.3 (1997), pp. 273–291. ISSN: 0946-2171, 1432-0649. DOI: 10.1007/s003400050175.

[67] K. Buse. "Light-induced charge transport processes in photorefractive crystals II: Materials". In: *Applied Physics B* 64.4 (1997), pp. 391–407. ISSN: 0946-2171, 1432-0649. DOI: 10.1007/s003400050190.

[68] N. V. Kukhtarev et al. "Holographic storage in electrooptic crystals. I. Steady state". In: *Ferroelectrics* 22.1 (1978), pp. 949–960. ISSN: 0015-0193. DOI: 10.1080/00150197908239450.

[69] N. V. Kukhtarev et al. "holographic storage in electrooptic crystals. II. Beam coupling-light amplification". In: *Ferroelectrics* 22.1 (1978), pp. 961–964. ISSN: 0015-0193. DOI: 10.1080/00150197908239451.

[70] M. P. Petrov et al. "Spatial Rectification of the Electric Field of Space Charge Waves". In: *Physical Review Letters* 84.22 (2000), pp. 5114–5117. DOI: 10.1103/PhysRevLett.84.5114.

[71] V. V. Bryksin and M. P. Petrov. "Spatial rectification of fields of photorefractive waves". In: *Physics of the Solid State* 42.10 (2000), pp. 1854–1860. ISSN: 1063-7834, 1090-6460. DOI: 10.1134/1.1318876.

[72] M. P. Petrov et al. "Overall rectification and second harmonic generation of space charge waves". In: *Physical Review B* 66.8 (2002), p. 085107. DOI: 10.1103/PhysRevB.66.085107.

[73] V. V. Bryksin and M. P. Petrov. "Second harmonic generation and rectification of space-charge waves in photorefractive crystals". In: *Physics of the Solid State* 44.10 (2002), pp. 1869–1879. ISSN: 1063-7834, 1090-6460. DOI: 10.1134/1.1514775.

[74] Jeffrey J. Rack. *Photoinduced molecular switches*. US patent nr. 6433270. 2002.

[75] Vincenzo Balzani, Alberto Credi, and Margherita Venturi. "Light powered molecular machines". In: *Chemical Society Reviews* 38.6 (2009), pp. 1542–1550. ISSN: 1460-4744. DOI: 10.1039/B806328C.

[76] K.C. Kao and G.A. Hockham. "Dielectric-fibre surface waveguides for optical frequencies". In: *Proceedings of the Institution of Electrical Engineers* 113.7 (1966), pp. 1151 –1158. ISSN: 0020-3270. DOI: 10.1049/piee.1966.0189.

[77] Pieter Kramer. *Reflective optical record carrier*. US patent nr. 5068846. 1991.

[78] Vincent W. S. Chan et al. *All-optical network architecture*. 1994.

[79] Françisco M. Raymo and Massimiliano Tomasulo. "Optical Processing with Photochromic Switches". In: *Chemistry – A European Journal* 12.12 (2006), 3186–3193. ISSN: 1521-3765. DOI: 10.1002/chem.200501178.

[80] Dorr Eugene Felt and University of California Libraries. *Mechanical arithmetic, or The history of the counting machine*. Chicago: Washington Institute, 1916.

[81] Doron Swade and Charles Babbage. *Difference Engine: Charles Babbage and the Quest to Build the First Computer*. Viking Penguin, 2001. ISBN: 064153440X.

[82] Konrad Zuse. *Der Computer - mein Lebenswerk / Konrad Zuse. Mit Geleitw. von F. L. Bauer und H. Zemanek*. 5., unveränd. Aufl. Berlin: Springer, 2010. ISBN: 978-3-642-12095-4.

[83] Julio S. Edgar Lilienfeld. *Method and Apparatus for Controlling Electric Currents*. US patent nr. 1745175. 1930.

[84] J. Bardeen and W. H. Brattain. "The Transistor, A Semi-Conductor Triode". In: *Physical Review* 74.2 (1948), pp. 230–231. DOI: 10.1103/PhysRev.74.230.

[85] J. S. Kilby. "Invention of the integrated circuit". In: *IEEE Transactions on electron devices* 23 (1976), pp. 648–654.

Acknowledgement

An erster Stelle geht mein besonderer Dank an meine beiden Betreuer, Herrn Prof. Dr. Mirco Imlau und Herrn apl. Prof. Dr. Heinz-Jürgen Schmidt. Beide haben mich nicht nur mit dem Thema dieser Dissertation zusammengebracht, sondern standen mir auch während ihrer Entstehung stets mit fruchtbaren Diskussionen und wertvollem Rat zur Seite. Mein Dank gilt außerdem Prof. Dr. Romano Rupp, der mich während meines Gastaufenthalts an der Nankai Universität in Tianjin nicht nur mit China, sondern auch mit der Theorie der Strahlkopplung vertraut gemacht hat.

Ich danke allen aktuellen und ehemaligen Mitgliedern der Arbeitsgruppe "Nichtlineare Molekül- und Festkörperoptik" für die freundliche Aufnahme, das positive Klima und die Unterstützungsbereitschaft in experimentellen Fragen. Besonderer Dank gilt dabei natürlich Dr. Burkhard Hilling, Dr. Hauke Brüning und Dr. Sebastian Eicke, die mit ihrer experimentellen Leistungen mein theoretisches Arbeitsfeld eröffnet haben. Vor dem gleichen Hintergrund danke ich Dr. Dmitri Petrov vom Ioffe Institut St. Petersburg.

Für finanzielle Unterstützung danke ich der Deutschen Forschungsgemeinschaft, die mich im Rahmen eines Forschungsstipendiums im Graduiertenkolleg 695 bis zu meiner Anstellung als wissenschaftlicher Mitarbeiter gefördert hat.

Nicht zuletzt danke ich meiner Familie, die immer für mich da war und mir – nicht nur in stressreichen Zeiten – vieles abgenommen hat. Ganz besonders hervorheben möchte ich dabei neben meinen Eltern meine Lebensgefährtin Michaela. Ich habe das Glück, dass sie mich nicht nur mit ständiger Geduld und einem stets offenen Ohr, sondern vor wie nach ihrem Ausscheiden aus der Arbeitsgruppe auch mit kompetentem fachlichen Rat unterstützen konnte.

Eidesstattliche Erklärung

Ich erkläre hiermit, die vorliegende Arbeit selbstständig und ohne unerlaubte Hilfe verfasst und keine anderen als die angegebenen Hilfsmittel und Quellen verwendet zu haben.

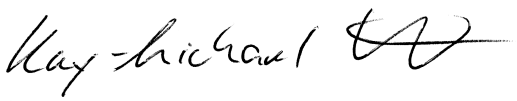

Osnabrück, im Februar 2013.